UC Irvine
UC Irvine Electronic Theses and Dissertations

Title
Thermally Induced Evolutions of Metallic Nanoparticles Through In Situ Transmission Electron Microscopy

Permalink
https://escholarship.org/uc/item/1m41248f

Author
Lu, Xiner

Publication Date
2024

Peer reviewed|Thesis/dissertation

eScholarship.org Powered by the California Digital Library
University of California

UNIVERSITY OF CALIFORNIA,
IRVINE

Thermally Induced Evolutions of Metallic Nanoparticles Through In Situ Transmission Electron Microscopy

DISSERTATION

submitted in partial satisfaction of the requirements
for the degree of

DOCTOR OF PHILOSOPHY

in Materials Science and Engineering

by

Xiner (Lucy) Lu

Dissertation Committee:
Associate Professor Kai He, Chair
Distinguished Professor Julie Schoenung
Assistant Professor William Bowman

2024

Portion of Chapter 2 © 2022 Elsevier
Portion of Chapter 3 © 2022 Elsevier
Portion of Chapter 3 © 2023 Oxford University Press
Chapter 4 © 2024 American Chemical Society
All other materials © 2024 Xiner (Lucy) Lu

TABLE OF CONTENTS

Page

LIST OF FIGURES iv
LIST OF TABLES vii
LIST OF ABBREVIATIONS viii
ACKNOWLEDGEMENTS x
VITA xii
ABSTRACT OF THE DISSERTATION xiv
CHAPTER 1 Introduction 1
1.1 Metallic Nanoparticles 1
1.1.1 Controlled Shape 1
1.1.2 Controlled Structure 5
1.1.3 Controlled Composition 7
1.2 Application of Metallic Nanoparticles 13
1.3 Fundamental Concepts 16
1.3.1 Metal Diffusion 16
1.3.2 Surface Energy 19
1.3.3 Phase Stability 22
1.4 Motivation 25
CHAPTER 2 Experimental Methods 29
2.1 Synthesis Methods 29
2.2 Characterization Methods 32
2.2.1 Conventional Transmission Electron Microscopy 32
2.2.2 Scanning Transmission Electron Microscopy 34
2.2.3 In Situ Transmission Electron Microscopy 36
CHAPTER 3 Machine Learning for Images Analysis 45
3.1 Background 45
3.1.1 AI-enabled Microscopy Data Analytics and Applications for In Situ TEM 45
3.1.2 Machine Learning for TEM Image Processing 46
3.2 Methods 50
3.2.1 Image Segmentation 50
3.2.2 Synthetic Data Generation 55
3.3 Results and Discussion 57
3.3.1 In Situ Images Analysis 57
3.3.2 Data Analysis Precision and Statistics 63

3.4 Conclusions 66
CHAPTER 4 Structural and Chemical Evolutions of Bimetallic Pt-Ni NPs at Elevated Temperatures 68
4.1 Background 68
4.2 Experimental Methods 70
4.2.1 Synthesis of Pt-Ni NPs 71
4.2.2 Materials Characterizations by TEM and XRD 72
4.3 Results and Discussion 73
4.3.1 Characterization of As-synthesized NPs 73
4.3.2 Thermally Induced Morphological Evolution of Single NP 77
4.3.3 Thermally Induced Chemical Evolutions of NPs Clusters 83
4.3.4 ML-assisted Images Analysis 86
4.4 Conclusions 89
CHAPTER 5 Structural and Chemical Evolutions of Quinary PdCuPtNiCo NPs at Elevated Temperatures 91
5.1 Background 91
5.2 Experimental Methods 93
5.2.1 Synthesis of PdCuPtNiCo NPs 93
5.2.2 Materials Characterizations by TEM 94
5.3 Results and Discussion 95
5.3.1 Characterization of As-synthesized NPs 95
5.3.2 Thermally Induced Chemical Evolutions of HEA NPs 97
5.3.3 Thermally Induced Chemical Evolutions of Single Core-shell NPs 100
5.3.4 Thermally Induced Chemical Evolutions of Neighbor Core-shell NPs 105
5.3.5 ML-assisted Images Analysis 107
5.3.6 Proposed Mechanism 110
5.4 Conclusions 114
CHAPTER 6 Conclusions and Perspectives 115
6.1 Conclusions 115
6.2 Perspectives 117
References 118

LIST OF FIGURES

Page

Figure 1.1 An illustration of general synthetic strategies for size and shape control of metal NPs 3

Figure 1.2 TEM and HRTEM images of shape-controlled NPs 4

Figure 1.3 3D renderings of different NP structures 6

Figure 1.4 Summary of synthesis methods of HEMs divided into solid phase and liquid phase synthesis. 11

Figure 1.5 Isothermal section of the Fe–Ni–Pt system at 600 °C with three constituent binary phase diagrams 24

Figure 2.1 Illustration of the NP conversion process to synthesize HEA NPs 32

Figure 2.2 Schematic of a TEM. 33

Figure 2.3 TEM images of Au seeds using different modes. 34

Figure 2.4 Schematic of the detectors in STEM. 35

Figure 2.5 Schematic illustration of in situ TEM methodologies and AI-enabled data analytics for energy conversion and storage materials 38

Figure 2.6 In situ heating setup and applications for nanocrystal evolutions at elevated temperatures. 41

Figure 3.1 ML approaches for identification and tracking morphologies and microstructures in TEM images. 48

Figure 3.2 Modified workflow making use of the autoencoder. 53

Figure 3.3 Processing steps of the input images. 54

Figure 3.4 Symmetric truncated octahedral using {111} facets with a specified distance of 0.8. 57

Figure 3.5 (a) Original in situ heating HAADF-STEM images of Pt-Ni NPs, and (b) contoured images using ML segmentation. 59

Figure 3.6 (a) Labeled center of mass location in the example contoured image. (b) x and y coordinates of the center of mass. 61

Figure 3.7 (a) Original HAADF-STEM image. (b) Cropped image from (a). (c) Plot of the center of mass distances as a function of temperature. 62

Figure 3.8 Image segmentation of HAADF-STEM images. 64

Figure 3.9 Quantitative analysis of image segmentation accuracy of traditional global thresholding method and ML-enhanced method for HAADF-STEM images taken at various magnifications 65

Figure 4.1 Schematic diagram of the synthesis and characterization of Pt–Ni NPs and their structural and chemical evolutions revealed by in situ heating TEM 71

Figure 4.2 STEM images of as-synthesized Pt-Ni NPs..... 74

Figure 4.3 Structural and compositional characterizations of as-synthesized Pt-Ni NPs. 75

Figure 4.4 XRD pattern of as-synthesized Pt-Ni NPs..... 76

Figure 4.5 STEM-EDS analysis of as-synthesized Pt-Ni NPs..... 77

Figure 4.6 Morphological evolution and surface facet development observed by in situ heating TEM. 79

Figure 4.7 HRTEM images showing the evolution of Pt-Ni NPs under in situ heating from 20 to 800 °C. 80

Figure 4.8 Tomographic visualization of the NP after heating..... 82

Figure 4.9 HAADF-STEM tomography tilt series images of a NP after in situ heating..... 83

Figure 4.10 Compositional evolution of solid-solution Pt-Ni NPs. 84

Figure 4.11 Compositional evolution of core-shell Pt-Ni NPs. 85

Figure 4.12 Compositional evolution of core-shell Pt-Ni NPs in the temperature range of 300-500 °C..... 86

Figure 4.13 (a) In situ heating of Pt-Ni NPs, (b) the ML segmentation and (c) contoured HAADF-STEM images. 87

Figure 4.14 Measured number of NPs and projected area indicating different stages of NPs evolution at elevated temperatures..... 89

Figure 5.1 Atomic structure and compositional characterizations of as-synthesized NPs... 96

Figure 5.2 Compositional evolution of HEA PdCuPtNiCo NPs..... 98

Figure 5.3 HAADF-STEM images showing the evolution of HEA PdCuPtNiCo NPs on carbon under in situ heating from 20 to 1000 °C. 99

Figure 5.4 Compositional evolution of core-shell PdCu@PtNiCo NPs with nearly no mass transfer..... 101

Figure 5.5 Compositional evolution of core-shell PdCu@PtNiCo NPs with mass transfer. 103

Figure 5.6 Characterization of background low-contrast small clusters. 104

Figure 5.7 HAADF-STEM images and corresponding EDS maps of 3 core-shell PdCu@PtNiCo NPs after heating with phase segregation..... 104

Figure 5.8 Compositional evolution of core-shell PdCu@PtNiCo NPs with coalesce. 106

Figure 5.9 HAADF-STEM images and corresponding EDS maps of 4 coalesced core-shell PdCu@PtNiCo NPs after heating. 107

Figure 5.10 (a) In situ heating HAADF-STEM images of core-shell PdCu@PtNiCo NPs, and (b) contoured images using ML segmentation. 108

Figure 5.11 Measured projected area of each NP and summation of two NPs. 110

Figure 5.12 Proposed mechanism from in situ TEM heating experiments. 111

LIST OF TABLES

Page

Table 1.1 Top down methods and bottom up methods of NP preparation 8
Table 1.2 Comparison of homogeneous catalysts and heterogeneous catalysts. 15
Table 1.3 Diffusion parameters for the solute diffusion of Ni-X systems..... 18
Table 1.4 Surface energy values and lattice constants of selected metal elements. 21
Table 2.1 Reduction potentials of the metal ions. 30
Table 3.1 Measurement of number and projected area of NPs from in situ STEM images... 60
Table 4.1 Measurement of number and projected area of NPs from in situ STEM images... 88
Table 5.1 Atomic percentage obtained from ICP-MS measurement for core-shell and HEA NPs. 97
Table 5.2 Vapor pressure data. 99
Table 5.3 Measurement of number and projected area of NPs from in situ STEM images. 109

LIST OF ABBREVIATIONS

Abbreviation	Definition
2D	Two dimensional
3D	Three dimensional
4D	Four dimensional
ABF	Annular bright field
AC-TEM	Aberration-corrected transmission electron microscopy
AI	Artificial intelligence
BF	Bright field
CCDs	Charge-coupled devices
CNN	Convolution neutral network
DF	Dark field
DL	Deep learning
EDS	Energy dispersive X-ray spectroscopy
EELS	Electron energy loss spectroscopy
EM	Electron microscopy
ETEM	Environmental transmission electron microscopy
fcc	Face centered cubic
FFT	Fast Fourier transform
FIB	Focused ion beam
GAN	Generative adversarial network
HAADF	High angle annular dark field

HEA	High entropy alloy
HEMs	High entropy materials
HEO	High entropy oxide
HRTEM	High-resolution transmission electron microscopy
ICP-MS	Inductively coupled plasma mass spectrometry
LCTEM	Liquid cell transmission electron microscopy
MEMS	Microelectromechanical system
ML	Machine learning
NPs	Nanoparticles
ORR	Oxygen reduction reaction
PEMFC	Proton exchange membrane fuel cells
RT	Room temperature
SAED	Selected area electron diffraction
STEM	Scanning transmission electron microscopy
TEM	Transmission electron microscopy
TM	Transition metal

ACKNOWLEDGEMENTS

I would like to express the deepest appreciation to my committee chair, Associate Professor Kai He, whose guidance and advice carried me through all stages of working on my research. Without his persistent help this dissertation would not have been possible.

I would like to thank my committee members, Distinguished Professor Julie Schoenung and Assistant Professor William Bowman for serving on my committee. Their feedback on my work and their help with my career was much appreciated.

In addition, a thank you to colleagues and friends at University of California, Irvine. I would like to thank undergraduate students Karthik Iyer and Neelansh Khare in the He research group for their work on machine learning for images analysis. I also acknowledge the use of facilities and instrumentation at the UC Irvine Materials Research Institute (IMRI), which is supported in part by the National Science Foundation through the UC Irvine Materials Research Science and Engineering Center (DMR-2011967). I would like to thank the staff members Dr. Toshihiro Aoki and Dr. Mingjie Xu for their help with my electron microscopy work.

This research also used the Electron Microscopy facility of the Center for Functional Nanomaterials (CFN), which is a U.S. Department of Energy Office of Science User Facility, at Brookhaven National Laboratory under Contract No. DE-SC0012704. I would like to thank the staff scientists Dr. Sooyeon Hwang and Dr. Kim Kisslinger for their help with my experiments.

Financial support was provided by the American Chemical Society Petroleum Research Fund under Grant No. 62493-DNI10. Portion of Chapter 2 and 3 of this dissertation is a reprint of the material as it appears in "In situ transmission electron microscopy and artificial intelligence enabled data analytics for energy materials" [Zheng, H.; Lu, X.; He, K., Journal of Energy Chemistry 2022, 68, 454-493], used with permission from Elsevier. The co-authors listed in this publication are Hongkui Zheng and Kai He. Portion of Chapter 3 is a reprint of the material as it appears in "Machine Learning Enhanced Image Segmentation for High-Fidelity STEM Data Analysis" [Lu, X.; He, K., Microscopy and Microanalysis 2023, 29 (S1), 1895-1896], used with permission from Oxford University Press. The co-author listed in this publication is Kai He. Chapter 4 is a reprint of the material as it appears in "In Situ TEM for Structural and Chemical Evolutions of Bimetallic Pt-Ni Nanoparticles at Elevated Temperatures: Implications for Heterogeneous Catalysis" [Lu, X.; Hwang, S.; He, K., ACS Applied Nano Materials 2024, 7 (13), 15735-15742], used with permission from American Chemical Society. The co-authors listed in this publication are Sooyeon Hwang and Kai He.

Finally, my appreciation goes out to my family and friends for their encouragement and support through my studies.

VITA

Xiner (Lucy) Lu

EDUCATION

University of California, Irvine, Irvine, CA — Sep 2022 – Sep 2024

Doctor of Philosophy in Materials Science and Engineering

Clemson University, Clemson, SC — Aug 2019 – May 2022

Master of Science in Materials Science and Engineering

Southern University of Science and Technology, Shenzhen, China — Sep 2015 – Jun 2019

Bachelor of Engineering in Materials Science and Engineering

FIELD OF STUDY

Nanoparticles, metallic, in situ TEM, core–shell, solid solution, heterogeneous catalysts

PUBLICATIONS

Li, Q.; Ho, H.-P.; Zeng, Z.; Li, W.; Wang, Q.; Dong, K.; Tantratian, K.; Chen, L.; Rousse, G.; Lu, X.; He, K.; Chen, Y.; Han, K. S.; Thieu, N. A.; Chen, X.; Zhang, D.; Tian, H.; Wang, Y.; Ma, L.; Frost, M.; An, K.; Hu, S.; Li, W.; Luo, J.; Li, X.; Hu, L.; Wang, J.-H.; Liu, X. Local structural distortion and energy gradient enhance lithium ionic conductivity in Li-poor high-entropy oxide. J. Am. Chem. Soc 2024, under review.

Cao, L.; Soto F. A.; Li, D.; Deng, T.; Hu, E.; Cullen, D. A.; Lu, X.; Zachman, M. J.; Eidson, N.; Yang, X.; He, K.; Balbuena, P. B.; Wang, C., Single-atom Pd-Ru pair on Pt surface for promoting hydrogen oxidation in alkaline media. Nature Communications 2024, accepted.

Lu, X.; Hwang, S.; He, K., In Situ TEM for Structural and Chemical Evolutions of Bimetallic Pt–Ni Nanoparticles at Elevated Temperatures: Implications for Heterogeneous Catalysis. ACS Applied Nano Materials 2024, 7 (13), 15735-15742.

Yu, S.-W.; Kwon, S.; Chen, Y.; Xie, Z.; Lu, X.; He, K.; Hwang, S.; Chen, J. G.; Goddard III, W. A.; Zhang, S. Construction of a Pt-CeO_x Interface for the Electrocatalytic Hydrogen Evolution Reaction. Adv. Funct. Mater 2024, 2402966.

Lu, X.; He, K., Machine Learning Enhanced Image Segmentation for High-Fidelity STEM Data Analysis. Microscopy and Microanalysis 2023, 29 (S1), 1895-1896.

Lu, X.; He, K., Transformation during In Situ Heating of Bismuth Antimony Telluride Nanoplates. Microscopy and Microanalysis 2022, 28 (S1), 2284-2286.

Zheng, H.; Lu, X.; He, K., In situ transmission electron microscopy and artificial intelligence enabled data analytics for energy materials. Journal of Energy Chemistry 2022, 68, 454-493.

Lu, X.; He, K., Temperature-Dependent Structural Evolution of Pt-Ni Nanoparticles Observed by In Situ TEM. Microscopy and Microanalysis 2021, 27 (S1), 1236-1237.

Chen, M.; Cullen, D. A.; Karakalos, S.; Lu, X.; Cui, J.; Kropf, A. J.; Mistry, H.; He, K.; Myers, D. J.; Wu, G., Single Atomic Iron Site Catalysts via Benign Aqueous Synthesis for Durability Improvement in Proton Exchange Membrane Fuel Cells. Journal of The Electrochemical Society 2021, 168 (4), 044501.

Rashti, A.; Lu, X.; Dobson, A.; Hassani, E.; Feyzbar-Khalkhali-Nejad, F.; He, K.; Oh, T.-S., Tuning MOF-Derived Co_3O_4/$NiCo_2O_4$ Nanostructures for High-Performance Energy Storage. ACS Applied Energy Materials 2021, 4 (2), 1537-1547.

ABSTRACT OF THE DISSERTATION

Thermally Induced Evolutions of Metallic Nanoparticles
Through In Situ Transmission Electron Microscopy
by
Xiner (Lucy) Lu
Doctor of Philosophy in Materials Science and Engineering
University of California, Irvine, 2024
Associate Professor Kai He, Chair

Platinum-based metallic NPs hold considerable interest due to their applications especially in catalysis. The catalytic performance depends on their morphology, structure, and composition. The response under thermal stimuli remains complex and is not fully elucidated. TEM is an indispensable method for characterizing materials from the atomic level to nanoscale. In situ TEM has enabled unprecedented capabilities for observing the real-time evolution of materials during dynamic processes. This study investigates the thermally induced structural and chemical evolutions of Pt-based NPs with different structures and elemental compositions using in situ TEM. In situ TEM generates massive datasets, necessitating effective tools for data analysis. Image segmentation using machine learning was developed to analyze STEM images and quantify NPs behavior at elevated temperatures.

The first NP system investigated is Pt-Ni NPs. We synthesized NPs with two distinct structures. In situ TEM reveals morphological evolution from truncated octahedron to spherical-like isotropic shapes, followed by pancake-like ellipsoid shapes. In situ STEM with EDS mapping shows that solid-solution compositional configuration is retained over a large temperature range, while core-shell NPs undergo irreversible solid-solution transitions through chemical homogenization at elevated temperatures.

The study extends to quinary PdCuPtNiCo NPs with core-shell and HEA structures. STEM and EDS mapping examine the crystal structure and mixing patterns. In situ experiments reveal that chemical evolutions during heating are controlled by mass transfer with nearby NPs. Without mass transfer, NPs maintain their solid solution structure; however, mass transfer with background atom clusters or neighboring NPs leads to the formation of Janus structures after heating.

Overall, this work provides new scientific knowledge about structural and chemical evolutions of metallic NPs model systems during heat treatment. The obtained knowledge can be used as design principles to extend to other multimetallic systems to improve materials' performance in real applications.

CHAPTER 1 Introduction

1.1 Metallic Nanoparticles

Nanotechnology plays a crucial role in numerous fields, allowing us to manipulate molecules and atoms to create specific structures. NPs are tiny solid particles, typically on the nanometer scale, with exceptional physicochemical properties [1]. Nanocrystals are a type of crystal that have at least one dimension between 1 and 100 nm and are characterized by a single-domain crystalline structure without the complexity of grain boundaries. The interest in nanocrystals is rising due to their unique role as intermediaries between atoms and bulk solids, as well as their remarkable properties and potential uses [2]. Notably, many of these applications require metals in a nanoscale form, ideally as nanocrystals with precisely controlled characteristics.

Metallic materials are widely used in various industrial applications including aerospace, automotive, energy storage and conversion due to their excellent mechanical and physicochemical properties [3]. As complexity increases, metallic materials including monometallic, bimetallic, multimetallic (≥3 elements), and high-entropy (≥5 principal elements) alloys (HEAs) have received significant attention due to their advantageous catalytic, electrical, structural, magnetic and optical properties [4]. However, their performances largely depend on their shapes, sizes, crystal structures, chemical compositions and so on.

1.1.1 Controlled Shape

The diversity of shapes that metallic NPs have is extensive, with each shape offering unique properties and advantages for specific applications [5]. The controlled synthesis of

these shapes leverages thermodynamic and kinetic factors, as well as the use of surfactants and ligands. A wide range of shapes has been successfully created, encompassing not only basic geometries such as spheres, cubes, tetrahedrons, octahedrons, decahedrons, and icosahedrons, but also 1-dimensional and 2-dimensional forms like rods, wires, plates, discs, triangular and hexagonal plates. Additionally, more complex structures such as bipyramids, tetrapods, and hyper-branched shapes have also been achieved [6]. As shown in Figure 1.1, shape-controlled synthesis of metal NPs involves a meticulous process that begins with monomers and progresses through the stages of seed formation, nucleation, and growth. Initially, metal precursors (monomers) are reduced in a controlled environment to form small clusters of atoms, known as seeds. These seeds serve as the nucleation sites where the NPs begin to take shape. The nucleation phase is critical, as it determines the initial size and distribution of the particles. By manipulating factors such as temperature, concentration of precursors, and the presence of surfactants or capping agents, people can direct the uniform formation of seeds. During the growth phase, these seeds undergo further atomic deposition, where additional metal atoms are added, leading to the enlargement of the NPs. The growth phase is where the final shape of the NPs is established, heavily influenced by the kinetics of atom deposition and the selective binding of surfactants to specific crystallographic facets. This selective binding can inhibit growth in certain directions, allowing for the synthesis of NPs with controlled various shapes. Each stage from monomer to seed, through nucleation and growth, is finely tuned to achieve the desired morphology, enabling the tailoring of physical and chemical properties for specific applications [7].

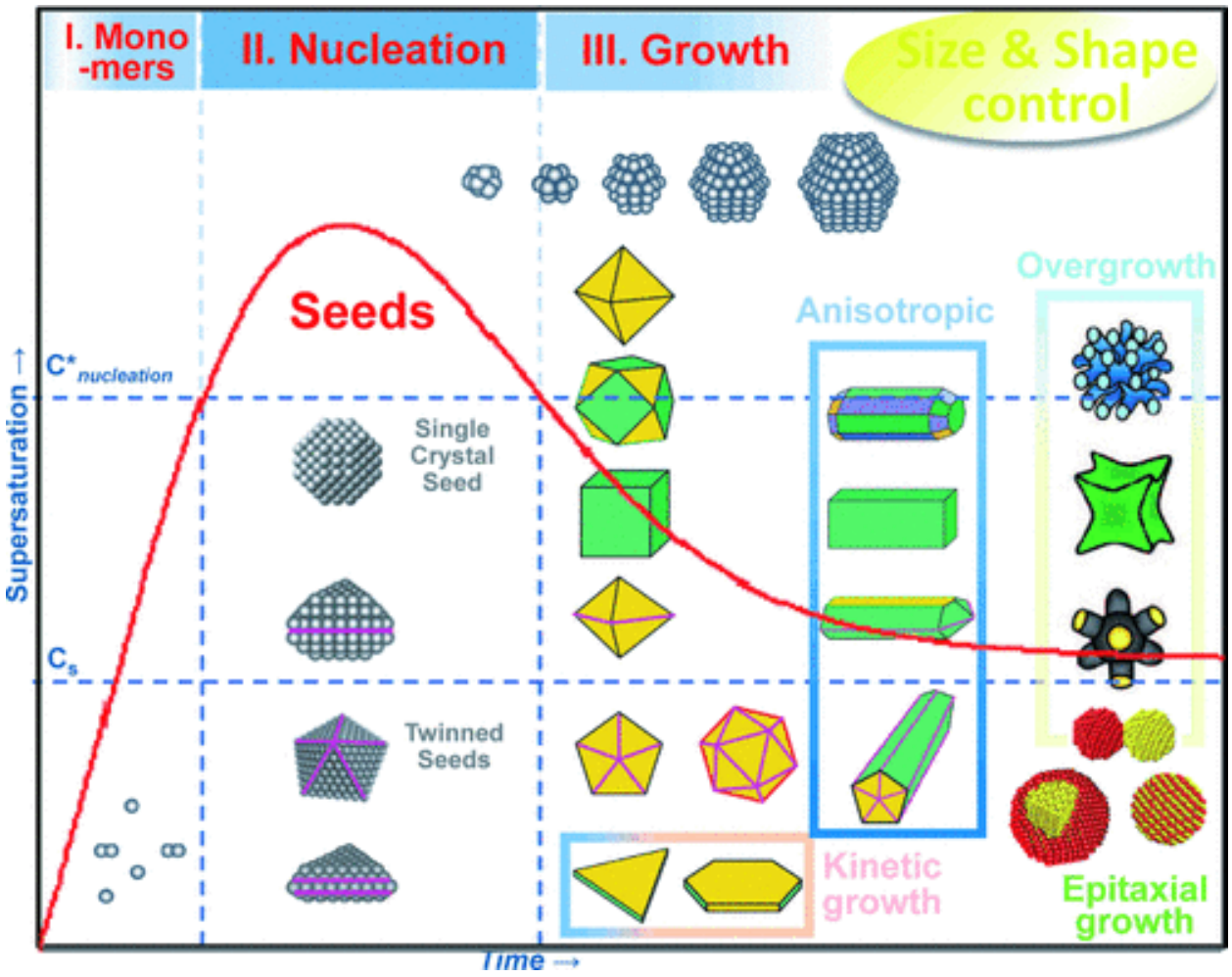


Figure 1.1 An illustration of general synthetic strategies for size and shape control of metal NPs [6]. Reproduced with permission. Copyright 2012, WILEY-VCH.

Figure 1.2 shows an example of TEM images of different shapes of synthesized Pt NPs. Cubic NPs, often synthesized using seed-mediated growth or controlled chemical reduction, expose high-energy {100} facets. These facets are active sites for catalytic reactions, making cubic NPs particularly useful in catalytic applications [8]. Octahedral NPs are characterized by their {111} facets, which typically exhibit lower surface energy than {100} facets. This shape is advantageous in applications requiring high surface stability and reduced agglomeration. Octahedral Pt-Ni NPs are known for their excellent catalytic properties in

oxygen reduction reactions [9]. Rod-shaped NPs, or nanorods, have an elongated structure with high aspect ratios. This shape provides a high surface area-to-volume ratio and anisotropic properties, which are beneficial for applications in optoelectronics and drug delivery [10, 11]. Nanowires are even more elongated than nanorods and are used in electronic and sensing applications due to their excellent electrical conductivity and high surface area. Metallic nanowires, such as Au-Ag and Pt-Pd, have shown promising results in biosensing and as components in nanoelectronic devices [12]. Branched or dendritic NPs have multiple arms extending from a central core, providing a large surface area and numerous active sites. This shape is advantageous for applications requiring extensive surface interactions, such as catalysis and sensing [13].

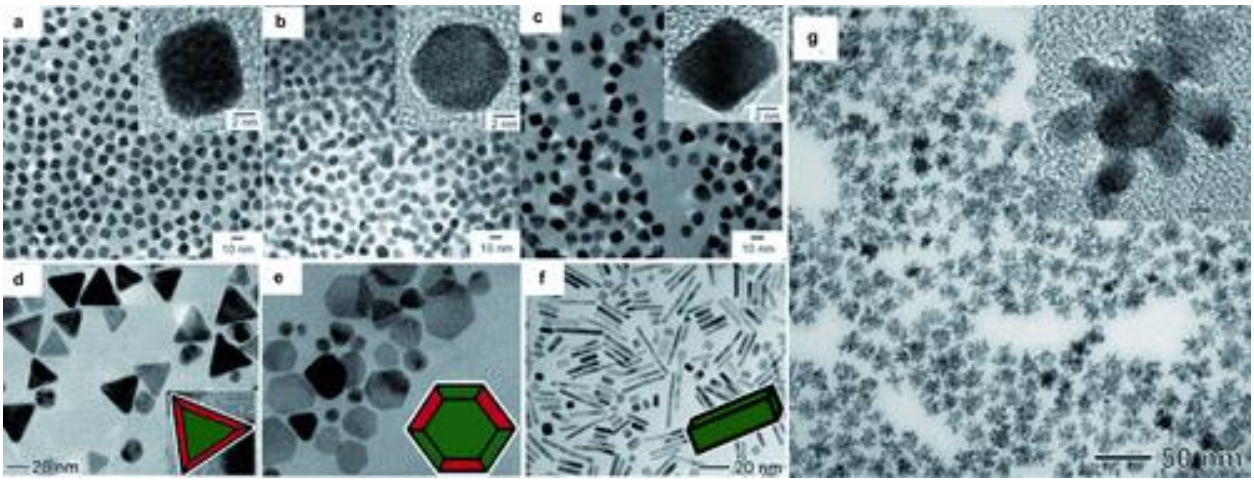


Figure 1.2 TEM and HRTEM images of shape-controlled NPs : a) Pt cubes, b) Pt cuboctahedra, c) Pt octahedra, d) Pd triangular plates, e) Pd hexagonal plates, f) Pd nanobars, and g) Pd-Pt bimetallic nanodendrites [6]. Reproduced with permission. Copyright 2012, WILEY-VCH.

The controlled shape of metallic NPs is a critical aspect of nanotechnology that significantly influences their properties and applications. The ability to manipulate NPs

morphology enables precise tailoring of their properties for diverse applications. However, the real-world utility of these materials extends beyond their initial synthesis. Under thermal and actual reaction conditions, NPs can undergo shape transformations that critically influence their performance and stability. For instance, high temperatures or reactive environments can cause reshaping, sintering, or dissolution of specific facets, altering their activity and efficiency [14]. Therefore, understanding and controlling these shape changes are vital for maintaining the desired properties and functionality of metallic NPs in practical applications.

1.1.2 Controlled Structure

The progression from monometallic to bimetallic and multimetallic NPs represents a significant development in nanomaterials, offering more control over structure and properties. Initially, monometallic NPs served as the building blocks for understanding fundamental synthesis principles and characterizing basic properties. However, incorporating a second constituent introduces additional compositional and structural complexities, resulting in bimetallic nanocrystals adopting various configurations. These configurations include ordered intermetallics, random alloys, core-shell structures, and more [15]. Figure 1.3 shows the simulations of EDS maps of seven different octahedral Pt-Ni NPs with different structures [16]. Alloy structure has a homogeneous distribution of two or more metals throughout the particle. These structures can exhibit enhanced catalytic, magnetic, or optical properties due to the synergistic effects between the constituent metals [17, 18]. Core-shell structure consists of a core of one metal surrounded by a shell of another. For multimetallic NPs, this structure can also be extended to multiple elements consisting of either core or shell [19]. This structure allows for the combination of core and shell

properties, such as enhanced stability, catalytic activity, and biocompatibility [20, 21]. Except for these structures shown in Figure 1.3, Janus structure features two distinct faces with different compositions or properties. This unique structure enables asymmetric functionality due to the presence of possible different metals on separate faces [22]. Hollow and porous structures have internal cavities, providing high surface area and low density. These structures are advantageous for catalytic applications where mass transport and surface interactions are critical [23, 24].

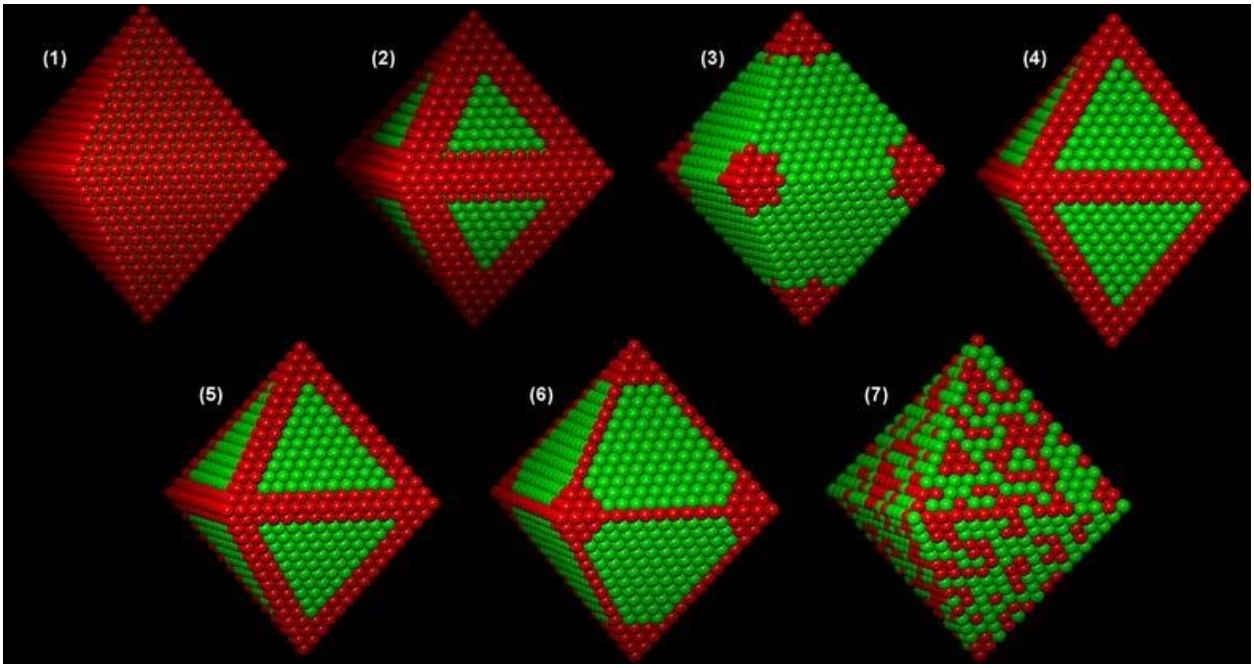


Figure 1.3 3D renderings of different NP structures. Pt atoms are shown in red and Ni atoms are shown in green. (1) Pt monolayer over a Ni core; (2) Pt edges over a Ni core; (3) Pt hexapod; (4) Pt hexapod and edges; (5) Pt hexapod, Pt edges and Pt core; (6) Ni facets that are not connected; (7) random alloy structure [16]. Reproduced with permission. Copyright 2018, Springer Nature.

Considering that complex structures may transform from one form to another when subjected to elevated temperatures, or other reaction conditions, both catalytic activity and stability can be significantly impacted. Hence, it is essential to comprehend these transformation pathways through in situ experiments.

1.1.3 Controlled Composition

The selection of metal elements incorporated into metallic NPs are crucial determinant of their properties and functionalities. The choice of metals is guided by the desired physical, chemical, and catalytic properties, as well as the application requirements. The combination and proportion of metals can significantly influence the stability, reactivity, and overall performance of the NPs.

Bimetallic Nanoparticles

Bimetallic heterogeneous nanocrystals composed of both noble metal and TM elements often demonstrate superior catalytic performance compared to single noble metal catalysts [25]. Nanoscale Pt–Ni bimetallic NPs with octahedral shape and controlled size have been actively explored in recent years due to their outstanding activity for ORR [26]. In 2007, Stamenkovic et al. found that the Pt_3Ni (111) surface is 10 times more active for the ORR than the Pt (111) surface, and 90 times more active than the Pt/C catalysts [27]. Zhang et al. successfully synthesized monodisperse Pt_3Ni nanoctahedra and nanocubes by co-reducing $Pt(acac)_2$ and $Ni(acac)_2$ in a mixed organic solvent of oleic acid and oleylamine [28].

The synthesis of metallic NPs has been a significant focus of research due to their unique properties and wide range of applications. Achieving precise control over the composition, size, morphology and structure of these NPs requires the use of sophisticated

synthesis methods. These methods can be categorized into two main types bottom up methods and top down methods, as listed in Table 1.1 [29].

Table 1.1 Top down methods and bottom up methods of NP preparation [29]. Reproduced with permission. Copyright 2019, Elsevier.

Sr. No.	Top down methods		Bottom up methods	
	Methods	Examples	Methods	Examples
1	Mechanical milling	Ball milling Mechanochemical method	Solid state methods	Physical vapor deposition Chemical vapor deposition
2	Laser ablation		Liquid state synthesis methods	Sol gel methods Chemical reduction Hydrothermal method Solvothermal method
3	Sputtering		Gas phase methods	Spray pyrolysis Laser ablation Flame pyrolysis
4			Biological methods	Bacteria Fungus Yeast Algae Plant extract
5			Other methods	Electrodeposition process Microwave technique Supercritical fluid precipitation process Ultra sound technique

High Entropy Alloy Nanoparticles

HEMs have received considerable critical attention in recent years due to their unique properties and wide applications led by the multielemental composition and solid-solution structure. By changing the added metal species and inducing the anion source, versatile HEMs could be obtained. In 2004, Yeh et al. introduced the concept of HEAs [30]. Based on

Boltzmann's hypothesis, the mixing configurational entropy during the formation of a solid solution from n elements with equimolar fractions can be calculated from equation (1), where R is the gas constant. According to the classifications in HEAs research, the multicomponent alloys which satisfy the requirement (2) can be named as HEAs [31]. For alloys with equal molar fractions with 3, 4, 5, 6 and 9 elements, their mixing entropy value ΔS_{mix} can be easily calculated as 1.10R, 1.39R, 1.61R, 1.79R and 2.20R, respectively. Therefore, only the alloys with more than 5 different kinds of metal elements and random mixing crystal structure can be defined as HEAs.

$$\Delta S_{mix} = -R \sum_n \frac{1}{n} ln \frac{1}{n} = Rlnn \quad (1)$$

$$\Delta S_{mix} > 1.5R \quad (2)$$

In recent years, the high phase and chemical stability under extreme environments caused by the unique crystal structure has made HEMs a promising candidate for energy conversion and storage applications. Bulk HEAs are difficult to use for catalytic applications due to their low surface area and low number of active sites. Compared with the bulk counterpart, HEA NPs with more than 5 kinds of metal elements and homogeneous mixing structure own large surface area and enriched catalytic active sites, therefore demonstrating excellent catalytic performances on both thermocatalysis and electrocatalysis reactions [32]. For example, Yao et al. successfully synthesized a library of HEA NPs by carbonthermal shock method and proved the catalytic utility with ~100% conversion and >99% nitrogen oxide selectivity as ammonia oxidation catalysts [33].

The most important property of HEAs is that they are single phase materials where entropic stabilization accounts for compositionally complex solid solution formation.

However, multimetallic NPs may have heterogeneous structure. Mirkin et al. made great progress in synthesizing multicomponent NPs through polymer nanoreactor–mediated synthesis and the obtained product had heterogeneous structure with phase segregation [34]. Skrabalak group reported the synthesis of quinary, senary, and septenary NPs comprised of PdCuPtNi with Co, Ir, Rh, Fe, and/or Ru with core-shell structure and conversion of two-phase core–shell NPs into single-phase HEA NPs by thermal treatment [35]. This demonstrates the ability to manipulate the degree of intermixing between the core and shell phases and the generality of this NP conversion strategy to monodisperse HEA NPs.

The primary key to synthesizing HEMs is adjusting their thermodynamic parameters to create homogeneous distribution of kinds of elements. HEMs with high surface area and abundant active sites are favorable for energy applications. However, the size, phase and elemental composition of the synthesized HEMs are highly dependent on the selection of synthesis approaches and parameters. I summarized the general methods in Figure 1.4.

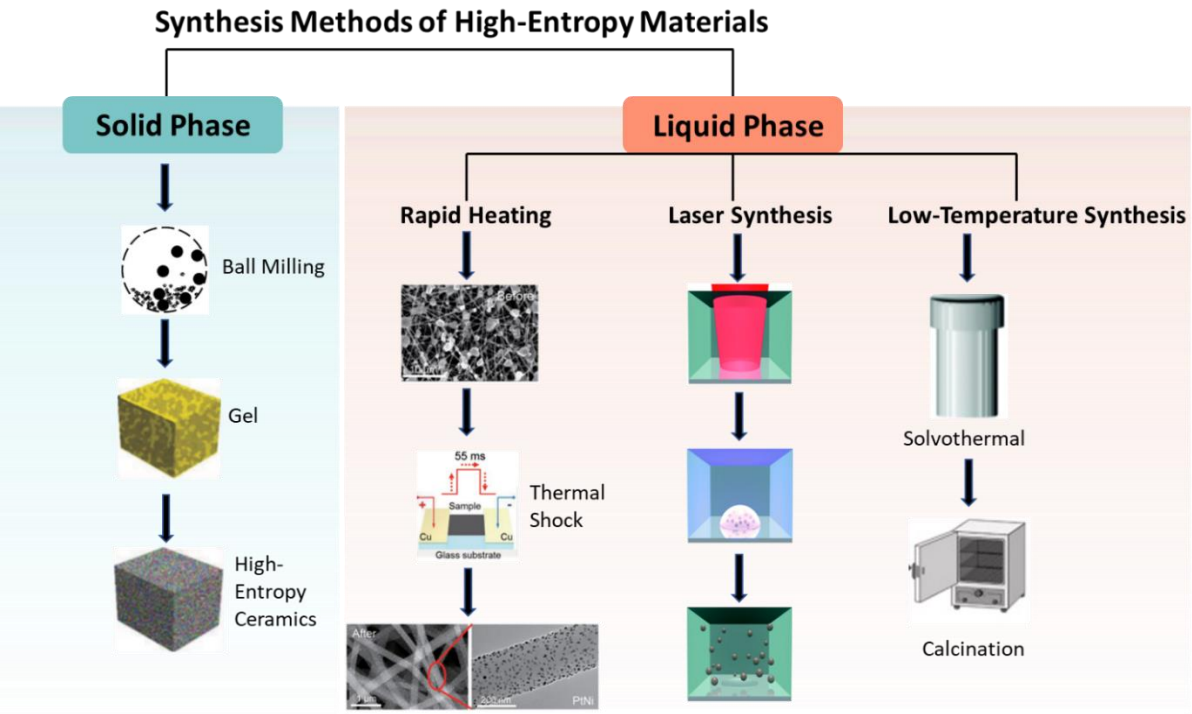


Figure 1.4 Summary of synthesis methods of HEMs divided into solid phase and liquid phase synthesis.

Mechanochemical synthesis to reorganize atoms from different elements into the same lattice is an efficient solid-state synthesis for HEMs. Wu et al. prepared CoCrFeNiPt and CoFeNiCrPd ingots using the vacuum arc melting method under argon atmosphere and then used spark discharge system to prepare HEA NPs [36]. Besides the solid phase precursors, aqueous precursor solutions are also widely applied to synthesize HEMs. The liquid-state synthesis of HEMs can be broadly classified into three main categories. The first one is increasing the temperature rapidly in seconds to shock the precursors and obtain high-entropy phases. Hu group at the University of Maryland first employed flash heating and cooling with temperature ~2000 K and shock duration ~55 ms of metal precursors on oxygenated carbon support to produce HEA-NPs with up to eight dissimilar metallic

elements [33]. They synthesized a wide range of multicomponent NPs with narrow size distribution and uniform dispersion by controlling the carbothermal shock parameters. It is noted that they used conductive carbon support, which are carbon nanofibers as substrate for the carbonthermal shock process. After the rapid shock, high concentration of metallic NPs formed across the carbon surface without agglomeration. On the one hand, the ultrafast heating is a nonequilibrium process which drives the particle "fission" and "fusion" events to achieve uniform mixtures. On the other hand, the rapid cooling rate 10^5 K/s dominate the kinetic control and avoid phase segregation [33]. Similarly, this rapid heating route has also been developed in various forms to synthesize HEMs such as PtPdFeCoNi HEA-NPs by microwave heating [37], HEO microparticles by Joule heating [38]. Pyrolysis can also be applied to the synthesis of HEM NPs in high temperatures, including fast moving bed pyrolysis to prepare denary MnCoNiCuRhPdSnIrPtAu HEA-NPs and flame spray pyrolysis to obtain quinary $(Mn, Fe, Ni, Cu, Zn)_3(O)_4$ HEO NPs [39, 40]. Instead of drying solution on carbon support, continuous synthesis using aerosol droplets for fast heating and quenching treatment is more suitable for large-scale production [41] [24]. Similarly, vapor phase spark discharge method enables the precursors to a direct vapor-crystal transformation to confine the NPs in their alloyed states [42]. Ultrasound irradiation process is able to produce instantaneous massive energy in momentary timespans, meeting the rapid heating requirement to form multimetallic NPs and high-entropy perovskite oxides [43, 44].

Besides the ultrafast heating and cooling synthetic methodologies to reach nonequilibrium process and achieve uniform dispersed HEM NPs, Waag et al. reported a laser synthesis of colloidal CoCrFeMnNi HEA NPs [45]. They first prepared HEA bulk target by mixing and heat treatment, and then applied a laser beam to irradiate the surface of the

target. Through the laser ablation, a cavitation bubble formed and the ablated species condensed and released as HEA NPs in the liquid. The scalability and reproducibility with 3 grams of colloidal HEA NPs have also been proved using this method [45]. Concurrent chemical reduction of platinum-group metals in organic solvents can form solid-solution HEA [46]. Mori et al. utilized hydrogen spillover phenomenon with TiO_2 to obtain supported HEA NPs [47].

1.2 Application of Metallic Nanoparticles

The production and consumption of energy are closely linked to global climate change. Presently, most energy consumption relies on fossil fuels. However, these non-renewable resources are depleting rapidly, and the combustion of large quantities of fossil fuels generates significant pollutants, leading to greenhouse effects, acid rain, and other severe environmental issues [48, 49]. The traditional energy structure and low utilization rates cannot meet the future demands for efficient, clean, economical, and safe energy in a sustainable society. Consequently, there has been a growing exploration of renewable and clean energy sources, such as solar, wind, geothermal, and ocean energy [50]. To promote the development of new energy, energy conversion and storage materials play an important role in extending interest in energy devices such as lithium-ion batteries, fuel cells and perovskite solar cells [51, 52].

Catalysis is fundamental to the chemical and petroleum industries, playing a crucial role in a wide range of chemical reactions and processes that support clean energy and environmental sustainability [53]. Catalysts can be classified into two types: homogeneous and heterogeneous. Homogeneous catalysts exist in the same phase as the reactants,

typically in solution. An example is soluble organometallic compounds acting as catalysts in hydrogenation [54]. In contrast, heterogeneous catalysts are in a different phase than the substrates; for instance, a solid catalyst might accelerate a reaction involving liquid or gas phase reactants [55].

Both types of catalysts have their advantages and disadvantages, as summarized in Table 1.2. The active centers of homogeneous catalysts are all metal atoms, which provide high selectivity. They operate under relatively mild reaction conditions but have low thermal stability and limited applicability, and product separation is challenging. However, their reaction mechanisms are easier to understand.

Heterogeneous catalysts, on the other hand, have active centers that are only surface atoms. They tend to have lower selectivity and often require more severe reaction conditions, but they possess high thermal stability and wide applicability. Product separation is easier with heterogeneous catalysts, though their reaction mechanisms are less well understood. Many catalytic reactions depend on heterogeneous catalysts, including metals, metal oxides, and metal salts. Noble metals such as Pt, Pd, Rh, and Ir are exceptional heterogeneous catalysts, though they are costly and scarce. TMs like Ni, Cu, Co, and Fe are also widely used as catalysts. Therefore, combining noble metals and TMs in catalysts can potentially offer excellent catalytic properties while reducing costs [56].

Table 1.2 Comparison of homogeneous catalysts and heterogeneous catalysts.

	Homogeneous	Heterogeneous
Active centers	all metal atoms	only surface atoms
Selectivity	high	low
Reaction condition	mild (50-200°C)	Severe (often>250°C)
Thermal stability	low	high
Applicability	limited	wide
Product separation	difficult	easy
Reaction mechanism	reasonably well understood	poorly understood

Among noble metals, Pt exhibits exceptional catalytic activities across numerous applications, such as automotive exhaust gas treatment, petroleum refining, organic synthesis, hydrogen production, and PEMFC [57, 58]. ORR is a critical half-cell reaction in chemistry, particularly for PEMFCs, where oxygen molecules react with protons and electrons to form water. Improving catalysts for ORR is a major focus because of its slow kinetics and significant potential loss. Additionally, the cathode in PEMFCs typically requires a higher Pt loading, often several times that of the anode. However, Pt resources are limited, necessitating strategies to reduce Pt usage and enhance catalytic activities by designing specific Pt-based nanomaterials [59].

Pt-based nanomaterials, compared to their bulk counterparts, have a significantly increased specific surface area and a greater number of exposed active sites, leading to much higher Pt atom utilization. Various strategies have been developed to optimize these

nanostructures and further enhance their catalytic properties [60]. These strategies include incorporating another TM element to create Pt-based alloys, core-shell, or heterogeneous structures, controlling exposed crystal facets, developing three-dimensional nanostructures like hollow spheres and nanoframes, and utilizing support materials with stable structures, high specific surface areas, and more anchoring sites [9, 23].

The suitability of a catalyst for a specific process is primarily determined by three catalytic properties: activity, selectivity, and stability. These properties are intrinsically dependent on the catalyst's structure, morphology, and composition [61]. From a materials science perspective, a fundamental understanding of the structure-property relationship and the evolution of material structure and chemistry at relevant length and temporal scales is crucial and urgent for the rational design of energy-related applications.

1.3 Fundamental Concepts

Understanding the thermal-induced evolutions of metallic NPs requires a solid understanding of several key phenomena: metal interdiffusion, surface energy-driven coalescence and growth, and phase stability and intermetallic formation. These concepts provide the foundation for explaining observed behavior.

1.3.1 Metal Diffusion

Metal diffusion is a key phenomenon in alloy systems, where atoms from different metals migrate into each other. This process significantly impacts the structural and functional properties of metallic NPs, especially at elevated temperatures. The diffusion process in metals can be described using Fick's laws. Fick's first law states that the diffusion

flux, J, which is the amount of substance that flows through a unit area per unit time, is proportional to the concentration gradient:

$$J = -D\frac{d\varphi}{dx}$$

where J is the diffusion flux, D is the diffusion coefficient, φ is the concentration, and x is the position. Atomic diffusion can be driven by concentration gradients or surface energy minimization. Diffusion driven by concentration gradients follows Fick's laws, where atoms move from regions of high concentration to low concentration, leading to homogenization over time. This type of diffusion is quantified by the diffusion coefficient and can be described by Fick's second law:

$$\frac{\partial\varphi}{\partial t} = D\frac{\partial^2\varphi}{\partial x^2}$$

The diffusion coefficient D is temperature-dependent and follows an Arrhenius relationship:

$$D = D_0\exp\left(\frac{-Q}{RT}\right)$$

where D_0 is the pre-exponential factor, Q is the activation energy for diffusion, R is the universal gas constant, and T is the absolute temperature [62].

The diffusion of elements within NPs is influenced by their diffusion coefficients values, atomic sizes, and electronegativities. Elements with higher diffusion coefficients will migrate more rapidly, particularly under thermal conditions. Here, the diffusion coefficients of the further studied metal elements are summarized in Table 1.3, which displays the diffusivity data for Ni-X dilute systems, where X represents different solute elements [63]. The table provides D_0 and Q values at two different temperature points (700 K and 1700 K),

showcasing how these parameters change with temperature. Cu exhibits the highest diffusion coefficients among the four metals, indicating rapid diffusion within the Ni lattice. The lower activation energy further facilitates this process, especially at elevated temperatures. This suggests that Cu can quickly homogenize within Ni, impacting phase formation and potentially reducing the stability of distinct phases. Pt has relatively low diffusion coefficients and relatively high activation energy, indicating slower diffusion within the Ni lattice compared to Cu and Pd but faster than Co. This suggests that Pt atoms will migrate less readily compared to Cu and Pd, potentially leading to the formation of stable Pt-rich regions. Co exhibits the lowest diffusion rates in Ni among the four metals, with a significant increase in diffusivity at higher temperatures. The high activation energy suggests that considerable thermal energy is required for Co atoms to diffuse within the Ni lattice. Overall, rapid diffusing elements like Cu can quickly homogenize, ensuring a uniform distribution. However, the slower diffusion of Co and Pt can maintain distinct regions. The diffusion behavior of these metal elements highlights the diverse effects they can have on the thermal evolution and stability of multimetallic NPs.

Table 1.3 Diffusion parameters for the solute diffusion of Ni-X systems [63].

Solute	D_0 (10^4 m^2/s)	Q (eV)	T (K)
Pd	0.141	2.74	700
	0.432	2.72	1700
Cu	0.254	2.85	700
	0.620	2.75	1700
Pt	0.090	2.94	700
	0.275	2.95	1700
Co	0.085	3.07	700
	0.243	3.09	1700

1.3.2 Surface Energy

Surface energy is a fundamental concept in materials science, particularly significant for understanding the behavior of metal NPs. The surface energy of a material is the excess energy at the surface of a solid compared to the bulk. This concept is crucial because NPs have a high surface-to-volume ratio, making surface energy a dominant factor in determining their properties and stability. Surface energy (γ) can be defined as the energy required to create a unit area of a surface. For metals, this energy arises from the disruption of atomic bonds at the surface, leading to higher energy states compared to the atoms in the bulk. Mathematically, surface energy is expressed as:

$$\gamma = \frac{dW}{dA}$$

where dW is the work done to create a new surface area dA [64].

The high surface energy of metal NPs tends to drive changes in morphology to minimize the total surface energy. This can lead to phenomena such as facet development and rounding of edges. As NPs reduce their surface energy, they may undergo shape transformations, which is critical in applications like catalysis where specific surface facets exhibit different catalytic activities [65]. Atomic diffusion driven by surface energy minimization involves the migration of atoms to reduce the system's overall surface energy. For example, Ostwald ripening involves the dissolution of smaller NPs and redeposition of material onto larger ones, driven by the reduction in total surface energy. The larger particles grow at the expense of smaller ones, leading to a more thermodynamically stable distribution of particle sizes [66]. Adjacent NPs may coalesce to form larger particles. This process reduces the total surface area and thus the total surface energy. Coalesce would

reduce the active surface area for catalytic reactions and further decrease the performance [67]. Surface energy also influences the phase stability of NPs. For instance, in multimetallic NPs, the different surface energies of the constituent metals can lead to surface segregation, where one metal preferentially occupies the surface. Intermetallic formation in NPs can also be driven by surface energy considerations. The surface energy of intermetallic phases can be different from that of pure metals, influencing the formation and stability of these phases.

The surface energies of representative facets for the studied metals are shown in Table 1.4 [68]. The weighted surface energy ($\bar{\gamma}$) is defined by the following equation:

$$\bar{\gamma} = \frac{\sum_{\{hkl\}} \gamma_{hkl} A_{hkl}}{\sum A_{hkl}} = \sum_{\{hkl\}} \gamma_{hkl} f_{hkl}^{A}$$

where γ_{hkl} is the surface energy for a unique facet, A_{hkl} is the total area of all facets in the {hkl} family, and f_{hkl}^{A} is the area fraction of the {hkl} family. The shape of metals significantly influences their surface energy, which in turn affects their stability, growth, and properties. Different facets such as {111}, {110}, and {311} planes exhibit varying surface energies due to differences in atomic density and coordination. For instance, in fcc metals, the {111} facet typically has lower surface energy compared to other facets, making it more stable and energetically favorable. This anisotropy in surface energy leads to the formation of NPs with specific shapes that minimize the overall surface energy, such as octahedra, which are bound by {111} facets. In our study, we focus on the fcc structure, commonly observed in metals like Pt, Ni, and their alloys.

Pd and Cu have relatively low surface energies, which implies that in a multimetallic NP, these metals are less likely to migrate to the surface to minimize total surface energy. Pt

has moderate surface energy. Therefore, Pt atoms can migrate to the surface but not as dominantly as Ni or Co. Ni and Co have the highest surface energies among the selected metals. This makes them prone to surface segregation in multimetallic NPs to reduce the overall surface energy.

Table 1.4 Surface energy values and lattice constants of selected metal elements [68].

Element	Facet	Surface energy (J/m^2)	Weighted surface energy (J/m^2)	Lattice constant (Å)
Pd	(111)	1.36	1.45	3.8898
	(100)	1.52		
	(311)	1.57		
	(331)	1.53		
	(210)	1.63		
	(221)	1.50		
Cu	(111)	1.34	1.42	3.61496
	(100)	1.47		
	(311)	1.54		
	(331)	1.52		
	(210)	1.60		
	(221)	1.48		
Pt	(111)	1.49	1.60	3.9231
	(100)	1.86		
	(311)	1.79		
	(331)	1.71		
	(210)	1.89		
	(221)	1.60		
Ni	(111)	1.92	2.04	3.52387
	(100)	2.21		
	(311)	2.30		
	(331)	2.23		
	(210)	2.40		
	(221)	2.17		
Co	(111)	2.04	2.15	3.548
	(100)	2.48		
	(311)	3.28		
	(331)	3.64		
	(210)	4.36		
	(221)	2.33		

In catalytic applications, the surface reconstruction of NPs under reaction conditions can alter the catalytic performance. Understanding and controlling surface energy is thus essential for optimizing catalysts' properties.

1.3.3 Phase Stability

Phase stability in multimetallic systems is governed by thermodynamic principles, particularly Gibbs free energy (G). The stability of a phase is determined by its Gibbs free energy, which is a function of enthalpy (H), entropy (S), and temperature (T).

$$G = H - TS$$

A phase is stable if it has the lowest Gibbs free energy under given conditions. In multimetallic systems, the Gibbs free energy depends on the interactions between different atomic species, their concentrations, and temperature.

Enthalpy represents the total heat content of the system, including bond energies between atoms. In multimetallic NPs, the enthalpy of mixing (ΔH_{mix}) is crucial, which can be positive or negative depending on whether the mixing is endothermic or exothermic. For example, if two kinds of atoms mix favorably, the enthalpy of mixing is negative, promoting a homogeneous alloy phase. Entropy measures the disorder of the system. In multimetallic NPs, the configurational entropy (ΔS_{config}) is significant, representing the number of ways atoms can be arranged. At higher temperatures, the entropy term ($-TS$) becomes more significant, favoring phases with higher disorder. This can lead to a tendency towards homogeneity at elevated temperatures as atoms become more randomly distributed.

Phase diagrams are graphical representations of the equilibrium between different phases in a multicomponent system as a function of composition and temperature. These diagrams provide valuable insights into the stability of different phases, mapping the stable phases at varying compositions and temperatures. For instance, binary phase diagrams illustrate the phase behavior of systems with two components. Figure 1.5 shows three binary phase diagrams [69]. Taking Pt-Ni as an example, at lower temperatures, it showes ordered intermetallic phases like $PtNi_3$, PtNi, and Pt_3Ni, which are indicated by distinct phase boundaries. As the temperature increases, the system tends towards a disordered solid solution due to increased entropy, where the atomic arrangement becomes more random.

In contrast, ternary phase diagrams, such as the Fe-Ni-Pt system shown in Figure 1.5, involve three components and thus provide a more complex representation of phase equilibria [69]. These diagrams show not only the regions of single-phase stability but also the interactions between the three elements, leading to the formation of various solid solutions and intermetallic compounds. The increased complexity of ternary systems results in more intricate phase boundaries and regions where multiple phases coexist.

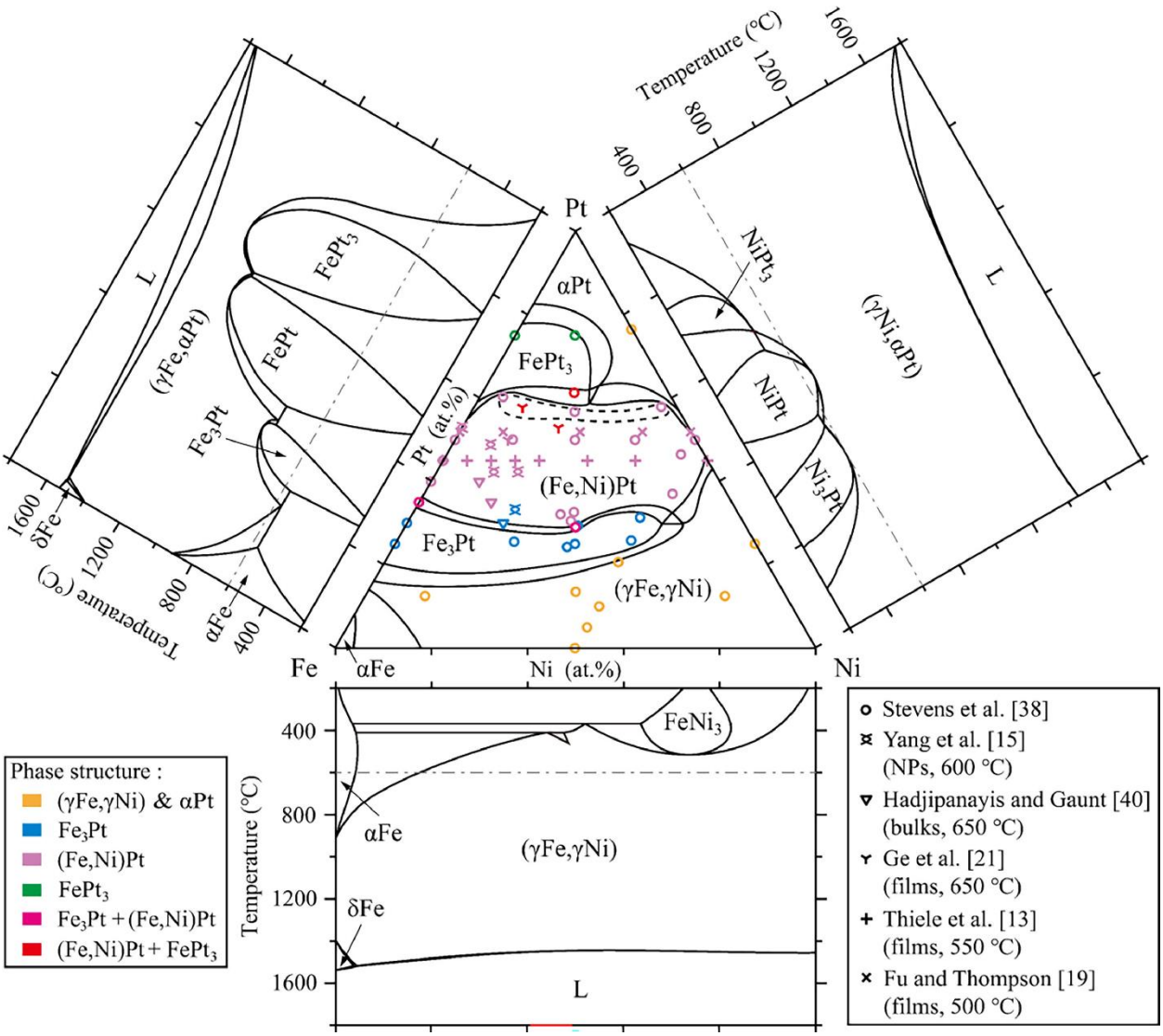


Figure 1.5 Isothermal section of the Fe–Ni–Pt system at 600 °C with three constituent binary phase diagrams [69]. Reproduced with permission. Copyright 2024, Elsevier.

As the complexity of the system increases, the likelihood of phase separation also increases. This is because the addition of more components introduces more variables, which affect the overall stability of the system. The presence of multiple components increases the chances of phase segregation, where regions within the material become enriched in certain elements, leading to heterogeneous structures. Phase segregation occurs

when different elements in a multimetallic NP separate into distinct regions or phases rather than forming a homogeneous mixture. Several factors can drive phase segregation.

1) Lattice strain: Lattice strain is a measure of the distribution of lattice constants arising from crystal imperfections, such as lattice dislocation. This strain can drive segregation to minimize the energy. For example, it has been used to create a phase-separated and strained Pd–Rh heterostructure [70].

2) Temperature: At lower temperatures, the enthalpy term dominates, favoring phase separation if mixing is energetically unfavorable. At higher temperatures, the entropy term becomes significant, promoting homogeneity as the system seeks to maximize entropy.

3) Surface energy: The surface energy of different metals can lead to segregation at the NP surface. Metals with lower surface energies may preferentially occupy the surface, while those with higher surface energies migrate to the interior or form distinct phases.

By understanding phase stability and controlling the synthesis conditions, researchers can design NPs with desired phases and properties. This is particularly important for multimetallic NPs, where multiple elements contribute to complex phase behaviors.

1.4 Motivation

The study of metallic systems has evolved over time from simple monometallic materials to more complex bimetallic materials and now to HEAs. The increased complexity of metallic materials allows for a greater range of potential properties and their development has led to the discovery of new materials with desirable properties for various applications. Regardless of the working reactions, the thermal stability of these materials has always been

a major problem for academic and industrial research, as the compositions and surface structures of crystals under working scenarios are subjected to increased temperatures. Thermal response at high working temperatures is important for improving the design and reliability of metallic materials. People have investigated the shape change of bimetallic NPs in the past [71, 72]. Gocyla et al. reported a morphological evolution sequence, with the transformation from concave octahedra to truncated octahedra or cuboctahedra [71]. Gan et al. revealed a surface evolution in which Pt-rich surface atoms diffused and covered the concave Ni-rich {111} surfaces [72]. While these studies investigated shape stability, they primarily concentrated on the morphological and surface evolution and less on the internal compositional changes. The lack of investigations into compositional change inside NPs causes the mechanism by interaction between noble and TM has not been fully established. In this research, by investigating metallic NPs with different degrees of complexity, we aim to study their temperature-dependent structural and chemical evolutions and provide a comprehensive understanding of the underlying mechanisms of these evolutions. The results of this research will be useful for designing new materials that can withstand extreme thermal conditions and for improving the stability and efficiency of existing materials. The research aims to answer the following key questions:

1) How will different structures and phases evolve during the thermal treatment process?

2) How will different metallic elements change their spatial distributions at elevated temperatures?

3) How will a thermal process impact the relationship between structural transition and composition distribution?

To address these scientific questions, we formulate a central hypothesis that controlled thermal treatment provides effective tunability to change the order-disorder transitions in the composition complex metallic NPs and could provide insights into designing novel heterogeneous catalysts. We aim to test this hypothesis in two model systems, i.e., bimetallic Pt-Ni NPs and multimetallic PdCuPtNiCo NPs.

Based on the overarching hypothesis, we further formulate the following three specific hypotheses outlined below:

Hypothesis 1: NPs would undergo facet development to minimize the free energy with surface rounding at elevated temperatures. Specifically, we start with bimetallic Pt-Ni NPs with terminating {111} facets and study their morphological evolution during heating in Chapter 4.

Hypothesis 2: Constitutional elements tend to be homogenized due to entropic effects at elevated temperatures. Specifically, with controlled colloidal synthesis, homogeneous and heterogeneous structures could be obtained. Then the evolutions of both structures are observed in real time. The two distinct structures of both bimetallic Pt-Ni NPs and multimetallic PdCuPtNiCo NPs were studied in Chapters 4 and 5.

Hypothesis 3: The existence of two or more types of noble-metal or transition-metal elements would have extra synergetic effects in addition to the simple combination of the individual elemental contributions. Specifically, NPs with five elements are synthesized and investigated with phase transformation and segregation during heat treatment in Chapter 5.

The objectives of this research are to specifically test these hypotheses through case studies of well-defined model systems.

CHAPTER 2 Experimental Methods

Portion of this chapter is a reprint of the material as it appears in "In situ transmission electron microscopy and artificial intelligence enabled data analytics for energy materials" [Zheng, H.; Lu, X.; He, K., Journal of Energy Chemistry 2022, 68, 454-493], used with permission from Elsevier.

The synthesis and characterization of metallic NPs are fundamental to understanding their properties and optimizing their performance for various applications. This chapter aims to provide a comprehensive background on the hot injection synthesis method and TEM characterization method used in this study. Detailed experimental procedures are described in sections 4.2 and 5.2.

2.1 Synthesis Methods

Among the synthesis methods, liquid state synthesis including the hot injection method is a prominent technique that offers several advantages, including high crystallinity and uniform particle size. The hot injection method involves heating organic metal compounds and decomposing them at high temperatures condition to produce metallic NPs. This is a common method to obtain monodisperse nanocrystals [73]. The process of nucleation and growth is primarily affected by the reduction rate of metal ion precursors. The metal ions with higher reduction potential are more easily to be reduced. For example, as shown in Table 2.1, Ni^{2+} with lower E_o is harder to be reduced compared to Pt^{2+} [74].

Table 2.1 Reduction potentials of the metal ions.

Reduction reaction	E_o **(V vs SHE)**[a]
$Au^{3+} + 3e^- \rightarrow Au$	1.50
$Pt^{2+} + 2e^- \rightarrow Pt$	1.18
$Ir^{3+} + 3e^- \rightarrow Ir$	1.16
$Pd^{2+} + 2e^- \rightarrow Pd$	0.95
$Ag^{+} + e^- \rightarrow Ag$	0.80
$Rh^{3+} + 3e^- \rightarrow Rh$	0.76
$Ru^{3+} + 3e^- \rightarrow Ru$	0.45
$Cu^{2+} + 2e^- \rightarrow Cu$	0.34
$Ni^{2+} + 2e^- \rightarrow Ni$	–0.25
$Co^{2+} + 2e^- \rightarrow Co$	–0.28
$Fe^{2+} + 2e^- \rightarrow Fe$	–0.44

[a] Standard conditions: 25 °C and 1 atm. SHE: standard hydrogen electrode. E_o**:** standard redox potential in volts (V).

The general procedure for synthesizing NPs via this method begins with the selection of metal precursors. Metal-organic precursors, such as metal acetylacetonates, carbonyls, or oleates, are chosen based on the desired metals. For example, acetylacetonates ($M(acac)_x$) are chosen to decompose under moderate conditions [75]. The chemical nature and thermal stability of precursors determine the decomposition temperature and the final composition of the NPs.

These metal precursors are then dissolved in a high-boiling-point solvent along with surfactants. Surfactants play a crucial role in stabilizing the NPs and controlling their growth. Surfactants and stabilizers, such as oleic acid and oleylamine, can selectively bind to different crystal facets, influencing the shape and size of the NPs [26]. The solvent used in the process

also affects the solubility of the precursors and the kinetics of the decomposition reaction. High-boiling-point solvents provide a stable environment for high-temperature reactions.

The reaction mixture is subsequently heated to a temperature where the metal precursors decompose, typically in the range of 200-300 °C. The heating rate and the final temperature are carefully controlled to ensure uniform decomposition and NP formation. Reaction temperature and time play significant roles. Once the decomposition is complete, the reaction mixture is cooled to RT. The resulting NPs are then purified by centrifugation and washing with solvents such as ethanol or acetone to remove any unreacted precursors and surfactants.

Here, in the bimetallic Pt-Ni NPs system, we selected $Pt(acac)_2$ and $Ni(acac)_2$ as metal precursors and benzyl ether, oleylamine and oleic acid as organic solvents. $W(CO)_6$ was used as surfactant to control the shape of the NPs. After multiple trials, we found the optimized reaction condition is reaction temperature of 200 °C and reaction time of 35 min. Detailed procedure is described in section 4.2.1 in Chapter 4.

However, synthesizing monodisperse HEA NPs via colloidal chemistry is challenging due to the different reduction rates of metal precursors and the limited understanding of reaction intermediates. The Skrabalak group proposed a general approach to HEA NPs through an NP conversion pathway. In this method, two-phase core-shell NPs are synthesized using the colloidal chemistry method and then converted into single-phase HEA NPs by heat treatment [19]. Figure 2.1 illustrates the sequential process involved in forming HEA NPs. The procedure begins with the preparation of monodisperse bimetallic seeds, which serve as the foundation for subsequent reactions. Then, other metal precursors are

co-reduced in a heated solution. The resulting core-shell NPs are loaded onto a carbon support and annealed to form HEA NPs. Since it involves a more complicated system than bimetallic NPs, the synthesis principle is also more complex. Their approach to designing monodisperse core-shell NPs follows specific principles: (1) placing metal precursors with higher reduction potentials relative to other metals in the core of the core-shell NPs, (2) positioning metal precursors with significantly lower reduction potentials relative to other metals in the shell, and (3) using metals that impede alloy phase formation or exhibit poor wettability in the core of the core-shell NPs. This strategy for converting NPs into HEA offers an efficient method to create monodisperse alloy NPs spanning a wide range of compositions [19]. Through collaboration with Skrabalak group, quinary PdCuPtNiCo NPs with core-shell and HEA structures were obtained for further study.

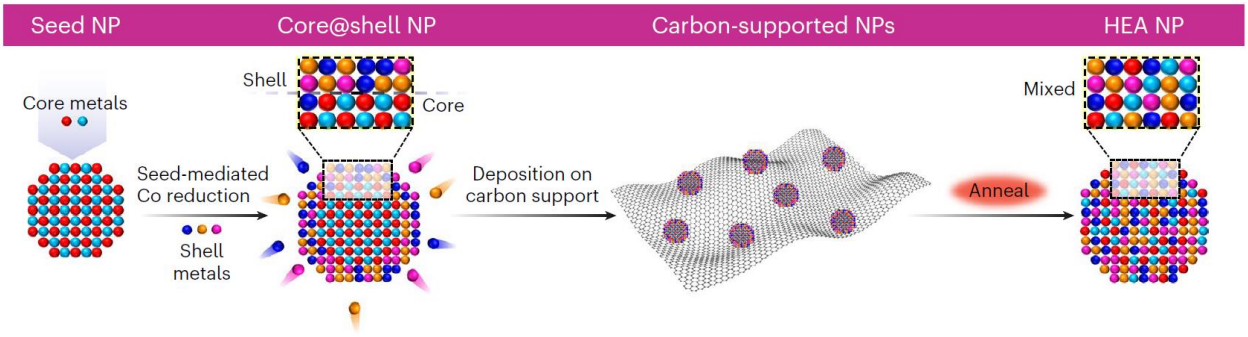


Figure 2.1 Illustration of the NP conversion process to synthesize HEA NPs [19]. Reproduced with permission. Copyright 2024, Springer Nature.

2.2 Characterization Methods

2.2.1 Conventional Transmission Electron Microscopy

TEM is an advanced technique for characterizing materials through imaging, diffraction, and spectroscopy with high resolution [76]. Figure 2.2 is a schematic diagram of

a TEM, where the emission source is located at the top of the column. The electron gun is powered by a high voltage source, usually ranging from 100 to 300 keV, and emits electrons into a vacuum. These electrons interact with atoms within the sample, altering their trajectory and causing 3D scattering. The extent of scattering angles is influenced by the density and thickness of the sample, resulting in varying brightness and contrast in the images produced. A TEM comprises multiple stages of lenses: the objective lens focuses the beam passing through the sample, the condenser lens forms the primary electron beam, and the projection lens enlarges the beam for observation on a phosphor screen. Then images are displayed on imaging devices such as fluorescent screens, films, or CCDs after magnification and focusing.

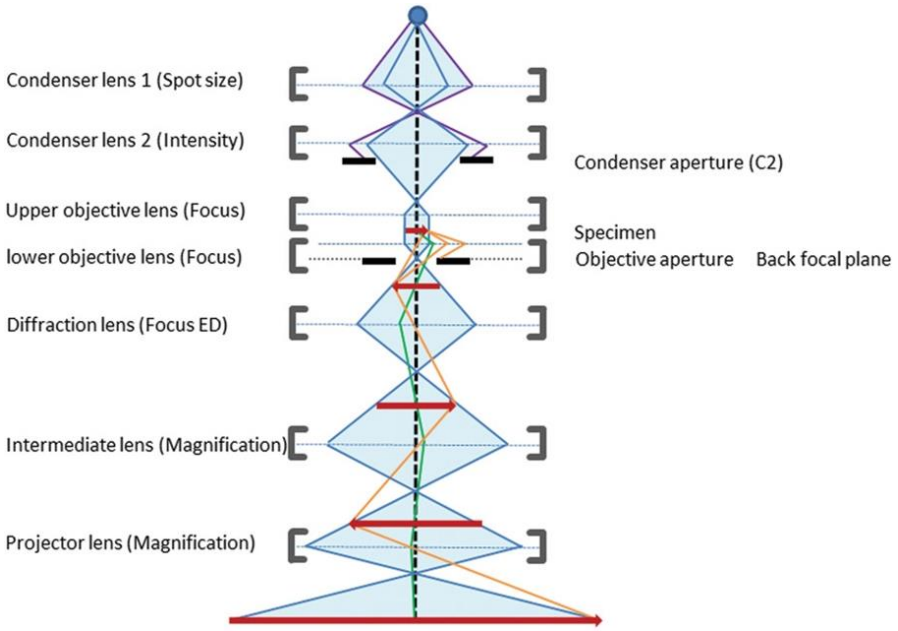


Figure 2.2 Schematic of a TEM. The electron beam is shown in blue. Lenses are indicated by gray brackets labeled with their names and respective microscope functions. Black bars represent apertures, and a red arrow denotes the specimen and its intermediate images. The

paths of scattered electrons are depicted in orange and green [77]. Reproduced with permission. Copyright 2020, WILEY-VCH.

Conventional TEM has four standard TEM modes, as shown in Figure 2.3. BF imaging refers to capturing images where the transmitted beam passes through the objective aperture. DF images, on the other hand, are obtained when the diffracted beam passes through the objective aperture. By changing the objective aperture to a selected area diffraction aperture, selected area electron diffraction SAED patterns can be generated to identify crystallography and phase information. HRTEM imaging is commonly utilized to visualize material structures at the atomic level, leveraging phase interference from multiple beams.

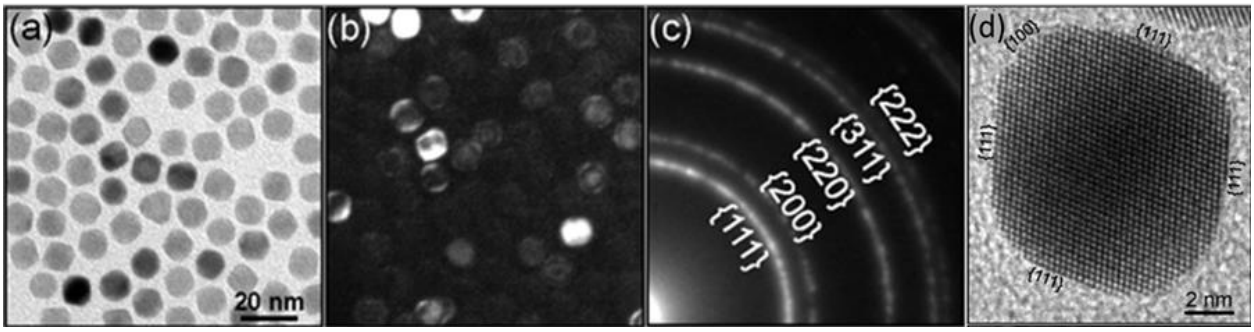


Figure 2.3 TEM images of Au seeds using different modes. (a) BF image. (b) DF image. (c) Corresponding SAED pattern. (d) HRTEM image [78]. Reproduced with permission. Copyright 2010, American Chemical Society.

2.2.2 Scanning Transmission Electron Microscopy

STEM represents an alternative mode in TEM characterization. Unlike TEM, STEM employs detectors instead of apertures, offering greater flexibility. By adjusting the camera length, the collection angle of the detector can be varied, as shown in Figure 2.4. Z-contrast,

a technique for high-resolution atomic and mass-thickness imaging, is also known as HAADF imaging.

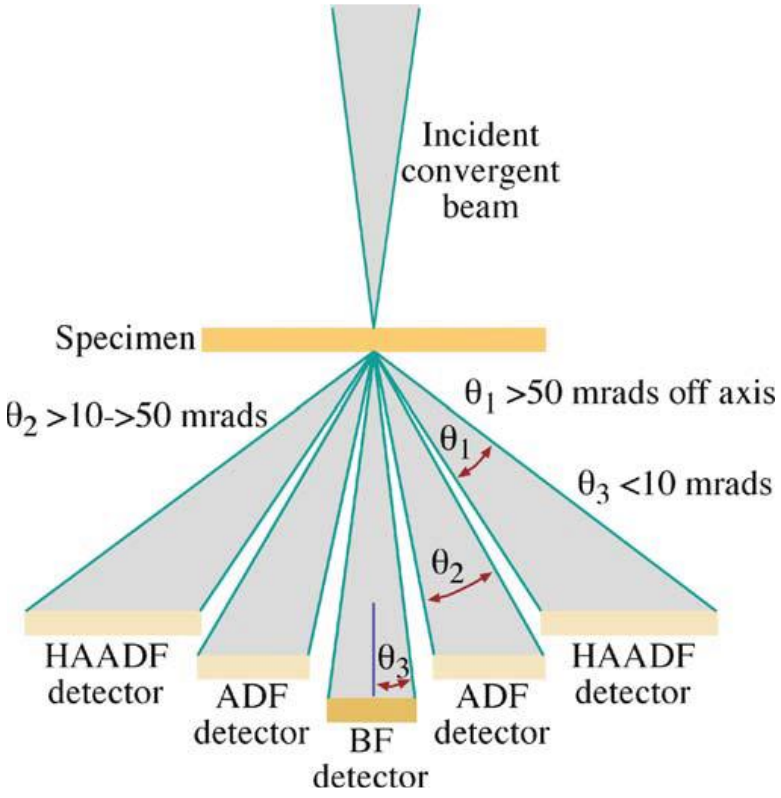


Figure 2.4 Schematic of the detectors in STEM. [79]. Reproduced with permission. Copyright 2009, Springer.

Analytical spectroscopy techniques such as EDS and EELS can identify information including chemical bonds, valence states, elemental compositions, electronic structures, and their spatial distributions when integrated with STEM. The significant advancements in aberration correctors and monochromators since the 1990s have facilitated exceptional spatial resolutions of approximately 0.4 Å and energy resolutions up to about 4.2 meV. These advancements provide unparalleled capabilities to resolve more information including the structure and chemistry of materials [80-82].

EDS is one of the strong techniques used to analyze the sample elemental composition. Its principle involves high-energy electromagnetic radiation that ejects core electrons from atoms. The resulting electron vacancies are filled by higher-energy electrons, releasing energy as they relax. This energy release is characteristic for each element, enabling identification of the elements present and their relative proportions in the sample.

EELS, on the other hand, analyzes the energy distribution of electrons passing through a specimen. These electrons may have undergone elastic scattering or inelastic collisions, which provide insights into the electronic structure, bonding, or valence states of the specimen. EELS complements EDS by offering more detailed information beyond elemental identification and is particularly effective for detecting light elements that are challenging to analyze with EDS.

2.2.3 In Situ Transmission Electron Microscopy

Advanced TEM-based techniques have been extensively employed to characterize a wide range of materials from conditions such as a specific reaction or process. This approach is known as "postmortem" or "ex situ" examination [83]. In contrast, to gain a deeper understanding of the intrinsic properties of materials, it is essential to directly observe their transformation during live reactions or processes, known as "in situ" characterization. In situ TEM involves applying one or more physical stimuli (such as heat, force, light, electrical bias, magnetic fields, electron beams, cooling, etc.) or chemically reactive environments (such as gases or liquids) within the TEM column. This approach mimics realistic operational conditions of the material and allows real-time observation of its structural, chemical, and functional changes.

In situ TEM has rapidly advanced over the past two decades, with significant efforts focused on developing instrumentation and conducting materials science research in dynamic environments [84-86]. The focus of interest comprises the study of materials undergoing transformation in chemical reactions or physical changes such as gas-phase, vacuum, and liquid-phase environments. In these studies, various stimuli may be applied solely or in combination with the samples using different types of in situ specimen holders (such as open cells and closed cells) or column settings (such as ETEM), as shown in Figure 2.5.

These sophisticated in situ TEM methodologies enable real-time imaging, diffraction, and spectroscopy to directly observe the structural and chemical changes occurring during dynamic processes at their operational conditions.

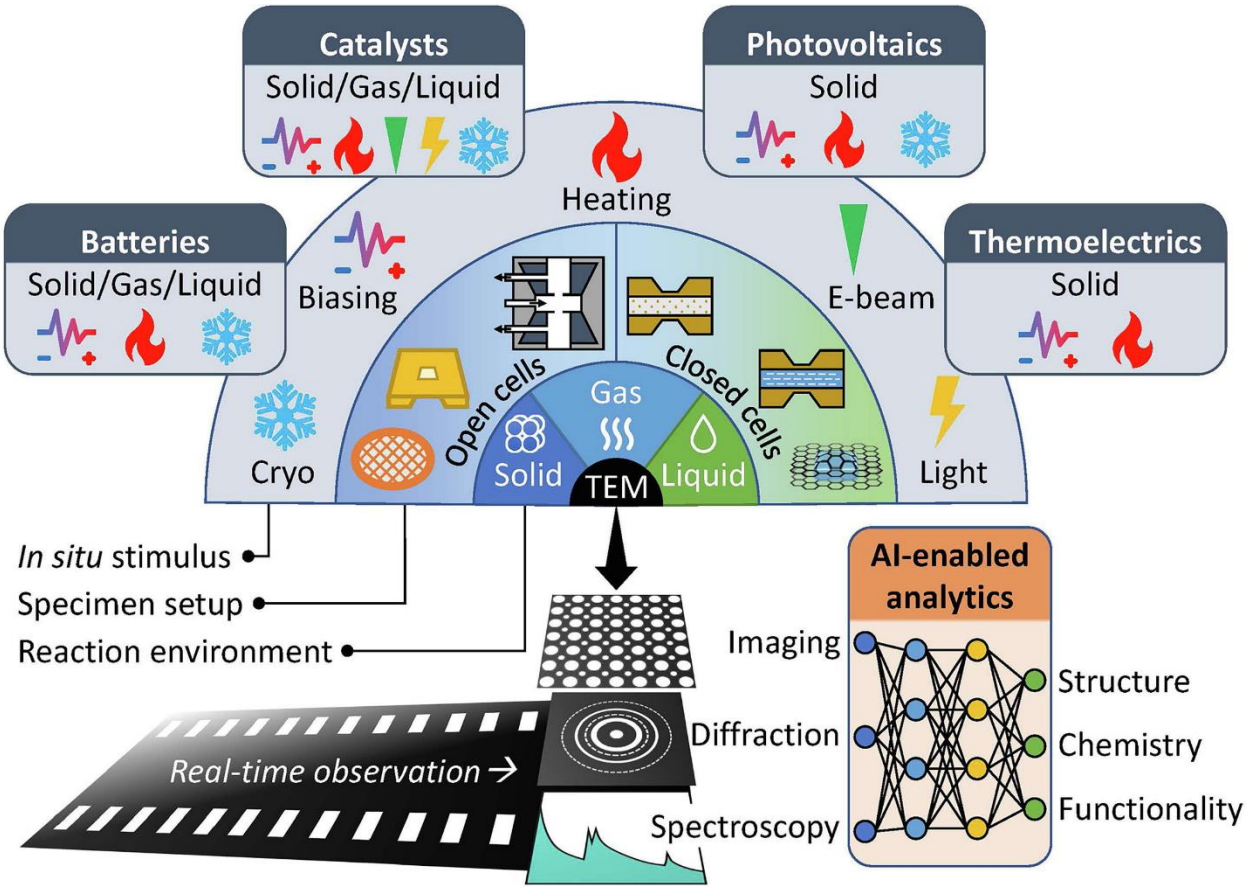


Figure 2.5 Schematic illustration of in situ TEM methodologies and AI-enabled data analytics for energy conversion and storage materials [87]. Reproduced with permission. Copyright 2022, Elsevier.

While traditional TEM postmortem characterization has been crucial in uncovering the effects of catalysts' static structures (such as crystal facets, defects, interfaces, etc.) on catalytic properties in as-synthesized and post-reaction states, understanding the dynamic evolution of the structure-property relationship under operational conditions and realistic environments is equally vital using in situ TEM. Depending on the type of catalysis—thermocatalysis, electrocatalysis, or photocatalysis—in situ TEM employs different stimuli

to observe the dynamic processes such as catalyst NPs crystal growth or the initiation of catalytic reactions across solid-solid, solid-liquid, and solid-gas phases.

Thermal stability is a critical concern in catalytic processes across academic research and industrial applications. Catalyst nanocrystals are subjected to thermal conditions to adjust compositions and surface structures or exposed to elevated temperatures during operation. Therefore, understanding the material transformation pathways and thermal stability at relevant temperatures is essential for designing catalysts effectively. In situ heating is a commonly used function in TEM, evolving through generations with different types of heating sample holders, as illustrated in Figure 2.6(A–C).

The first-generation heating holder is the furnace-type (Figure 2.6A), capable of heating the entire 3 mm TEM grid to approximately 1000 °C. However, it suffers from uneven temperature distribution and significant thermal drift on the sample. Moreover, its geometry causes strong X-ray shadowing, making it unsuitable for EDS analysis [88]. Figure 2.6(B) shows another type of bulk heater with the design of spiral-shaped tungsten wire, enabling the heating temperature up to ~1500 °C [89]. However, a shortcoming is that it limits the sample amount with nanostructured materials in contact with the surface of the wire, significantly reducing the visible area and the tilting range. In contrast, the latest heating holder utilizes the MEMS technique. This technique enables localized Joule heating using a nanopatterned metal heating element controlled by a four-probe feedback loop [90], as shown in Figure 2.6(C). The MEMS-based heating holder enables accurate control of local temperatures up to 1100–1300 °C, is suitable for nanostructured samples, and FIB samples, and provides larger tilting ranges and improved EDS collection capabilities. This technique

allows for rapid heating to the desired temperature, significantly reducing specimen drift compared to furnace-type holders. The low thermal mass of the MEMS heating element minimizes thermal expansion in the local area, enabling quick stabilization of drift within minutes, which greatly facilitates in situ observations.

MEMS heating chips are typically calibrated by the manufacturer using temperature-dependent resistance measurements. However, the actual temperature of the local observation area may differ from the temperature controller readout due to electron-beam-induced heating effects. For instance, the high-energy electron beam in TEM can serve as a local heat source to initiate nanocrystal transformations. However, directly measuring the exact temperature in this scenario is challenging [91]. This effect becomes more pronounced when the heating holder is used in non-vacuum environments with varying gas species and pressures. To mitigate the influence of these factors, it is crucial to accurately verify temperature calibration under real experimental conditions. This verification can be achieved using thermometric materials with known characteristic transition temperatures (such as melting points, crystal phase transitions, magnetic transitions, thermal expansion of lattice, or chemical reactions). Additionally, spectroscopic methods like EELS or diffraction techniques can measure plasmon/phonon excitations to further validate temperature conditions [92].

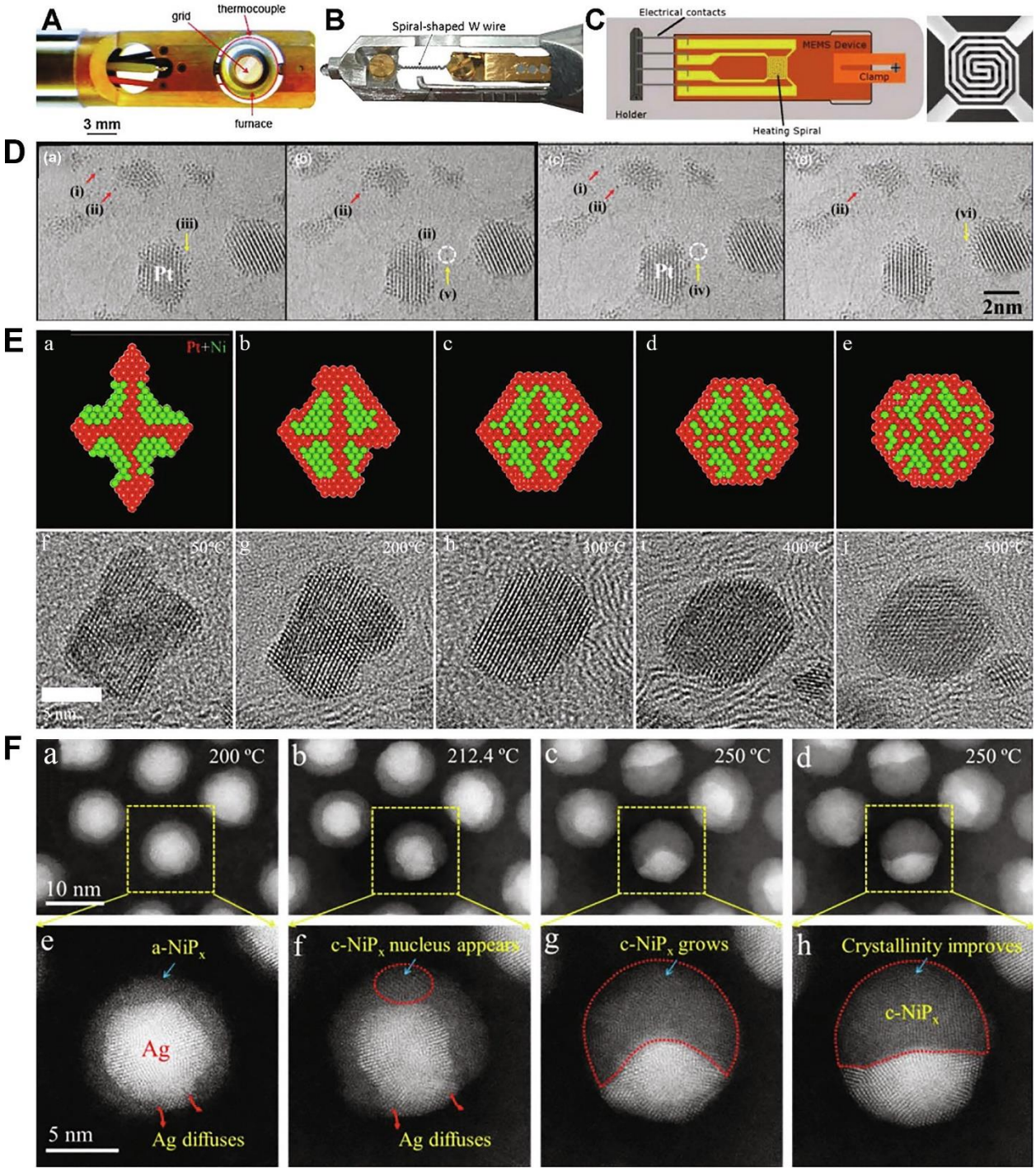


Figure 2.6 In situ heating setup and applications for nanocrystal evolutions at elevated temperatures. (A) The furnace-type bulk heating holder [88]. (B) The spiral-shaped tungsten wire heating holder [89]. (C) The MEMS-based heating holder [90]. (D) In situ

HRTEM images showing atom migration and structural evolution of Pt NPs [66]. (E) In situ HRTEM images of $PtNi_{1.5}$ octahedral NPs and the corresponding schematics showing the Pt (red) and Ni (green) redistribution during heating [71]. (F) In situ HAADF-STEM images showing the structural transformation of Ag-NiP_x nanocrystals from core-shell to Janus structure from 200 to 250 °C [22, 87]. Reproduced with permission. Copyright 2022, Elsevier.

In situ heating experiments have been conducted inside TEM for various mono- and multimetallic nanocatalyst systems using different types of heating holders. Yoshida et al. utilized in situ AC-TEM to investigate the dynamic behavior of Pt nanocrystals under the influence of a 300 kV electron beam [66]. Figure 2.6(D) presents selected images extracted from the original in situ TEM video, illustrating how the electron beam enhances the mobility of Pt atoms, allowing them to migrate on the carbon film. Consequently, Pt atoms can either remain in place or move to adjacent Pt NPs. This interparticle transfer of surface atoms between similarly sized NPs leads to the shrinkage of one particle and the growth of another, known as Ostwald ripening. These observations provide insights into the mechanism of Ostwald ripening at the single-atom level, suggesting that besides single atoms, bi-atoms and clusters may also collectively transfer during this process [66]. In addition, the dynamic behaviors including NP migration, coalescence, and sintering have also been reported in monometallic Au, Ag, and Pt nanocrystals [93-95].

Understanding the transformation pathways of complex structures in bimetallic heterogeneous nanocrystals, which can change under elevated temperatures, is crucial for

assessing their catalytic activity and stability. In situ heating experiments are essential for gaining insights into these pathways.

Pt-Ni nanocrystals are a popular bimetallic system renowned for their exceptional electrocatalytic activity in ORR [96]. Gocyla et al. performed in situ heating TEM study of $PtNi_{1.5}$ octahedral nanocrystals [71]. Figure 2.6(E) exhibits a sequence of HRTEM images showing the evolution of a Pt-Ni NP as it is heated from 50 to 500 °C. Initially, the pristine Ni-rich Pt-Ni NP has a concave octahedral shape. As the temperature increases, changes in morphology occur: at 200 °C, Pt diffuses from the edges, forming partially filled {111} facets. Subsequent Pt diffusion leads to the formation of a truncated octahedron shape at 300 °C, followed by a cuboctahedron shape at 400 °C, and finally a spherical particle at 500 °C. Throughout the process, the catalyst maintains a balance between the thickness of the Pt shell and the enrichment of Ni subsurface, achieving an optimized ratio between {111} and {100} facets. These facets are crucial for ensuring long-term stability and high catalytic performance [71]. Similar studies were also performed in sandwich-type Pt-Ni octahedral NPs [97] and Pt-rich Pt-Ni octahedral NPs [72], further demonstrating the impact of composition redistribution on catalytic performance. Other bimetallic nanocrystals involving Pt and TM like Co, Cu, Fe, etc., are also promising electrocatalysts for ORR. Xiong et al. employed in situ atomic-scale STEM to directly observe the phase transitions and morphological changes in both fully and partially ordered Pt_3Co NPs. They discovered that the optimally ordered structure exhibited significantly enhanced durability compared to the disordered counterpart [98]. Gatalo et al. studied the heat treatment of $PtCu_3$ NPs and identified the mechanism of Cu enrichment at elevated temperatures. They observed that the migration of Cu single atoms on the carbon support led to morphology reshaping and

crystal lattice ordering when heated to 500 °C [99]. Yao et al. conducted in situ heating study on carbon-supported low-Pt alloy catalysts, including $PtFe_3$, $PtCo_3$, and $PtNi_3$. Their findings showed that surface enrichment of TM elements could lead to faster particle coalescence and increased particle mobility on the carbon support. This research provides valuable insights for preparing thermally stable Pt-alloy catalysts with minimal sintering [67].

In addition to the core-shell and order-disorder transformations commonly observed in the previously mentioned studies, other transformation pathways can also occur in heterogeneous catalytic systems during heating. Huang et al. investigated the structural transformation of Ag-NiP_x core-shell nanocrystals under thermal treatment using in situ AC-STEM combined with elemental analysis [22]. It was found that the core-shell structure of Ag-NiP_x nanocrystals remained stable below 200 °C. As the temperature increased, Ag began to diffuse from the core to the surface, while NiP_x simultaneously grew on the opposite side of the Ag, forming a Janus structure with a sharp interface, as shown in the HAADF-STEM images in Figure 2.6(F). This newly formed Janus structure remained relatively stable between 250 and 450 °C. At 500 °C, Ag fully sublimated, leaving behind individual $Ni_{12}P_5$ nanocrystals. This core-shell to Janus transformation was driven by the minimization of surface energy, offering valuable insights into the structural engineering of multicomponent nanocrystals for catalytic applications [22]. In addition, in situ heating TEM has been extensively utilized to investigate the growth mechanisms of other heterogeneous systems, such as TM carbide catalysts Mo_2C and W_2C [100, 101].

CHAPTER 3 Machine Learning for Images Analysis

Portion of this chapter is a reprint of the material as it appears in "In situ transmission electron microscopy and artificial intelligence enabled data analytics for energy materials" [Zheng, H.; Lu, X.; He, K., Journal of Energy Chemistry 2022, 68, 454-493], used with permission from Elsevier. Portion of this chapter is a reprint of the material as it appears in "Machine Learning Enhanced Image Segmentation for High-Fidelity STEM Data Analysis" [Lu, X.; He, K., Microscopy and Microanalysis 2023, 29 (S1), 1895-1896], used with permission from Oxford University Press.

3.1 Background

3.1.1 AI-enabled Microscopy Data Analytics and Applications for In Situ TEM

AI simulates human intelligence in machines, enabling them cognitive and problem-solving abilities like humans [102]. ML, a branch of AI, uses computer algorithms to learn from data and make decisions autonomously. This has advanced to DL, where artificial neural networks allow the learning process to occur without human intervention [103-105]. In situ TEM is a data-intensive method that produces numerous graphic and spectral datasets over time, position, or other parameters. Traditional manual processing of these datasets is tedious and easy to make errors. Thus, AI approaches are preferred for autonomous and objective data analysis in in situ TEM characterization. Recently, ML-enhanced methods have been involved in microscopy imaging and spectroscopy data analysis [106-109]. Therefore, ML is increasingly utilized in analyzing microscopy data from biomedical imaging and physical studies. ML aims to enable computers to perform specific tasks automatically without explicit programming. There are two main approaches:

supervised ML, which uses labeled data for accurate prediction, and unsupervised ML, which analyzes unlabeled data to uncover hidden patterns. DL employs artificial neural networks to mimic human brain data processing. DL leverages the depth of neural network layers to create more effective models with minimal human intervention, requiring more powerful hardware and computing resources due to its complexity.

The advancement of ML and DL algorithms has significantly improved AI-enabled data analytics in electron microscopy. TEM-based methodologies produce various data types, including 2D TEM/STEM images, 3D electron tomography images, diffraction patterns and EELS spectra. These data types can be integrated into high-dimensional datasets in energy-filtered TEM, STEM-EELS spectrum imaging, 4D-STEM diffractive imaging, and time-sequenced in situ TEM, which are ideal for ML/DL methods. ML-based approaches for TEM data analysis have seen rapid development in recent years.

3.1.2 Machine Learning for TEM Image Processing

In situ TEM imaging typically produces datasets of images over time, capturing a specific sample in a dynamic process. There is a need to process and analyze these image data effectively. AI has greatly enhanced and automated image processing through ML, addressing routine tasks such as image recognition, segmentation, localization, classification, restoration, representation, and interpretation. Utilizing available algorithms and tools, AI-enabled image processing has been widely applied to various aspects of TEM analysis [106-109].

Image segmentation is a common and crucial task in TEM data analysis, requiring both accuracy and high speed to handle the large volumes of images produced by in situ TEM

experiments. Beyond pixel-wise segmentation of individual atom columns, DL also provides effective solutions to the semantic segmentation of TEM and STEM images at the small scale of microstructures and single particles [110-112]. Recently, Stach and colleagues conducted a case study on the semantic segmentation of NPs using CNN-based DL models [110]. They focused on a model system of Au NP catalysts that change in size and morphology during the Ostwald ripening process, as observed by in situ ETEM. They used the U-Net CNN architecture to segment NPs in HRTEM images, demonstrating its robustness in consistently identifying NPs of varying sizes, despite minor variations in edge detection, as shown in Figure 3.1(A). By systematically comparing CNN learning parameters, the study found that regularization through batch normalization is more effective than increasing the depth or complexity of the CNN, offering valuable guidelines to more generalizable segmentation tasks.

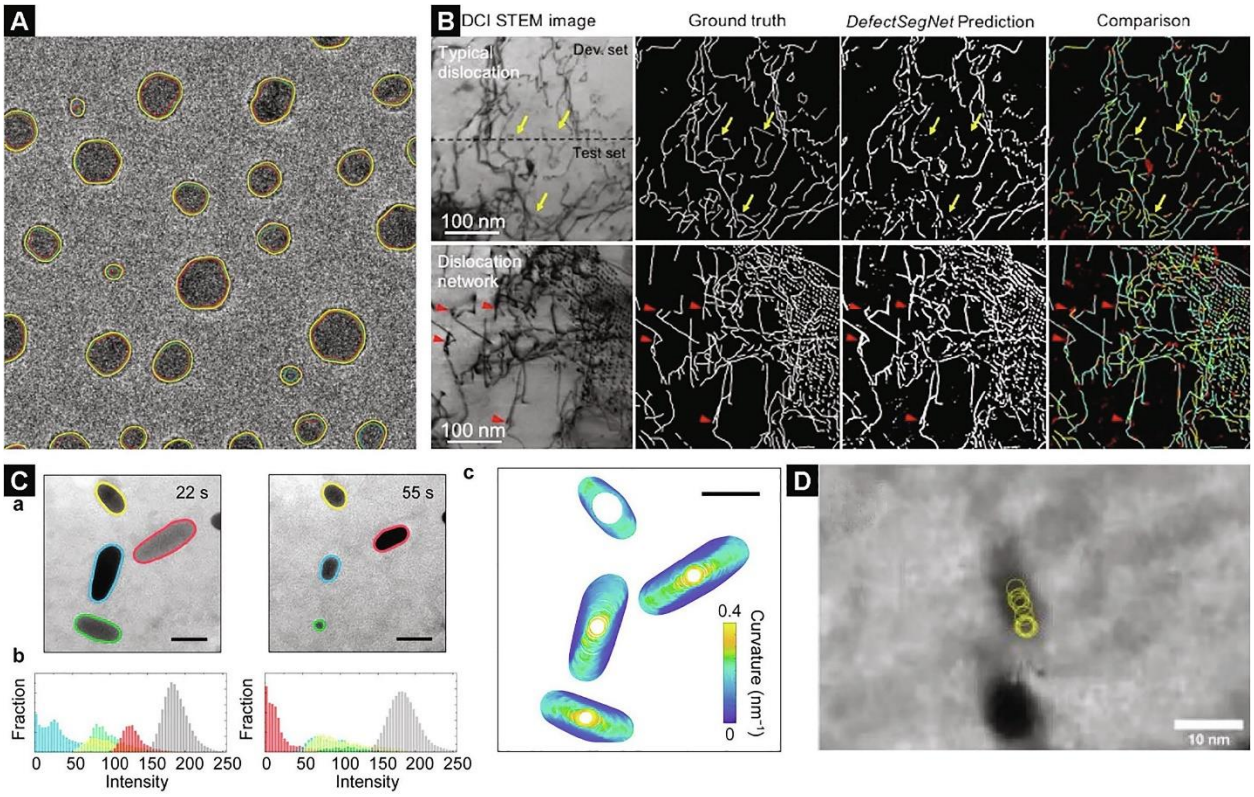


Figure 3.1 ML approaches for identification and tracking morphologies and microstructures in TEM images. (A) DL for image segmentation of Au NPs by U-Net frameworks with robust edge detection [110]. (B) DL for sematic microstructure detection by DefectSegNet model [112]. (C) U-Net based DL for segmentation of Au NP during in situ LCTEM [113]. (D) YOLO model-based DL for detecting the dynamic trajectory of a single defect in FeCrAl alloys upon in situ ion irradiation [87, 114]. Reproduced with permission. Copyright 2022, Elsevier.

Chen and colleagues applied the U-Net DL model to an in situ LCTEM study on the motion, chemical reaction, and self-assembly of Au NPs in solution environments [113]. The U-Net model's accurate segmentation of particle boundaries enabled the detection of the shape evolution trajectory of Au NPs during an etching process over time, as shown in Figure 3.1(C). This etching behavior was found to be highly dependent on curvature. Additionally,

other ML methods have also been used to study dynamic processes during in situ TEM experiments [115, 116]. These studies have demonstrated the feasibility and readiness of applying ML techniques to general in situ TEM experiments in liquid and gas environments.

Meanwhile, Zhu and colleagues conducted a case study on the semantic segmentation of microstructures in diffraction contrast imaging (DCI) STEM images of steels using the DefectSegNet CNN architecture [112]. The shape irregularity and distribution inhomogeneity of nonperiodic crystallographic defects pose significant challenges for the semantic segmentation of microstructures in practical TEM images. Using supervised DL via the DefectSegNet framework, three prototypic defect microstructures—dislocations, precipitates, and voids—were identified and segmented with high pixel-wise accuracy. Figure 3.1(B) illustrates an example of dislocation detection in the steel matrix, despite the complex background contrast. This study highlights the effectiveness of DL-enhanced image segmentation for complex TEM images with significant contrast variations.

Morgan et al. have conducted similar work to detect dislocation loops in FeCrAl alloys using a CNN-based DL approach [117]. Similarly, they employed the YOLO model-based deep learning technique to detect and track the dynamic motion of a single defect in FeCrAl alloys during in situ ion irradiation experiments [114]. Figure 3.1(D) shows the motion trajectory of the defect throughout its lifespan. This analysis was applied to in situ TEM videos to automatically detect the trajectories of all relevant defects. Statistical analysis of the trajectory data subsequently revealed the relationship between the effective diffusion coefficient and the median defect size. These findings provide critical benchmarks for

improving the accuracy of detecting and tracking complex features in in situ TEM experiments.

3.2 Methods

3.2.1 Image Segmentation

There are two primary ML paradigms: supervised and unsupervised learning. In supervised learning, the availability of ground truth labels for the training data allows the optimization of model parameters to known outcomes. This approach is commonly utilized in classification or regression tasks where unique labels are available or the value of interest can be observed. For image processing applications, supervised learning is widely used for tasks such as image classification, object detection, and semantic segmentation [118]. For instance, in image classification, a model is trained to assign an image to one of several predefined categories, such as identifying different species of animals in photographs. In object detection, the model not only classifies objects within an image but also identifies their locations by drawing bounding boxes around them. Semantic segmentation goes a step further by classifying each pixel in the image, allowing for detailed scene understanding. The success of these tasks depends on large, well-annotated datasets where each image is labeled with the correct category or segmentation mask.

Conversely, unsupervised learning involves reducing the features of the data to a simplified form, enabling the grouping or clustering of training examples based on their similarities. In the context of image processing, unsupervised learning is employed for tasks such as clustering, dimensionality reduction, and anomaly detection [119]. Clustering algorithms, like k-means or hierarchical clustering, group images based on visual similarities

without requiring labeled data [120]. For example, GAN and autoencoders have revolutionized image processing. GAN, which consists of a generator and a discriminator network, can generate realistic images from random noise, finding applications in areas such as image synthesis and data augmentation [121]. Autoencoders, which learn efficient coding of input data, can be used for image denoising, compression, and unsupervised feature learning [122].

The critical information in images is frequently embedded in the spatial relationships between objects. Therefore, encoding image data to preserve feature arrangements is essential. This is effectively achieved through the application of convolutional filters, which process image regions using a sliding window approach. By sequentially processing the information captured by these convolutional windows through multiple layers, and non-linear transformations, a CNN is constructed [110]. CNNs are among the most prevalent machine learning methodologies applied to image processing tasks. Convolutional filters apply to different areas of an image, allowing the spatial information to be encoded and utilized to classify individual pixels. In supervised learning, ground truth images where each pixel is assigned a specific class, are available for each training image. CNN aims to replicate this classification accurately, assigning the correct label to each pixel. In contrast, for unsupervised learning, the same CNN architecture can be employed to reproduce the input image rather than matching it to a known ground truth, which is often unavailable. In this scenario, the number of tunable parameters is significantly constrained, preventing the CNN from fully reproducing the input image. Instead, the network outputs a simplified version of the image, which can be easily segmented with minimal additional processing.

Given that the creation of labeled training datasets is frequently challenging and time-consuming, unsupervised learning offers significant advantages. Accordingly, we chose to use the unsupervised segmentation of TEM images. This approach leverages the power of CNNs to achieve efficient and effective image segmentation without the necessity for extensive labeled datasets.

Based on an open tutorial developed by Eric Stach group at University of Pennsylvania, we modified the workflow leveraging an autoencoder for image processing with several key steps to ensure accurate and efficient analysis. First, input images are fed into the system, serving as the raw data for training and analysis. These images are then processed using a neural network, specifically an autoencoder, which consists of an encoder to compress the image data into a lower-dimensional representation and a decoder to reconstruct the images from this compact form. As the network trains, it iteratively adjusts its parameters across multiple epochs. The performance of the network is monitored throughout the training process, and the epoch that yields the best reconstruction accuracy is selected. Once the best epoch is determined, the network processes the input images, generating reconstructed versions. Subsequently, statistical information is extracted from these processed images, which may include metrics such as reconstruction error, feature distributions, or other relevant statistical properties. Finally, the extracted data is plotted to visualize the results, allowing for verification of the accuracy and efficacy of the autoencoder. This visualization step is crucial for interpreting the performance of the network and ensuring that the processed images meet the desired quality and analytical standards.

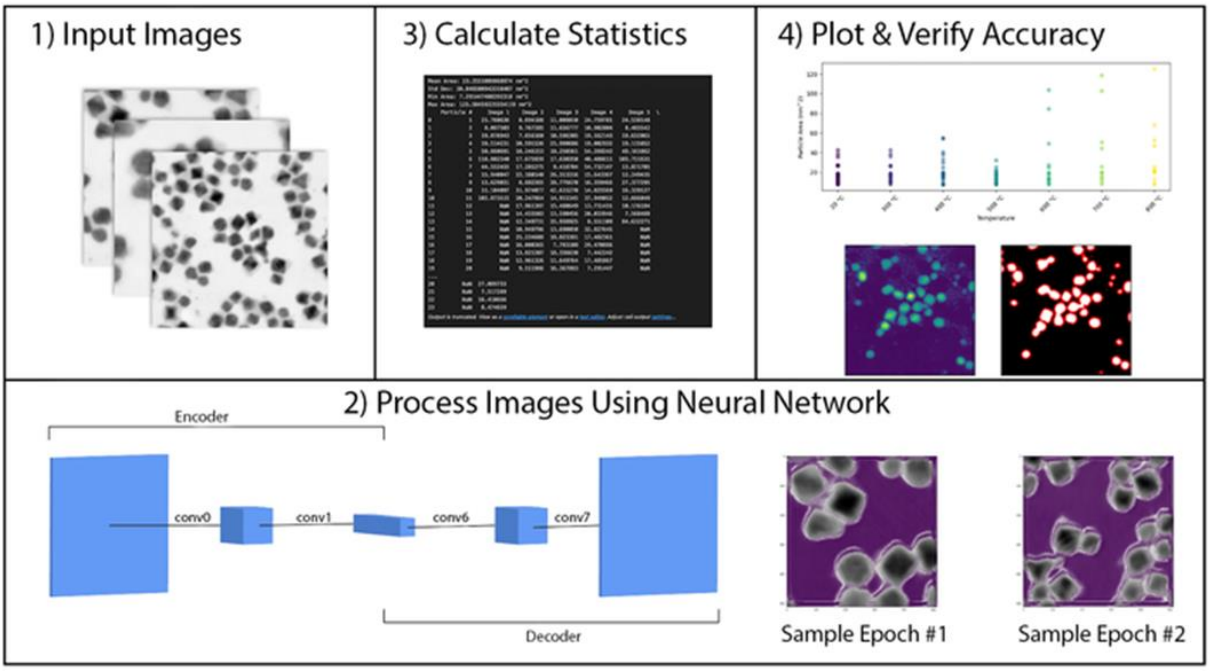


Figure 3.2 Modified workflow making use of the autoencoder.

There are four processing steps of the input images as shown in Figure 3.3. In the initial processing step, images are cropped to remove black borders caused by drift during the experiment. Drift, primarily induced by high temperatures, can also result from vibrations in the room or microscope. Proper drift correction is crucial as it ensures that particles can be accurately tracked, enabling meaningful analysis of the datasets. Drift is a consistent motion across a series of images, indicating that the entire image, and consequently all the particles within, move in a uniform direction. Discontinuities in the drift are corrected using cross-correlation techniques, ensuring smooth and continuous tracking of particles throughout the image sequence.

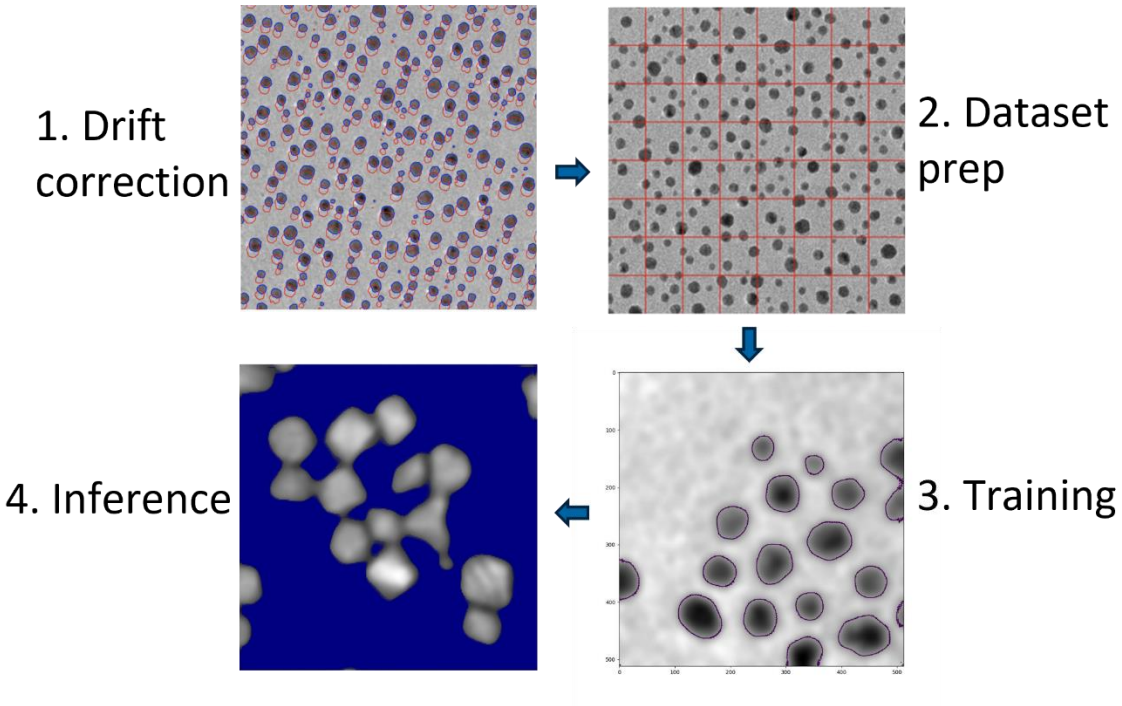


Figure 3.3 Processing steps of the input images.

In the second step, images are prepared for the machine learning model using data augmentation techniques, including cropping and rotation, to enhance the diversity of training examples. This augmentation process effectively increases the number of unique images available for training, thereby conserving resources by reducing the need for a large number of raw images. Each image is divided into smaller segments, each serving as a unique example in the training set. It is essential to maintain the similarity of these sub-images so that they closely resemble the larger image, ensuring the model is not biased by artifacts introduced during data augmentation.

The third processing step involves training the machine learning model. Raw training images from the previous step are fed into the model, which iteratively adjusts its parameters to produce outputs that closely approximate the ground truth. During training,

images are processed in batches, and the model's weights are adjusted based on the average performance across these batches. This batch processing approach optimizes the model's ability to generalize from the training data to new, unseen images.

In the final step, the trained machine learning model is applied to the remaining images. The selected weights from the training phase are used for image segmentation. The segmented output images enable further analysis, such as quantifying the number of particles per image, measuring particle sizes, and examining interactions between particles to determine certain mechanisms. This inference step translates the model's learned knowledge into actionable insights, facilitating detailed and accurate analysis of the experimental data.

3.2.2 Synthetic Data Generation

The extraction of scientific information from EM images has increasingly relied on the application of CNNs due to their exceptional ability to identify patterns in spatial data [110]. However, the efficacy of these networks is dependent on the availability of extensive and accurately labeled training datasets. The labor-intensive process of manual data labeling often impedes the acquisition of sufficiently large datasets, which are crucial for both supervised and unsupervised learning. To mitigate this challenge, datasets are frequently augmented using GANs, although these also require substantial amounts of training data [123].

In response to this issue, we incorporated an approach that involves procedural data generation using known crystallographic properties of material facets, specifically the {111}, {110}, and {100} planes. This method allows for the creation of "pseudo particles" that not

only facilitate the generation of synthetic EM images but also enable the extraction of scientific information such as cross-sectional areas and center of mass positions. This data can be utilized for both supervised training and augmentation of training sets for unsupervised learning. By employing procedurally generated data, the dependency on large quantities of real training data is significantly reduced, enhancing the accuracy of CNN-based EM image processing. Additionally, these synthetic datasets can serve as ground-truth training data for supervised learning algorithms.

The implementation of procedural data generation is executed using Python's NumPy and Matplotlib libraries. The process begins with the modeling of a NP as a 3D grid. Users can specify the distances to the {111}, {110}, and {100} facets on a scale from 0 to 1, where 1 represents no truncation and 0 denotes maximum truncation. The NP is subsequently represented as an assembly of its terminating facets. To generate synthetic data, these 3D objects are projected onto the XY plane, with their density along the Z-axis used to create an intensity map. An example using {111} truncations is shown in Figure 3.4a. To simulate real-world conditions more accurately, the generated particles are subjected to random rotations and positioned at various locations within a single image. The final synthetic image is then produced by adding noise and blurs to mimic the imperfections commonly observed in actual EM images. Figure 3.4b demonstrates an example after random rotation.

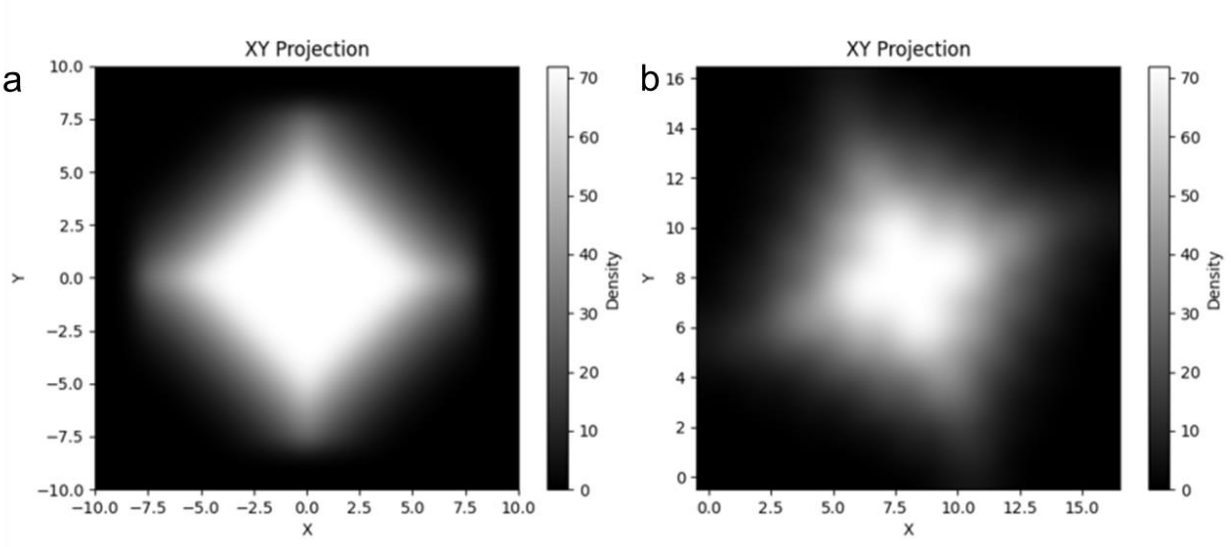


Figure 3.4 Symmetric truncated octahedral using {111} facets with a specified distance of 0.8. (a) Projection on XY plane. (b) XY projection after random rotation.By generating synthetic NPs and creating ground-truth training data, this approach provides a robust foundation for training CNNs in EM image analysis. The synthetic data generation not only enhances the volume and diversity of the training datasets but also ensures that the models trained using these datasets are capable of accurately processing and analyzing real EM images.

3.3 Results and Discussion

3.3.1 In Situ Images Analysis

We examined the application of ML image segmentation to retrieve useful information, such as to quantify the number and areas of bimetallic Pt-Ni NPs in in situ HAADF-STEM images taken at different temperatures. The goal is to evaluate the effectiveness of an ML-enhanced segmentation approach and provide accurate and reliable measurements of NPs properties under varying thermal conditions. Figure 3.5a shows the original HAADF-STEM image of Pt-Ni NP clusters acquired at multiple temperatures at

elevated thermal conditions during real-time in situ heating experiments. The ML image segmentation model was then applied to these images. The segmentation results were used to count the number of NPs and measure their projected areas at each temperature. The ML-enhanced segmentation successfully identified and outlined NPs across all temperature conditions, as shown in Figure 3.5b. The number of NPs and their respective areas were extracted from the segmented images and summarized in Table 3.1. Additional limits were added to get rid of the smaller particles and the bigger ones, and the contour shows the counted particles. At RT, the model identified 32 NPs per image with a total projected area of 700 nm^2. Due to the contrast difference especially reflected on the background clusters, there is a slight change at 300 and 400 °C. As the temperature increased to 500 °C, the average number of NPs decreased to 27, suggesting particle coalescence. At 700 and 800 °C, the total area of identified NPs increased, due to the carbon contamination identifying as NP on the upper right side of the images.

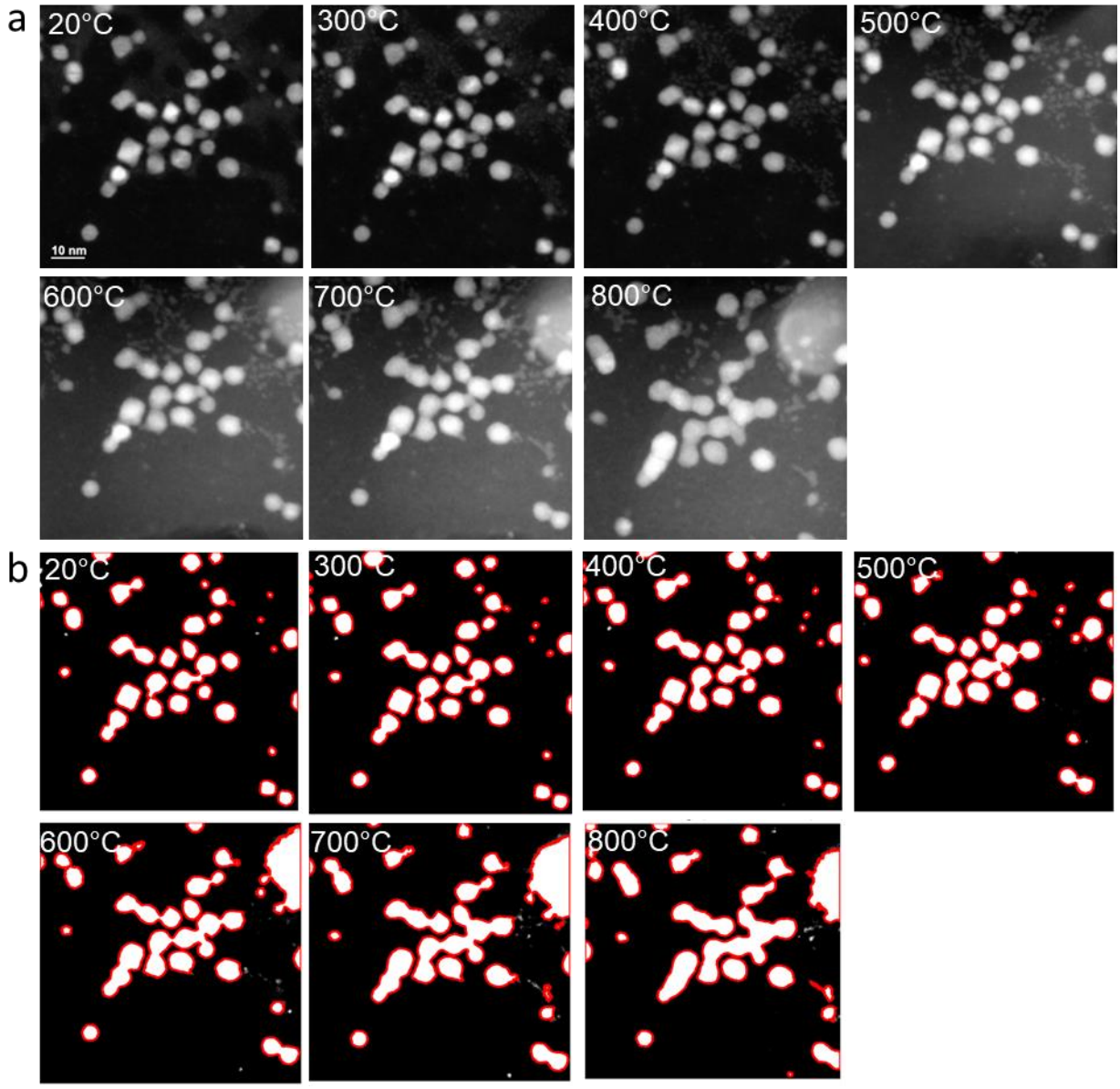


Figure 3.5 (a) Original in situ heating HAADF-STEM images of Pt-Ni NPs, and (b) contoured images using ML segmentation.

Table 3.1 Measurement of number and projected area of NPs from in situ STEM images.

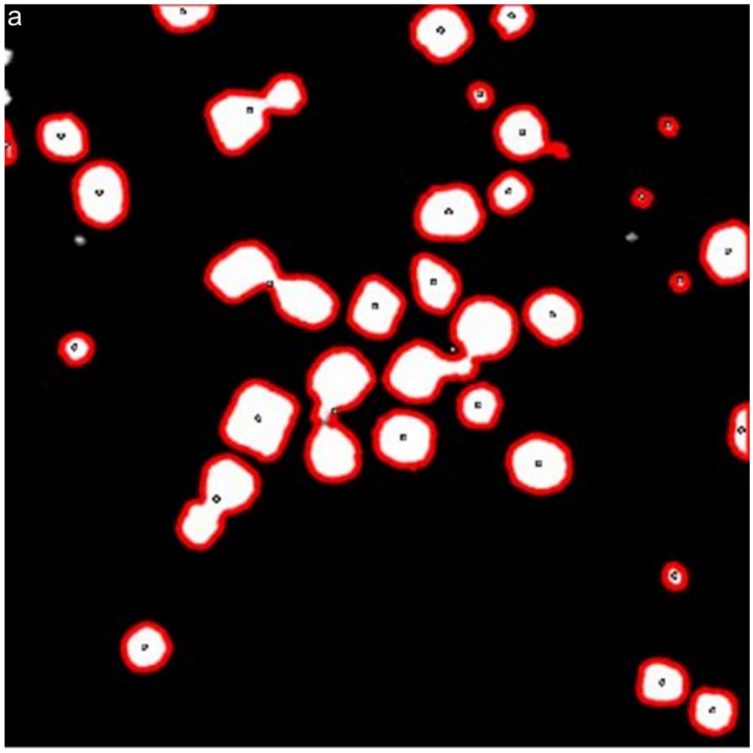
Temperature/°C	Number of NPs	Total projected area /nm^2
20	32	700
300	35	721
400	35	740
500	27	775
600	20	917
700	20	1013
800	22	1008

The results indicate a clear trend of decreasing NP count and increasing average area with rising temperature. This observation aligns with the expected behavior of coalescence and growth under thermal conditions. The ML model's ability to accurately segment and measure these changes highlights its effectiveness in capturing dynamic transformations. Compared to traditional methods, the ML-enhanced segmentation approach offers significant advantages. The ML model processes images much faster than manual segmentation, enabling high-throughput analysis. The automated segmentation reduces human error and ensures consistent measurements across a large dataset. The trained model can be applied to new datasets with minimal adjustments, making it highly scalable for different experimental conditions.

Additional data points, specifically the center of mass locations of each NP within the images are also incorporated. Figure 3.6a illustrates the labeled center of mass location in a contoured image. This figure shows how the center of mass is identified and marked within the NPs, providing a visual representation of each NP's geometric center. The x and y coordinates of the center of mass for each NP were labeled in Figure 3.6b, providing a precise method to track the movement and interactions of the NPs during thermal treatments. Their

movement, coalescence, or separation could be monitored throughout the process. Here, we selected a small area with 3 NPs and measured their pairwise distances of the center of mass, as shown in Figure 3.7. From RT to 500 °C, the ML model can identify all 3 NPs with the decreasing trend of distances, indicating the interparticle mass transfer. From 600 to 800 °C, NP 2 and 3 merged and they were identified as a single NP. Therefore, we put the distances between them as 0 and the other two pairwise distances are the same. At highly elevated temperatures, NP 1 started merging with NP 2 and 3, showing the reduced distances between them. By labeling the center of mass location and measuring the pairwise distances, the coalescence behavior can be quantified and provide more information to understand the mechanism.

a



b

No.	x	y
1	1947	1947
2	1807	1870
3	388	1772
4	1842	1577
5	586	1367
6	1470	1269
7	1100	1199
8	2025	1178
9	1305	1109
10	701	1146
11	911	1126
12	197	951
13	1234	957
14	1506	862
15	1020	840
16	1857	768
17	1182	773
18	732	776
19	1988	687
20	1752	537
21	1223	580
22	1388	524
23	265	526
24	10	395
25	1824	341
26	160	371
27	1424	361
28	1307	256
29	677	303
30	1201	82
31	1395	42
32	493	32

Figure 3.6 (a) Labeled center of mass location in the example contoured image. (b) x and y coordinates of the center of mass.

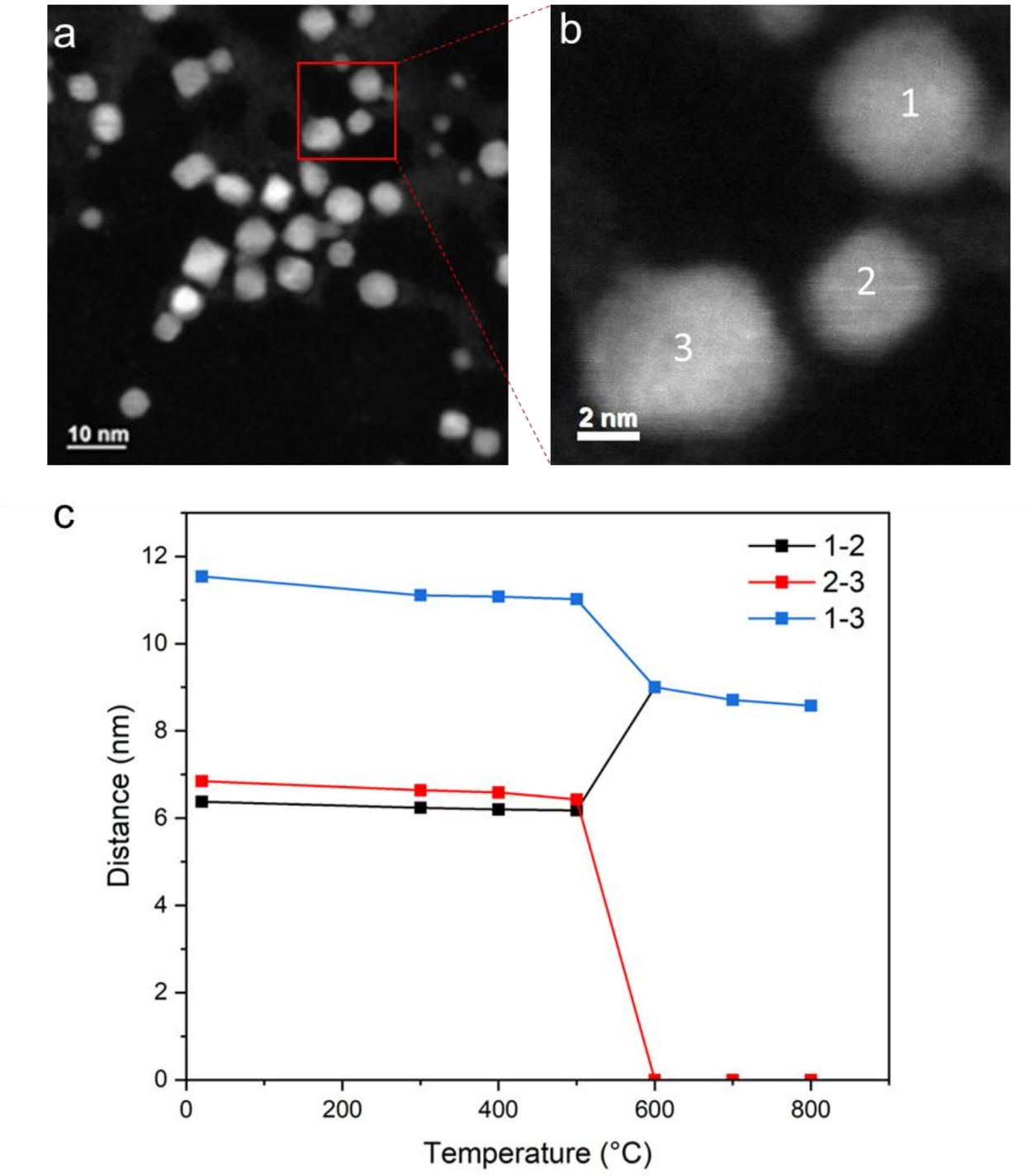


Figure 3.7 (a) Original HAADF-STEM image. (b) Cropped image from (a). (c) Plot of the center of mass distances as a function of temperature.

3.3.2 Data Analysis Precision and Statistics

With the above analysis, we further focused on the precision and statistics of data analysis. It is noted that the statistical analysis of segmented NPs across different magnifications offers further insights. At lower magnifications, a larger field-of-view captures more NPs in a single image, providing a greater number of data points for statistical analysis. This can be advantageous for understanding the distribution and overall trends within the sample. However, the reduced pixel resolution at these magnifications compromises the precision of individual NP segmentation, leading to lower accuracy.

Conversely, higher magnifications provide a more detailed view of fewer NPs, allowing for highly accurate segmentation and precise characterization of each NP. This high-resolution data is essential for in-depth studies where accurate measurements of size, shape, and edge properties are critical. Although fewer NPs are analyzed at high magnifications, the high accuracy of segmentation ensures that the data obtained has higher quality, contributing to more reliable conclusions about the material properties.

Therefore, we focused on how to compromise the two factors and examined the effectiveness of image segmentation for HAADF-STEM images using both traditional global thresholding methods and ML-enhanced segmentation approach on different magnifications. We specifically employed the U-Net CNN architecture to evaluate the accuracy and efficiency of ML algorithms in identifying and segmenting NPs [124]. Figure 3.8 presents the original HAADF-STEM image of Pt-Ni NP clusters with the corresponding segmentation images using the global threshold method and the ML model. The results demonstrate that the trained ML model successfully identifies all NPs and segments them

with well-defined outlines, offering higher accuracy in edge detection compared to the traditional global thresholding method. This performance emphasizes the potential of ML-enhanced segmentation in providing more precise and reliable analyses of NP structures.

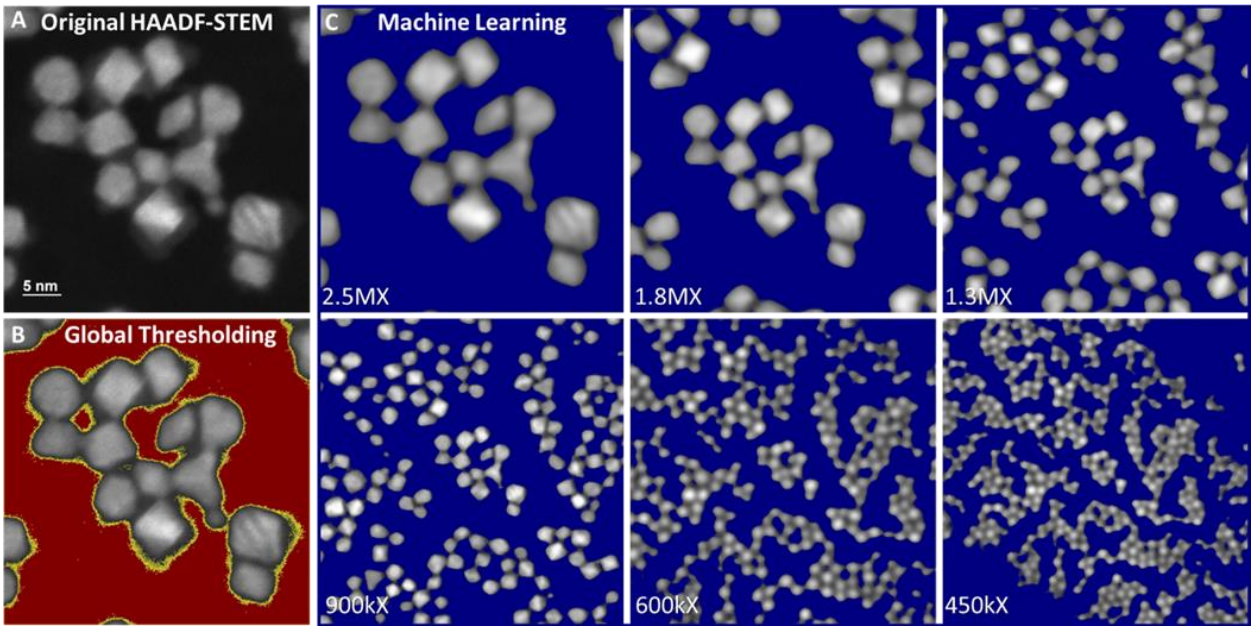


Figure 3.8 Image segmentation of HAADF-STEM images. (A) Original HAADF-STEM image of Pt-Ni NPs. Segmentation of NPs using (B) the traditional global thresholding method, and (C) the ML trained model at different magnifications [125]. Reproduced with permission. Copyright 2023, Oxford University Press.

To determine the detection limit, we systematically assessed the impact of imaging magnification on the quality of ML-based image segmentation (Figure 3.8C). We compared the same NP cluster from HAADF-STEM images taken at magnifications ranging from 450 kX to 2.5 MX and quantitatively analyzed their projected areas and accuracy using precisely measured manual segmentation as the ground truth (Figure 3.9). We found that edge detection accuracy remains above 95% at magnifications greater than 1.0 MX but decreases

significantly at lower magnifications due to reduced pixel resolution. This enables us to establish practical imaging parameters for optimized resolution and field-of-view combinations, ensuring reliable ML-enhanced image segmentation. These findings offer valuable guidelines for improving the accuracy and generalizability of segmentation tasks in data-intensive, high-fidelity TEM/STEM image analyses.

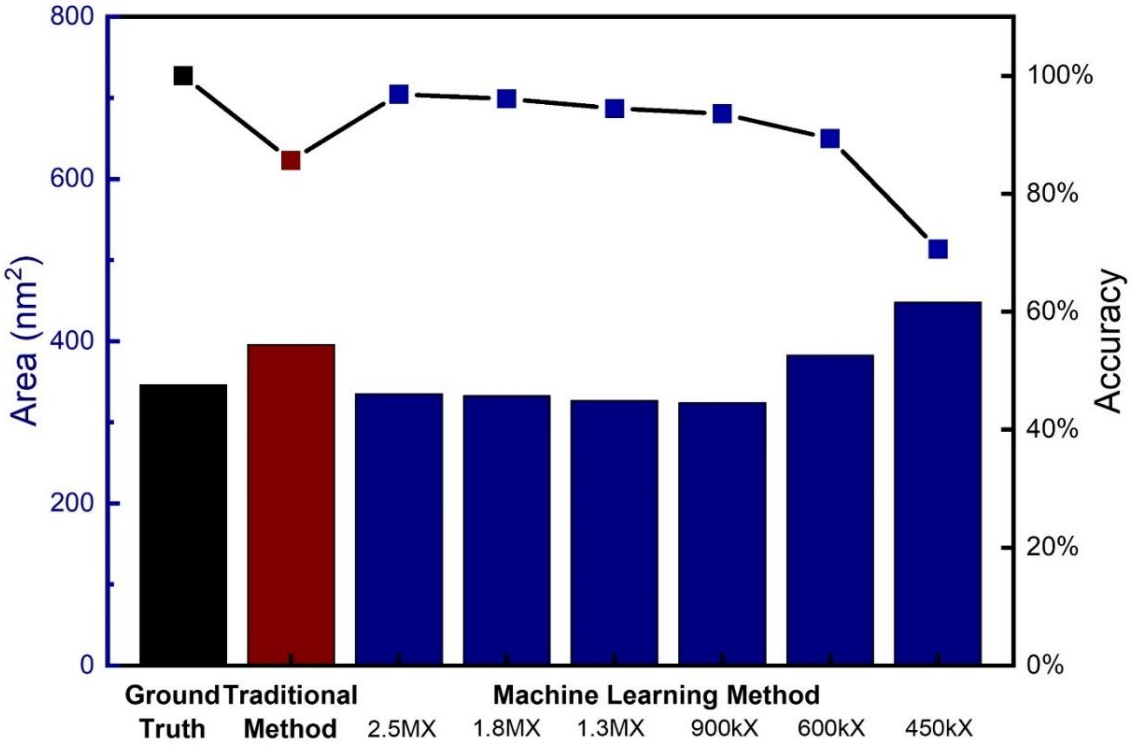


Figure 3.9 Quantitative analysis of image segmentation accuracy of traditional global thresholding method and ML-enhanced method for HAADF-STEM images taken at various magnifications [125]. Reproduced with permission. Copyright 2023, Oxford University Press.

Moreover, the robustness of the U-Net architecture in handling a diverse range of image magnifications highlights its adaptability and generalizability, making it a well-

developed method for high-fidelity image analysis. By maintaining high accuracy across various conditions, this ML-enhanced approach proves to be a valuable tool, offering practical guidelines for improving segmentation tasks in data-intensive TEM/STEM analyses.

In conclusion, we demonstrate the efficacy and advantages of using ML-enhanced segmentation techniques over traditional methods. The detailed investigation into magnification effects and segmentation quality provides critical insights on the imaging conditions and establishes this approach as a well-developed, reliable method for NPs image analysis.

3.4 Conclusions

Overall, AI-enabled microscopy data analytics has utilized advanced ML approaches to develop new capabilities for extracting information from TEM images, diffraction patterns, and analytical spectra with high accuracy and efficiency. In this chapter, we have explored the integration of AI and ML techniques in TEM data analytics and image processing. Specifically, we focused on leveraging ML for TEM image processing, showcasing the potential of CNNs such as U-Net to perform high-precision image segmentation. Our methodology is centered on robust image segmentation and synthetic data generation. The use of U-Net architecture enabled accurate contouring of NP boundaries, while data augmentation techniques ensured model resilience across various imaging conditions. This approach established a solid framework for high-fidelity data interpretation. We first applied ML image segmentation to in situ STEM images to quantify NP behavior at different temperatures, revealing significant trends and underscoring the advantages of automated

analysis over manual methods. Then we studied the compromise between precision and statistics and established the optimized imaging conditions with high accuracy for further analysis. Future work including improving the performance on identifying edges and boundaries with the incorporation of synthetic data as training dataset and using center of mass to predict the merging behavior is needed.

CHAPTER 4 Structural and Chemical Evolutions of Bimetallic Pt-Ni NPs at Elevated Temperatures

Portion of this chapter is a reprint of the material as it appears in "In Situ TEM for Structural and Chemical Evolutions of Bimetallic Pt-Ni Nanoparticles at Elevated Temperatures: Implications for Heterogeneous Catalysis" [Lu, X.; Hwang, S.; He, K., ACS Applied Nano Materials 2024, 7 (13), 15735-15742], used with permission from American Chemical Society.

4.1 Background

NPs have attracted significant attention from the scientific community due to their unique properties substantially distinct from their bulk counterparts, making them foundational building blocks for nanoscience and nanotechnology [126]. Bimetallic NPs have emerged as a leading research frontier due to their unique engineering at the nanoscale, combining two different metals to create a new material with synergistic attributes. These bimetallic NPs offer enhanced physical, chemical, and biological properties, making them highly valuable for diverse applications in catalysis, sensing technologies, biomedical diagnostics, environmental science, and energy sustainability [127, 128]. The design and controlled synthesis of bimetallic NPs represents a notable success in catalysis, leading to significantly enhanced catalytic performance across a wide range of processes. These include organic transformations, fuel cell reactions, and environmental remediation processes [129]. Specifically, Pt-based bimetallic NPs are the subject of substantial research, with potential applications in well-established catalytic processes (e.g., polymer electrolyte membrane fuel cells,[26, 27] water electrolysis) [130] photocatalysis (e.g., photochemical

water splitting) [131] and thermocatalysis (e.g., petrochemicals production [58] automotive exhaust treatment [57]). The catalytic properties such as activity, selectivity, and stability are significantly dependent on catalyst NPs' morphologies, structures, and compositions [61]. Therefore, continued effort is urgently needed to understand and control the geometry, surface facet configuration, compositional distribution and segregation of catalyst NPs [2].

Despite the advancement of catalysts by design, the thermal stability of these materials has always been a major problem for academic and industrial research. Because the compositions and surface structures of crystals under working scenarios are subjected to increased temperatures. Thermal response at high working temperatures is important for improving the design and reliability. Composition redistribution and shape changes at relatively low temperatures have been reported for Pt alloy NPs, which are correlated with the surface structures and facets configuration [71, 72, 97]. Compared to monometallic NPs, the addition of the second element in bimetallic materials introduces additional compositional and structural complications, resulting in diverse configurations such as ordered intermetallic, alloy, core-shell, Janus and so on [15]. This provides more opportunities to finely adjust the catalytic properties by leveraging the combined structural and compositional effects, which are often directly linked to geometric and electronic surface structures [20, 132]. Understanding the transformation pathways of complex structures at high temperatures is crucial, because the structural evolutions and compositional redistributions tend to proceed through independent pathways in response to thermal input, which may not be necessarily coincident to temperature. However, there have been a few investigations into the compositional change inside Pt-Ni NPs, causing the underlying mechanism to have not been fully established.

TEM is a useful tool for characterizing the morphology, structure, and composition of materials from the atomic level to the nanoscale. With recent rapid development, in situ TEM has provided capabilities for observing the real-time evolution of materials during dynamic processes and reactions under various physical or chemical stimuli, offering valuable insights into fundamental understanding of the underlying mechanisms [87]. Previous studies have demonstrated the unique power of such in situ techniques to reveal the dynamics of structural transformations at the atomic scale within individual NPs [72, 133]. In this work, we focus on Pt-Ni NPs as a classic model bimetallic system and use controlled synthesis to produce single-crystalline Pt-Ni NPs in a well-defined truncated octahedral shape with {111} terminating facets with two distinct compositional distributions (core-shell and solid-solution). We utilize in situ heating TEM techniques to examine the thermally induced response of bimetallic Pt-Ni NPs under elevated temperatures. STEM with EDS is used to identify the spatially resolved compositional distribution and evolution during in situ heating, while STEM tomography is also performed to determine the 3D shape of NPs after heat treatments. The microscopic insights gained from in situ TEM observations help obtain a better understanding of the complex structure-composition-coupled transformation mechanisms under thermal treatments, offering new possibilities for achieving synergistic control over morphology, structure, and composition in bimetallic NPs.

4.2 Experimental Methods

In this study, the experiments were designed to synthesize and characterize bimetallic Pt–Ni NPs as well as to understand their structural and chemical evolutions through in situ heating TEM, which is illustrated in Figure 4.1.

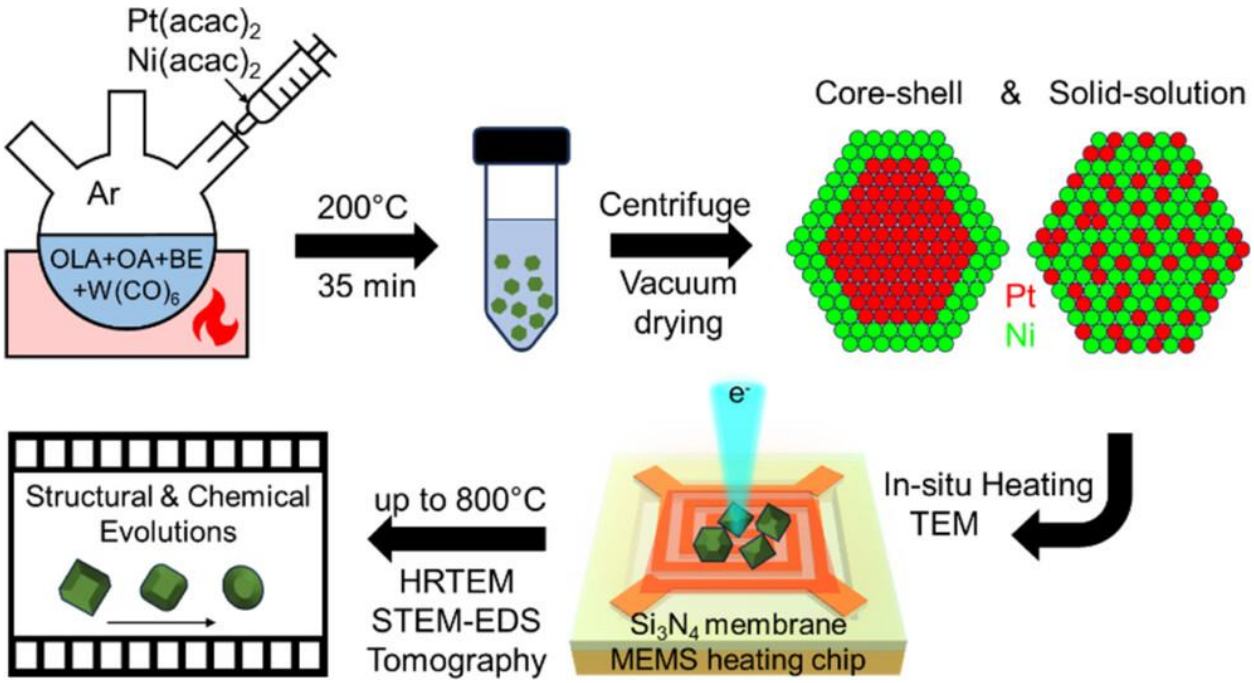


Figure 4.1 Schematic diagram of the synthesis and characterization of Pt–Ni NPs and their structural and chemical evolutions revealed by in situ heating TEM [134]. Reproduced with permission. Copyright 2024, American Chemical Society.

4.2.1 Synthesis of Pt-Ni NPs

Pt-Ni NPs were synthesized using a method modified from a previous study [96]. For a typical synthesis, 7 ml benzyl ether, 2 ml oleylamine, and 1 ml oleic acid were added into a 100 ml three-neck flask, which was placed inside a heating mantle. The temperature was monitored by a thermometer from the solution within the flask. The solution was heated to a desired temperature of 200 °C under Ar protection and with magnetic stirring. After that, 20 mg $Pt(acac)_2$, 10 mg $Ni(acac)_2$, and 60 mg $W(CO)_6$ were added into the solution to produce solid-solution type NPs, and the Ar purging was stopped. Alternatively, 20 mg $Pt(acac)_2$ was added into the solution at RT followed by adding 10 mg $Ni(acac)_2$ at 200 °C to produce core-shell type NPs. Then, the mixture was kept at this temperature for 35 min. The reaction

mixture was cooled down to RT naturally, and the reaction product was centrifuged and washed with ethanol and hexane several times, followed by vacuum drying at 70 °C for 12 h. The resulting Pt-Ni NPs were dispersed in hexane for further characterization.

4.2.2 Materials Characterizations by TEM and XRD

The as-prepared Pt-Ni NPs were dispersed and loaded on a silicon-supported silicon amorphous silicon nitride (Si_3N_4) membrane chip for a DENSsolution Wildfire in situ heating TEM holder. Real-time HRTEM and HAADF-STEM observations were performed using a DENSsolution MEMS-based heating holder on an FEI Talos F200X TEM operated at 200 kV and equipped with a four-quadrant EDS detector for elemental mapping. During a typical in situ heating experiment, the temperature was increased from RT to a desired elevated temperature with an incremental step of 100 °C and the heating rate of 100 °C/s, then the specimen was kept at the same constant temperature for 5 min. The electron dose rate was controlled under ~200 e/(Å^2 s) during data acquisition of in situ heating experiments, while the beam was blanked otherwise to avoid any possible beam-induced artifacts. Atomic-resolution STEM imaging was also performed using an aberration-corrected Hitachi HD2700C STEM operated at 200 kV. Electron tomography of NPs after heating was performed in STEM mode using a JEOL JEM-ARM300F "GrandARM" TEM at 300 kV and a Hummingbird Scientific's tomography TEM holder with a homemade sample clamp fixture. A tilt series of STEM images were collected with the angle interval of 5° and the obtained image data were processed using TomoJ plugin in the ImageJ software to reconstruct 3D tomographic visualization of the NP. X-ray diffraction (XRD) patterns were obtained by a Rigaku Ultima IV powder X-ray diffractometer equipped with a Cu Kα radiation source.

4.3 Results and Discussion

4.3.1 Characterization of As-synthesized NPs

We produced single-crystalline Pt-Ni NPs in truncated octahedral shape with {111} terminating facets (Figure 4.2) through a wet chemistry approach. As illustrated in Figure 4.3, atomically resolved HAADF-STEM image with FFT clearly shows visible atomic columns throughout a typical Pt-Ni NP along the $[\bar{1}10]$ zone axis, revealing the well-defined geometry and the high crystallinity of as-synthesized NPs. The lattice spacings of the adjacent fringes parallel to the Pt-Ni NP terminating facet were 0.225 nm, which is consistent with the {111} crystalline plane of a face-centered cubic (FCC) lattice structure. Also, 0.196 nm lattice-spacing was assigned to the {002} crystalline plane, corresponding to the truncated corners along [001] directions. The SAED pattern exhibits a series of diffraction rings corresponding to the FCC lattice planes of {111}, {200}, {220} and {311} (Figure 4.3c). Meanwhile, the XRD pattern (Figure 4.3d) shows diffraction peaks (2θ angles of 41.3°, 48.0°, 70.0° and 84.7°, shown in Figure 4.4) corresponding to the characteristic peaks of {111}, {200}, {220} and {311} planes of Pt-Ni fcc structure, respectively. Moreover, the rotationally averaged SAED radial profile shows a consistent match with the XRD curve, confirming the pure and uniform solid-solution phase (without any intermetallics) of Pt-Ni NPs [135], which is likely attributed to the low colloidal synthetic temperature (200 °C) and the off-stoichiometry (Pt:Ni ~ 57%:43%, measured by EDS) that do not favor the formation of intermetallic compounds such as $L1_0$ and $L1_2$ phases [136]. HAADF-STEM images and the corresponding STEM-EDS elemental maps are shown in Figure 4.3e and f. By adjusting the sequence of adding Pt and Ni metal precursors, we synthesized Pt-Ni NPs exhibiting two distinct structures in terms of different elemental distributions. While the EDS mapping in Figure

4.3e shows the uniform single-phase solid-solution configuration, the EDS mapping in Figure 4.3f shows that the Pt elements are concentrated in the center and Ni elements are rich on the surface of the NP, representing a core-shell structure with Pt in the core and Ni on the shell (also shown in the linescan profiles in Figure 4.5). The core–shell chemical configuration can also be consistently confirmed by the XRD pattern (Figure 4.4), which indicates obvious peak splitting arising from two separated Pt-rich and Ni-rich phases. It is also confirmed by XRD and EELS that no oxide (i.e., NiO) can be detected from the core–shell Pt–Ni NPs. These baseline characterizations of as-synthesized single-crystalline Pt-Ni NPs confirm the two compositional distributions by our design, which serve as ideal systems for the following in situ heating experiments.

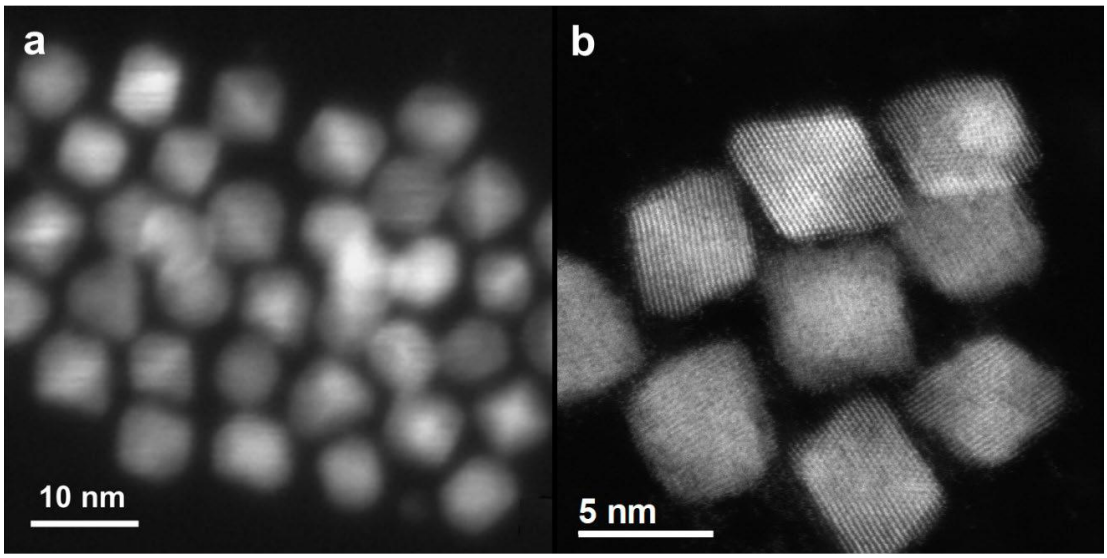


Figure 4.2 STEM images of as-synthesized Pt-Ni NPs. (a) Low-magnification and (b) high-magnification STEM images demonstrating the homogeneous truncated octahedral shape and monodisperse size of Pt-Ni NPs.

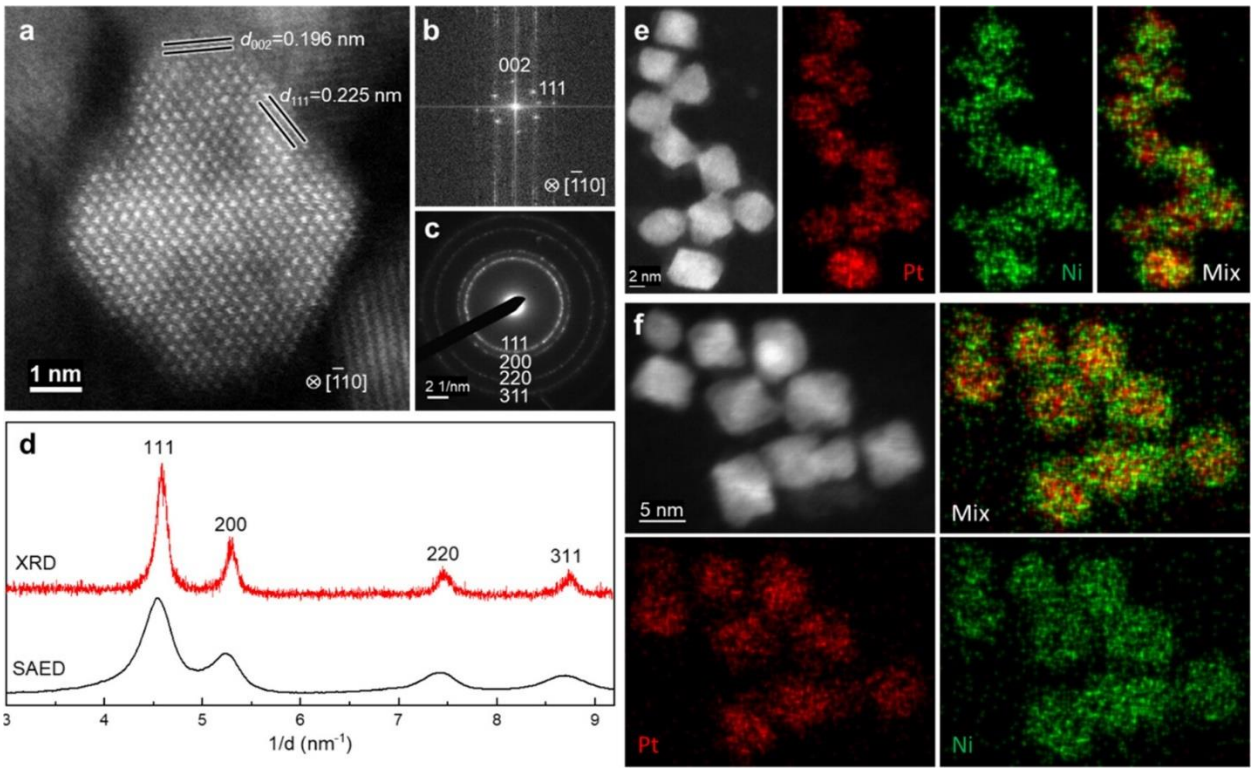


Figure 4.3 Structural and compositional characterizations of as-synthesized Pt-Ni NPs. (a) Atomically resolved HAADF-STEM image, and (b) the corresponding FFT pattern, of an individual Pt-Ni NP. (c) SAED pattern taken from numerous Pt-Ni NPs. (d) XRD pattern and rotationally averaged SAED radial profile showing the pure solid-solution phase of Pt-Ni NPs. HAADF-STEM image and the corresponding EDS elemental maps of (e) solid-solution, and (f) core-shell, Pt-Ni NPs [134]. Reproduced with permission. Copyright 2024, American Chemical Society.

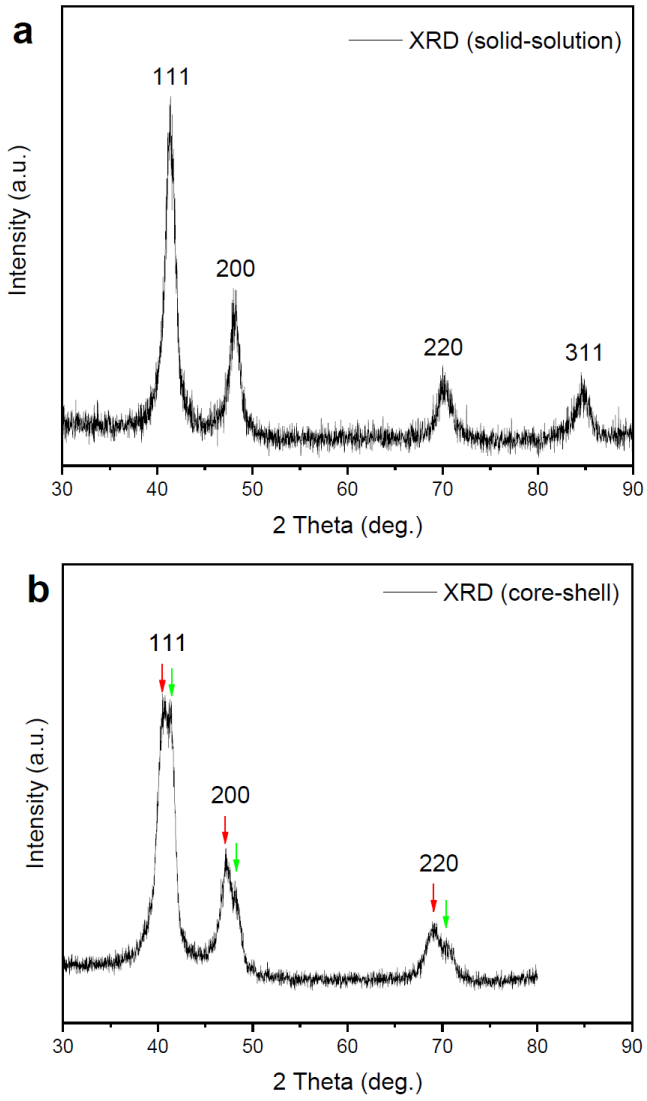


Figure 4.4 XRD pattern of as-synthesized Pt-Ni NPs. (a) The XRD pattern of solid-solution Pt-Ni NPs, in which four characteristics peaks are found at 41.3°, 48.0°, 70.0° and 84.7°, corresponding to {111}, {200}, {220} and {311} planes, with inversed lattice spacing (1/d) values of 4.58 nm^{-1}, 5.28 nm^{-1}, 7.45 nm^{-1}, and 8.75 nm^{-1}, respectively. (b) The XRD pattern of core-shell Pt-Ni NPs, in which peak splitting is found for {111}, {200}, and {220} planes due to the separated phases consisting of the Pt-rich solid-solution core (labeled by red arrows) and the Ni-rich shell (labeled by green arrows).

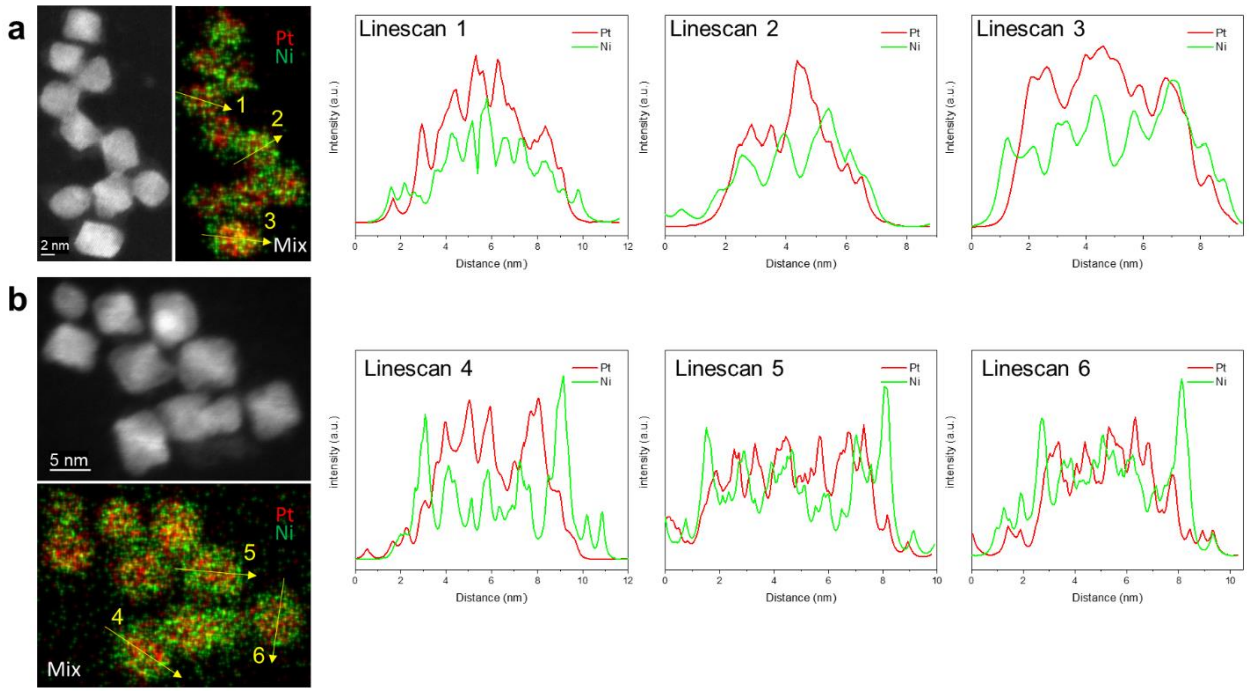


Figure 4.5 STEM-EDS analysis of as-synthesized Pt-Ni NPs. (a) STEM-EDS mapping and linescan profiles obtained from 3 different solid-solution NPs. (b) STEM-EDS mapping and linescan profiles obtained from 3 different core-shell NPs.

4.3.2 Thermally Induced Morphological Evolution of Single NP

Shape Evolution and Facet Development

First, to reveal the morphological and surface structure evolutions, we performed in situ heating TEM for an individual Pt-Ni NP in HRTEM mode, as shown in Figure 4.6. The metallic atom columns were spatially resolved by HRTEM along the [110] zone axis (Figure 4.6a), which allows us to track the morphological evolution by quantifying the projected atom column positions. To simplify this process, we used a model-based approach to generate [110]-oriented atomic images and find the closest match to experimental images (Figure 4.7) to help identify all atom positions (yellow overlays) and terminating facets (color lines). This allows us to further measure the number of core and surface atomic

columns (Figure 4.6b) as well as the length of each terminating facet (Figure 4.6c) during the entire heating process, thereby providing statistical analysis of the structural evolution during facet development. For a representative Pt-Ni NP, the pristine state at RT is stabilized by low-index facet termination, with the vast majority being {111}, {110}, and {100} facets. At the early stage of heating (up to 300 °C), the NP was terminated mainly by low-index facets {111}, {100}, and {110} along with an increasing number of {311} facets, while the NP tended to form a corner-rounded geometry, manifested by the decrease of the surface-to-core atom ratio. Starting at 400 °C, more high-index facets {422} appeared to mitigate the number of {311} facets. Since the surface energy (γ) of noble metals generally follows the order of $\gamma_{\{111\}} < \gamma_{\{100\}} < \gamma_{\{110\}} < \gamma_{\{hkl\}}$ ({hkl} denoting for high-index planes with at least one Miller index larger than 1) [137], the appearance of high-index facets is due to the increase of total surface energies of the NP caused by the thermal input from the environment [138]. When heated up to 500 °C, {511} facets were developed by replacing the {311} facets and some of the {422} facets. When the temperature reached 600 °C, high-index facets were largely phased out, leaving behind the most low-index facets termination to allow the NP to transform into a more isotropic shape. At this stage, the projected area reached the lowest value, implying the completion of the surface reduction process which changes the NP into a spherical-like 3D geometry. Upon further heating the NP to the range of 700-800 °C, its projected area was subject to a noticeable expansion, along with mixed facet developments including some high-index facets appearing (such as {511}, {422}, and {331}) and vanishing (such as {311}). Such an unusual size expansion at high temperatures was unexpected. With the assumption of no interparticle mass transfer for this isolated NP system, we hypothesize that the lateral expansion at 700 to 800 °C is likely due to the particle-substrate interaction which changes

the spherical geometry to a pancake-like shape in 3D, which was further validated by electron tomography shown below (Figure 4.8a). Although the statistical analysis and the relevant results shown in Figure 4.6b, c present the information only along the [110] orientation, it still provides a greatly representative foundation to infer possible evolutions in 3D space. The temperature-dependent in situ heating TEM observations have revealed the overall facet development during the corner-rounding and surface reduction process at elevated temperatures.

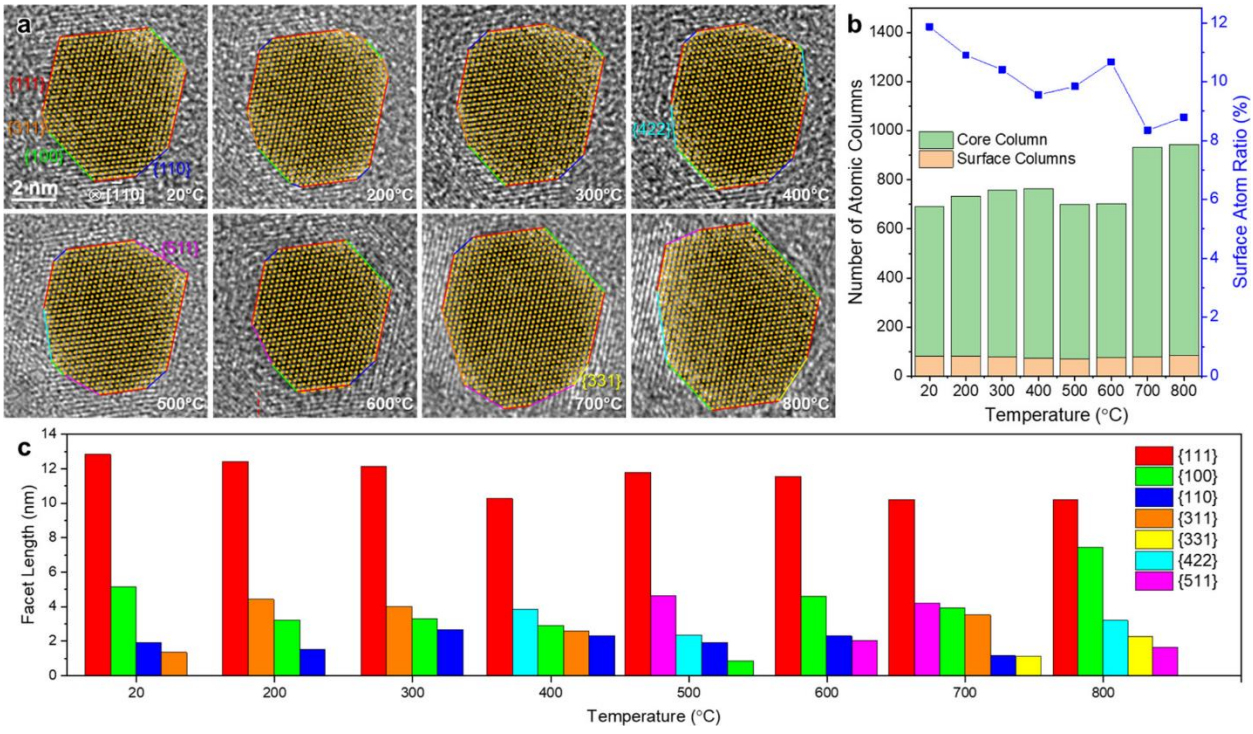


Figure 4.6 Morphological evolution and surface facet development observed by in situ heating TEM. (a) In situ HRTEM images viewed along [110] zone axis showing the morphological evolution of a Pt-Ni NP as a function of temperature from 20 to 800 °C. The color lines indicate different surface facets. (b) The measured surface columns and (c) facet

length at different temperatures [134]. Reproduced with permission. Copyright 2024, American Chemical Society.

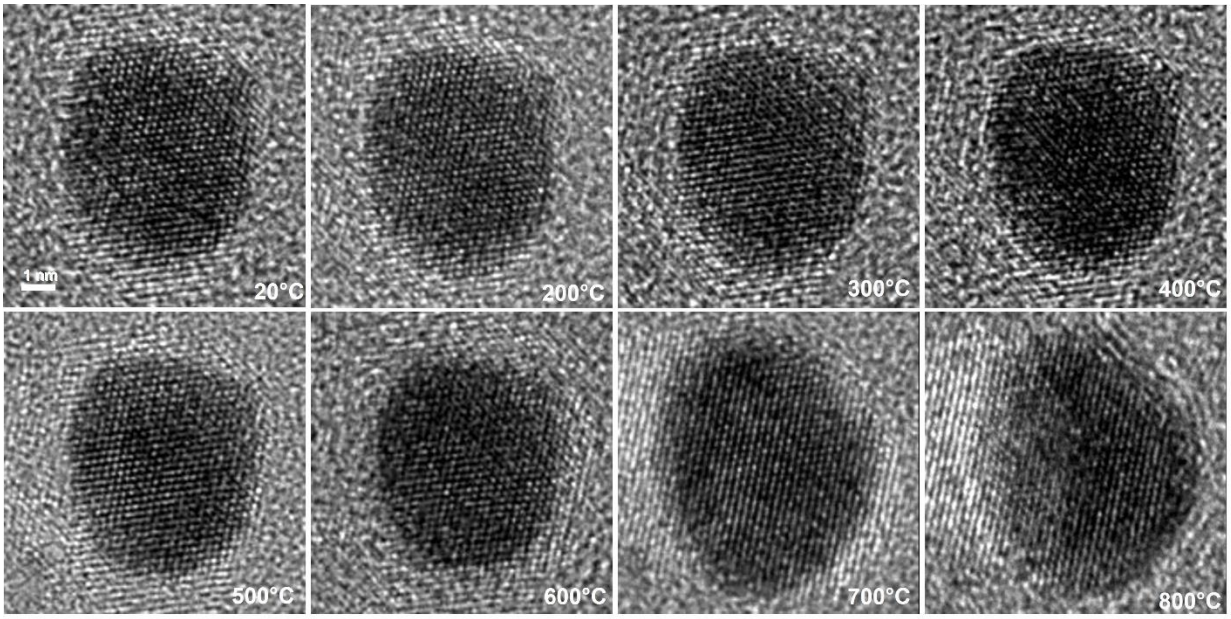


Figure 4.7 HRTEM images showing the evolution of Pt-Ni NPs under in situ heating from 20 to 800 °C.

Visualization of Three-Dimensional Structure

Based on the in situ heating experiments, we propose that the structural evolution following two primary stages (Figure 4.8a), (i) facet development that tends to round the corners of pristine truncated octahedron due to entropic effects, especially at elevated temperatures [139], and reduce the total facet exposure to minimize the surface energy, and (ii) particle-substrate interaction that attracts the atoms migrate from NP to the substrate to improve contact and interfacial wetting. To test our hypothesis about the second stage and understand the NP expansion observed at 700-800 °C, we performed electron tomography in STEM mode by conducting a tilt series HAADF-STEM imaging of a NP (Figure 4.9) after in

situ heating experiments, allowing us to visualize the stereoscopic geometry of the NP through 3D reconstruction. Figure 4.8b shows the tomographic reconstruction of 3D visualization of a Pt-Ni NP as well as its projection view (Figure 4.8c) in the x-y plane and side view (Figure 4.8d) in the x-z plane (z-axis is the electron beam direction). The projection view displays a shape like the final state after in situ heating at 800 °C in Figure 4.6a, while the side view renders the cross-section of an ellipsoid NP geometry, which is shortened along the vertical direction but flattened and enlarged laterally, consistent with our inferred pancake-like shape giving rise to the areal expansion. A similar shape was also found in previous work of annealed Pt particles [140]. The morphology and size change could be attributed to the wetting behavior of the composing elements interacting with the substrate to minimize the overall interfacial energy [141]. Such temperature-induced wetting also happened on Pt NPs on silica surface, which can be attributed to the interfacial mixing of Pt and SiO_2 and the resulting negative interface energy [142]. Overall, besides the insights of surface facet development with the propagation of low-index and high-index crystal planes upon heating, it is also crucial to be aware of the unavoidable particle-substrate interaction that would significantly modify the interfacial wetting behavior, which may facilitate the atom migration and mobilization at high temperatures.

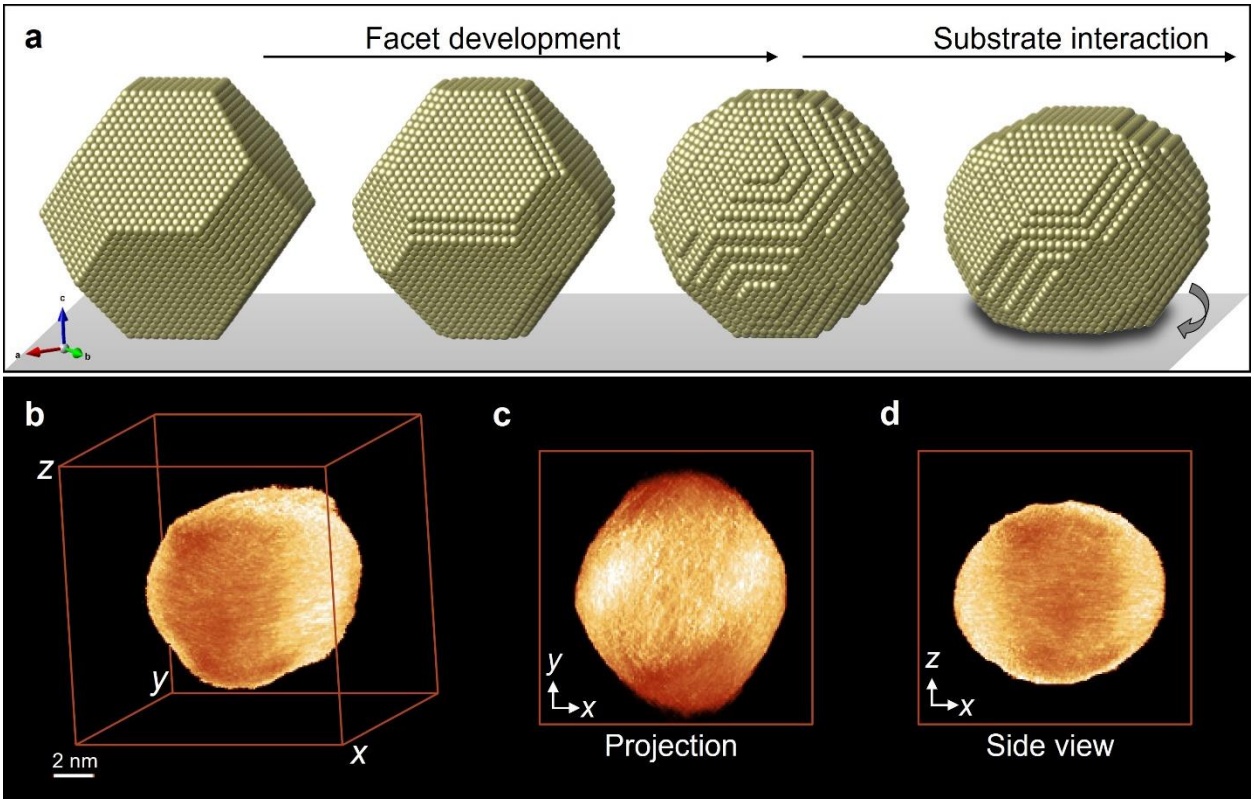


Figure 4.8 Tomographic visualization of the NP after heating. (a) The atomic model showing the thermally induced structural evolution of a Pt-Ni NP through two stages including the facet development and the particle-substrate interaction. (b) 3D visualization of a NP rendered from STEM tomography reconstruction. The surface rendering of the 3D reconstruction along (c) the projection view, and (d) the side view [134]. Reproduced with permission. Copyright 2024, American Chemical Society.

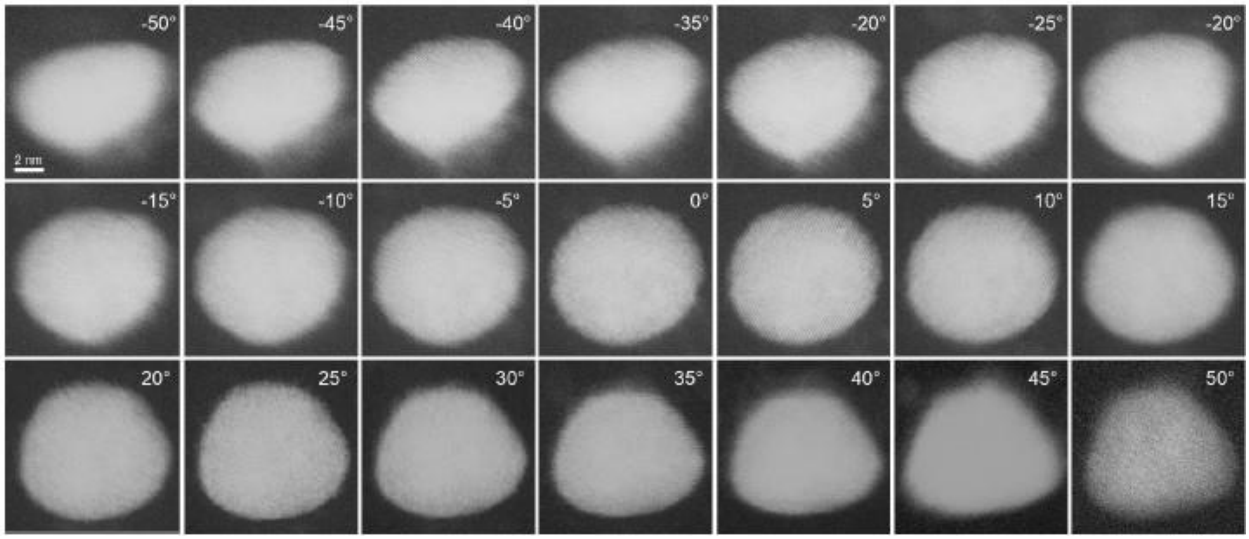


Figure 4.9 HAADF-STEM tomography tilt series images of a NP after in situ heating.

4.3.3 Thermally Induced Chemical Evolutions of NPs Clusters

Maintained Solid-solution Structure

In addition to the structural evolution revealed above, it is expected that the two composing elements, Pt and Ni, would also be subject to different types of migrations to be redistributed within the bimetallic NP and form distinct compositional configurations. From this perspective, we use as-synthesized Pt-Ni NPs with two distinct compositional configurations (i.e., solid-solution and core-shell) as different start points and perform in situ heating to investigate their chemical evolutions as a function of temperature. To minimize the electron beam induced effects (such as irradiation damage to NPs, local electron heating, etc.), we chose to conduct simultaneous STEM imaging and EDS acquisition after heating to certain temperatures, while the beam was kept blank during heating to ensure there was no beam-induced damage during the in situ experiments. Figure 4.10 shows the HAADF-STEM images and the corresponding STEM-EDS maps of solid-solution NPs during in situ heating. The compositional configuration remained a solid-solution type throughout the entire

heating process from RT to 800 °C. Additionally, individual NPs started to coalesce into a connected cluster at elevated temperatures between 700 and 800 °C. This indicates that interparticle mass transfer was facilitated by the surface atom migration through the enhanced NP wetting to the substrate, which led to the lateral expansion of individual NPs and narrowed down the gaps between adjacent NPs, eventually making these NPs merge. This phenomenon matches with the findings above.

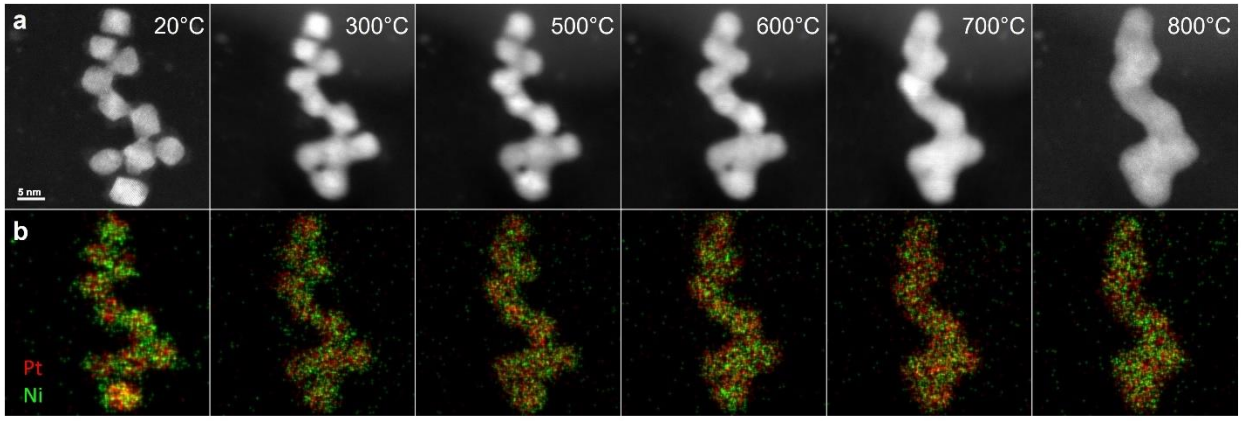


Figure 4.10 Compositional evolution of solid-solution Pt-Ni NPs. (a) HAADF-STEM images and (b) the corresponding STEM-EDS maps of solid-solution Pt-Ni NPs captured at different elevated temperatures during in situ heating [134]. Reproduced with permission. Copyright 2024, American Chemical Society.

Core-shell to Solid-solution Transformation

Similarly, we conducted in situ heating experiments for core-shell Pt-Ni NPs. Figure 4.11 shows HAADF-STEM images and corresponding EDS maps from RT to 800 °C. It is found that the core-shell structure was retained up to 300 °C, and mostly remained in the core-shell state during 300-400 °C (Figure 4.12). Starting from 500 °C, Ni atoms, initially situated in the shell, were redistributed into the core of the NP. Further heating to 600 °C resulted in

the complete mixing of Pt and Ni within the NP. When the temperature reached 700 °C, obvious interparticle mass transfer would occur to initiate the coalescence of multiple NPs into a connected cluster, which was finally merged into a single large particle at 800 °C. This coalescence behavior is consistent with the results shown above. After returning to RT, the merged large particle remains in the solid-solution state, indicating that the core-shell to solid-solution transformation is an irreversible process. The compositional reconstruction of the core-shell NPs under thermal input is described as the chemical homogenization of Pt and Ni atoms between the core and the shell within the NP. This process, where the surface energy dictates the diffusion of Pt and Ni, ultimately leads to the assimilation of Pt and Ni atoms, forming a uniformly mixed solid-solution alloy structure [143]. This homogeneous structure is expected due to the entropy stabilization, favoring the formation of a solid solution instead of phase separations or intermetallic compounds [144]. Similar transformations into homogeneous compositional configurations have also been observed in previous studies involving Ni-Co and Co-Pt core-shell NPs [21, 145].

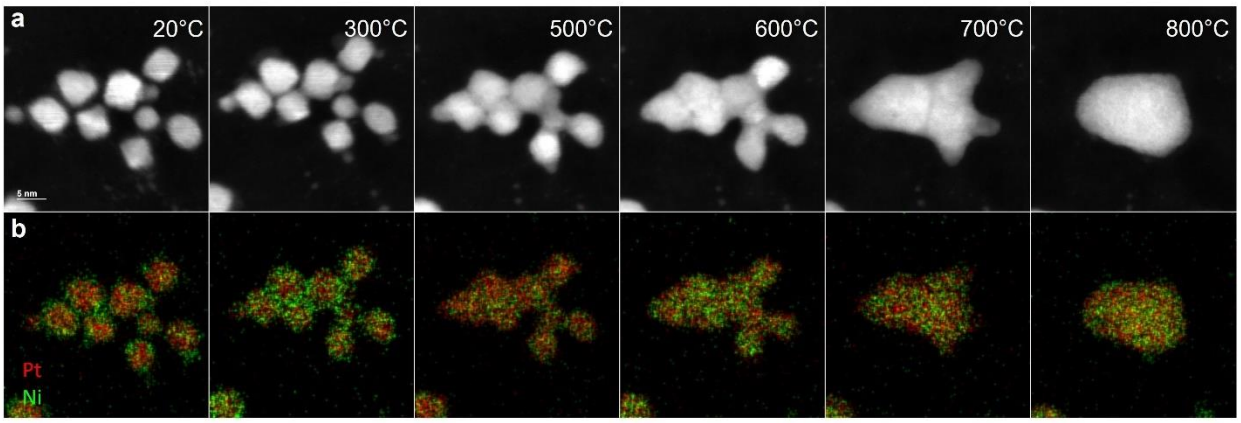


Figure 4.11 Compositional evolution of core-shell Pt-Ni NPs. (a) HAADF-STEM images and (b) the corresponding EDS maps of core-shell Pt-Ni NPs captured at different elevated

temperatures during in situ heating [134]. Reproduced with permission. Copyright 2024, American Chemical Society.

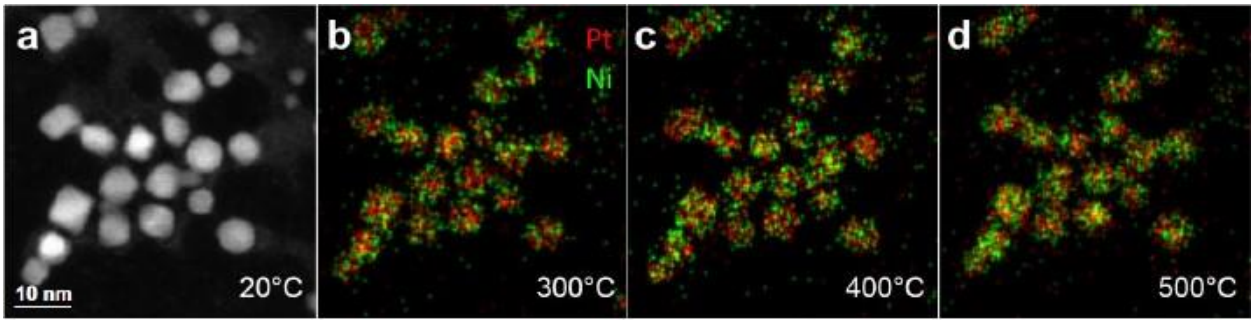


Figure 4.12 Compositional evolution of core-shell Pt-Ni NPs in the temperature range of 300-500 °C. (a) HAADF-STEM image taken at RT. STEM-EDS mapping obtained at (b) 300 °C, (c) 400 °C, and (d) 500 °C during in situ heating. STEM-EDS maps indicate that the Pt-Ni NPs remain mostly in core-shell state under 300 to 400 °C, while transforming into solid-solution state at 500 °C.

4.3.4 ML-assisted Images Analysis

Here, the ML image segmentation method described in Chapter 3 was applied to the Pt-Ni NPs system to quantify the evolution behavior at elevated temperatures. Figure 4.13a shows the in situ heating STEM images of Pt-Ni NPs, illustrating the morphological changes occurring at various temperatures. Figure 4.13b displays the ML segmentation of the in situ heating images. The segmentation model effectively identifies and outlines each NP, allowing for precise measurement of their shapes and sizes. Figure 4.13c shows the contoured images derived from the ML segmentation. These contoured images provide a clear visualization of the NPs' boundaries, enhancing the understanding of their structural transitions. The

contours highlight the changes in the projected areas and shapes of the NPs, offering a detailed view of the morphological evolution as the temperature rises.

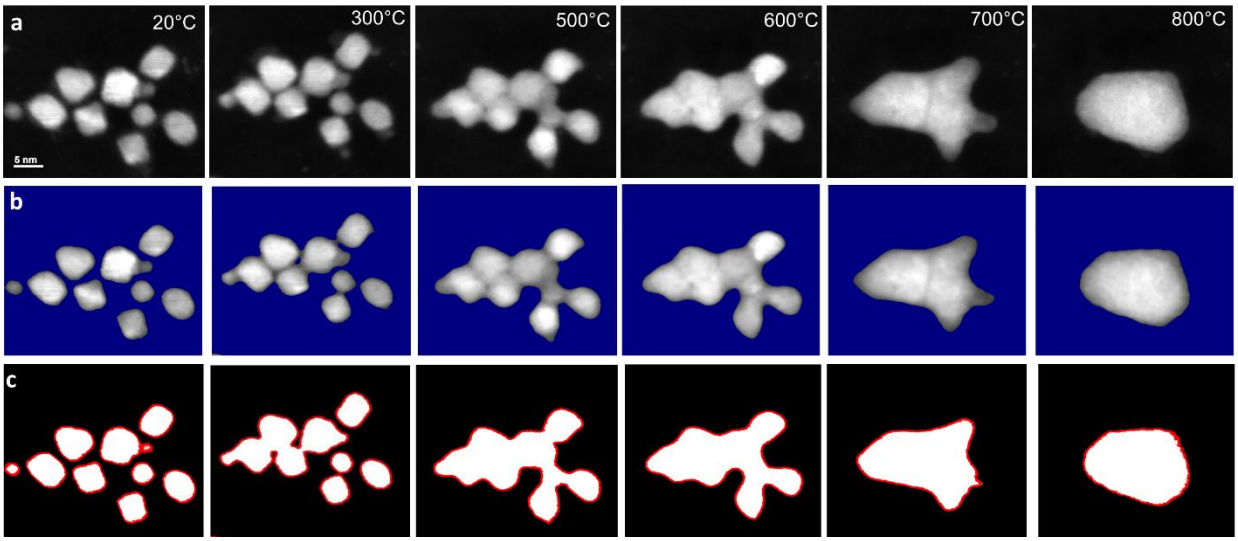


Figure 4.13 (a) In situ heating of Pt-Ni NPs, (b) the ML segmentation and (c) contoured HAADF-STEM images.

Table 4.1 summarizes the measurements of the number and projected area of NPs obtained from in situ STEM images. The data shows a consistent trend where the number of distinct NPs decreases while their average projected area increases with rising temperature. This indicates coalescence and growth of the NPs, driven by surface atom migration and interfacial wetting. From this result, Figure 4.14 shows the three different stages of NPs evolution. At RT, Pt-Ni NPs exhibit well-defined truncated octahedral shapes with distinct facets. As the temperature increases to 400 °C, the individual NPs undergo facet development, where their high index facets become more pronounced. When the temperature rises to 650 °C, interparticle mass transfer begins to occur. In this stage, atoms start to migrate between adjacent NPs, leading to changes in their sizes and shapes. The NPs

may begin to form necks or bridges between each other, indicating the onset of coalescence processes. The ML segmentation accurately captures these subtle changes, providing detailed information on the evolving NP structures. At higher temperatures to 800 °C, the NPs undergo significant coalescence. During this stage, neighboring NPs merge to form larger particles with increased projected areas. The original distinct boundaries between NPs blur as they coalesce into single larger entities. This process is facilitated by the enhanced atom mobility at higher temperatures, leading to the formation of pancake-like ellipsoid shapes. The ML segmentation and contoured HAADF-STEM images clearly show the merging of NPs and the resulting changes in their morphology.

Table 4.1 Measurement of number and projected area of NPs from in situ STEM images.

Temperature/°C	Number of NPs	Total projected area /nm^2
20	9	191
300	5	196
500	1	228
600	1	231
700	1	194
800	1	190

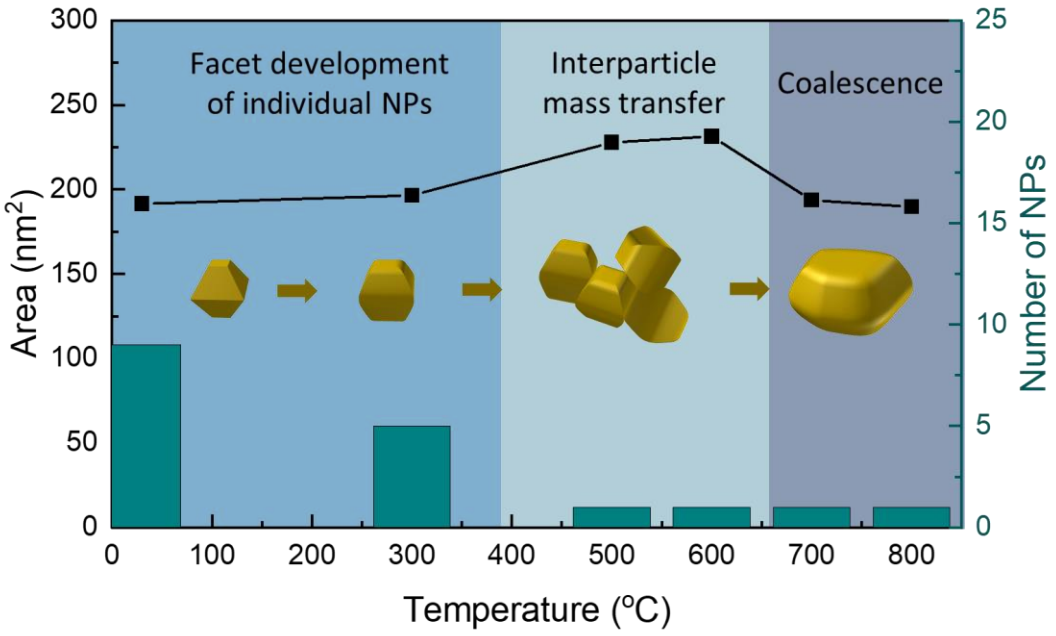


Figure 4.14 Measured number of NPs and projected area indicating different stages of NPs evolution at elevated temperatures.

4.4 Conclusions

In conclusion, we conducted in situ heating experiments on truncated octahedral Pt-Ni NPs with solid-solution and core-shell compositional structures using TEM. Our findings show the morphological evolution and facet development as a function of temperature, ranging from RT to 800 °C. We found a general structural evolution involving two stages, i.e., (i) the facet development process, where the truncated octahedral NP undergoes corner-rounding and surface reduction evolutions along with the appearance and vanishing of various high-index facets during the course, and (ii) particle-substrate interaction, which enables surface atom migration to flatten the NP from spherical-like to pancake-like shape. The electron tomography reveals the 3D visualization of a NP after heating, confirming the

geometric modification and wettability of NPs with the substrate at high temperatures. Through in situ STEM-EDS mapping, we comparatively investigated the evolution of compositional configurations in solid-solution and core-shell Pt-Ni NPs and found that solid-solution configuration remains stable while core-shell configuration tends to be disrupted and transformed to solid-solution state through chemical homogenization at 500 to 600 °C. Upon further heating to a higher temperature of 700 to 800 °C, the individual NPs start to coalesce due to the facilitated surface atom migration induced by particle-substrate interaction. These observations provide important insights into the structural and chemical evolution of bimetallic Pt-Ni NPs, aiding in the design of catalysts with improved geometric and compositional configurations for enhanced performance and stability in heterogeneous catalysis.

CHAPTER 5 Structural and Chemical Evolutions of Quinary PdCuPtNiCo NPs at Elevated Temperatures

5.1 Background

HEMs have received considerable critical attention in recent years due to their unique properties and wide applications led by their multielemental composition and solid-solution structure. By changing the added metal species and inducing the anion source, versatile HEMs could be obtained. In 2004, Yeh et al. introduced the concept of HEAs [30]. Bulk HEAs are difficult to use for catalytic applications due to their low surface area and low number of active sites. Compared with the bulk counterpart, HEA NPs with more than 5 kinds of metal elements and homogeneous mixing structures own large surface area and enriched catalytic active sites, therefore demonstrating excellent catalytic performances on both thermocatalysis and electrocatalysis reactions [32, 33].

Characterization plays an important role in confirming the uniform mixing of elements. Electron microscopy techniques as powerful tools including TEM, and STEM can provide useful information such as morphology and size of the materials. In particular, HAADF-STEM could reach an atomic resolution to identify the locations of different metal atoms [146]. When combining STEM with spectroscopy techniques, EDS and EELS can determine the elemental distribution and composition, chemical bonds, valence states, and electronic structures, which is critical to providing evidence of the homogeneity of HEAs.

To gain better knowledge of the transformation of materials reacting to a certain environment, in situ TEM has been used to directly observe the process by applying one or multiple physical stimuli such as heat, force, light, electrical bias, magnetic field, electron

beam, cooling or gases and liquids [87, 147]. To date, there have been few studies about the evolution of HEAs under various environments via in situ TEM [148, 149]. In situ heating TEM at high temperatures has been employed mostly to perform the stability test of high-entropy NPs. For example, RuRhCoNiIr NPs demonstrated high structural stability with uniform dispersion and size stability annealing up to 500 °C [150]. FeCoNiCuPd HEA NPs shrunk with the preferential sublimation of the Cu component after 700 °C [151]. For multimetallic NPs with different mixing patterns, it is necessary for a fundamental understanding of real-time evolution and reaction pathways. Higher temperature annealing is of interest to examine the thermal and phase stability of those NPs.

Here, we studied the high-temperature behavior of core-shell and HEA PdCuPtNiCo NPs in a vacuum environment. We propose the hypothesis that different starting points and mass transfer lead to different final stages. Because HEA NPs are loaded on carbon support, the atoms are not mobilized. Their high-entropy homogeneous mixing would maintain well after heating. For core-shell NPs, if a single one is isolated from others, given the result we found in the last Chapter, the core-shell structure would transform to solid-solution at certain temperatures. If there are neighbor NPs with atom transfer, they may merge into a big NP with solid-solution structure. However, since there are 5 metal elements comprising this NP, due to the potential synergistic effect, the phase-segregated structure could also happen at elevated temperatures. To test the hypothetical routes, the structural and compositional evolutions during heating from RT to 1000 °C are captured in real-time through in situ STEM imaging and EDS analyses.

5.2 Experimental Methods

5.2.1 Synthesis of PdCuPtNiCo NPs

NPs containing Pd, Cu, Pt, Ni, and Co were synthesized by graduate student Nabojit Kar from Prof. Sara Skrabalak group at Indiana University Bloomington based on the method in a previous study [35]. The details of the methods used by Nabojit are described below.

Synthesis of Core-shell NPs

To start, intermetallic PdCu NPs were synthesized with slight modifications to a previous method [152]. In a 100 mL three-neck round-bottom flask, 0.2 mmol of $PdBr_2$, 0.2 mmol of $Cu(ac)_2$, 9 mL of oleylamine, and 40 µL of oleic acid were added. This mixture was heated under vacuum while stirring at 110 °C for 10 minutes. Next, 60 µL of trioctylphosphine (TOP) was added, and the reaction solution was heated to 235 °C under an argon atmosphere for 30 minutes. After cooling to RT, the solution was centrifuged at 3900 rpm for 10 minutes to remove large particles. The supernatant containing the particles was then precipitated by adding a 3:1 acetone/ethanol mixture and collected by centrifugation at 10,000 rpm. The particles were washed with a 5:1 ethanol/hexane mixture and, after removing the supernatant, were resuspended in 3 mL of hexane and 16 mL of a 2:1 acetone/methanol solution for storage.

To synthesize quinary PdCu@PtNiCo NPs, PdCu seeds were added to a 100 mL three-neck round-bottom flask containing 4 mL of oleylamine, 5 mL of 1-octadecene, $PtBr_2$, $Ni(acac)_3$, and $Co(ac)_2{\cdot}4H_2O$, with metal precursor concentrations calculated to maintain a 1:1 ratio of seed to metal precursors. 1,2-Dodecanediol was added at a 20:1 ratio of 1,2-dodecanediol to metals. This mixture was heated to 110 °C under vacuum for 30 minutes,

then to 235 °C under argon for another 30 minutes. After cooling to RT, the solution was centrifuged at 3900 rpm for 10 minutes to remove large particles. The supernatant was precipitated with a 3:1 acetone/ethanol mixture and collected by centrifugation at 10,000 rpm. The sample was washed with a 5:1 ethanol/hexane mixture, and the particles were resuspended in hexane for further use [35].

Synthesis of HEA NPs

The quinary PdCu@PtNiCo NPs were deposited onto a carbon support (Ketjen EC-600JD) at a mass ratio of 1:9. The NPs were added dropwise to a slurry of the carbon support in 5 mL of acetone and 2.5 mL of hexane. After adding the NPs, the solution was sonicated for 1 hour and left to stir overnight. The solvents were then evaporated, and the resulting solids were dissolved in an acetone solution by sonicating, after which they were transferred onto a quartz crucible. The boat containing the sample was centered in a fused silica tube and heated in a tube furnace. The fused silica tube was purged with a H_2/N_2 (4 v/v %) mixture for 30 minutes, followed by heating the sample to 600 °C for 10 hours at a ramp rate of 20 °C per minute.

5.2.2 Materials Characterizations by TEM

NPs dispersion was drop-casted onto a MEMS heating chip using a DENSsolutions Wildfire in situ heating TEM holder. The heating chip was put into Fischione Model 1020 plasma cleaner under O_2 and Ar for 2 min to remove existing carbonaceous debris from the specimen and prevent contamination. In situ HAADF-STEM images and EDS mapping were acquired on a FEI Talos F200X TEM/STEM operated at 200 kV with a four-quadrant 0.9-sr EDS spectrometer. Temperature was directly ramped up from RT to a certain temperature

with a 100 °C interval. The sample was maintained for about 5 min for imaging and mapping. Atomic HAADF-STEM images were acquired by a spherical aberration-corrected JEOL JEM-ARM 300F "GrandARM" TEM with a cold field emission source operating at 300 kV, at 53 mrad convergence semi-angle.

5.3 Results and Discussion

5.3.1 Characterization of As-synthesized NPs

The morphology and chemical composition of as-synthesized core-shell and HEA NPs were characterized by STEM and EDS. HAADF-STEM image in Figure 5.1a shows that the core-shell NPs are mostly spherical with particle sizes around 10 nm. Figure 5.1b,c show the atomic resolution HAADF-STEM images of two individual NPs. The contrast difference between core and shell areas suggests the heterogeneity of elemental distribution. The lattice can be indexed to the ⟨-110⟩ zone axis with (002) and (111) planes. The elemental distribution was confirmed by STEM-EDS mapping as shown in Figure 5.1g. The core consists of Pd and Cu, while the shell consists of Pt, Ni and Co. Figure 5.1e shows the spherical HEA NPs supported on carbon with sizes around 10 nm. The atom-to-atom contrast variation in the HAADF and ABF images shown in Figure 5.1e,f suggest a homogeneous mixing of all 5 elements at the atomic level. Inset in the ABF image shows the FFT patterns in the ⟨-110⟩ zone axis with (002) and (111) planes, demonstrating the single-phase with fcc crystal structure. The composition uniformity was confirmed by STEM-EDS mapping in Figure 5.1h. These characterization results confirm that all synthesized NPs have the desired shape, size and elemental compositions for both materials. Elemental analysis measured by ICP-MS (Table 5.1) confirms the presence of all the anticipated metals, ranging from 14 at% to 28 at%.

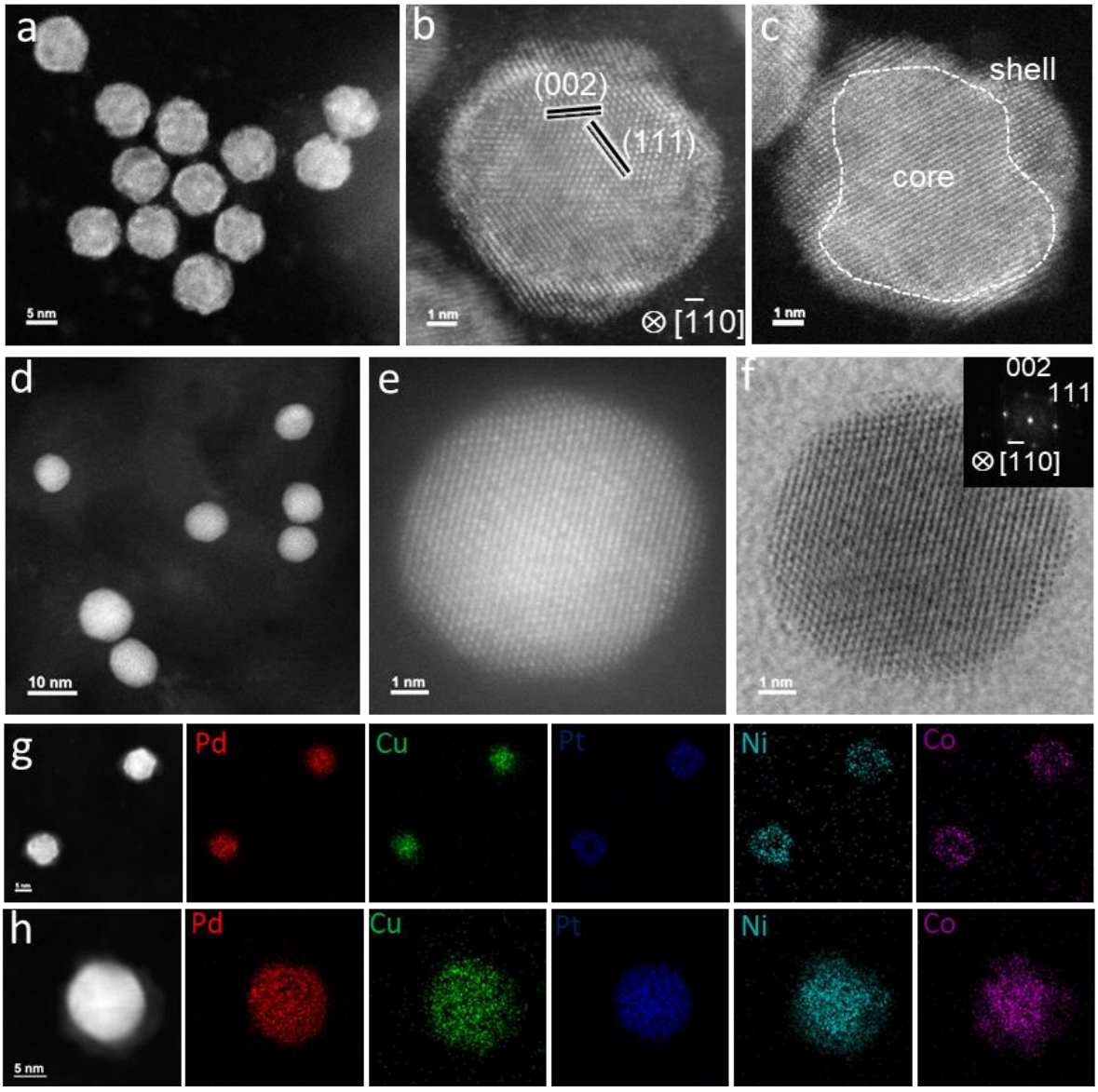


Figure 5.1 Atomic structure and compositional characterizations of as-synthesized NPs. (a) HAADF-STEM image of core-shell PdCu@PtNiCo NPs. (b) (c) Atomically resolved HAADF-STEM image of an individual PdCu@PtNiCo NP. (d) HAADF-STEM image of HEA PdCuPtNiCo NPs. (e) Atomically resolved HAADF-STEM image and (f) ABF image of an individual HEA PdCuPtNiCo NP. HAADF-STEM image and the corresponding EDS elemental maps of (g) core-shell, and (h) HEA NPs.

Table 5.1 Atomic percentage obtained from ICP-MS measurement for core-shell and HEA NPs.

Element	at% of core-shell NPs	at% of HEA NPs
Pd	28.64	28.48
Cu	20.47	20.51
Pt	14.69	15.08
Ni	18.89	20.77
Co	17.31	15.16

5.3.2 Thermally Induced Chemical Evolutions of HEA NPs

We initially investigated the transformations of HEA NPs loaded on carbon during heating. Figure 5.2 presents HAADF images alongside EDS maps for Pd, Cu, Pt, Ni, and Co at various temperatures. At RT, the HEA NPs exhibit a homogeneous distribution of all five elements. However, at 700 °C, Cu and Ni began to evaporate, indicated by the outward diffusion of their EDS signals. This phenomenon can be attributed to the nanoscale size of the particles and the high vapor pressure of Cu relative to the other metals studied [41]. Table 5.2 summarizes the vapor pressure data of the studied metal elements. Despite these changes, the overall homogeneous structure of the HEA NPs was maintained throughout the heating process. Graphitization of the supported carbon was also observed. As the temperature increased, the carbon support began to undergo structural transformation into graphite. This graphitization was especially pronounced for pairs of neighboring HEA NPs, leading to the encapsulation of these NPs within a graphite shell, as shown in Figure 5.3. The process of graphitization involves the reorganization of carbon atoms into a more ordered, crystalline graphite structure, which can encapsulate and overcoat the NPs [153]. Since these NPs are anchored on the carbon support, there was no mass transfer happening between

neighboring NPs, preventing them from merging. This anchoring effect stabilizes the positions of the NPs, as illustrated in Figure 5.3.

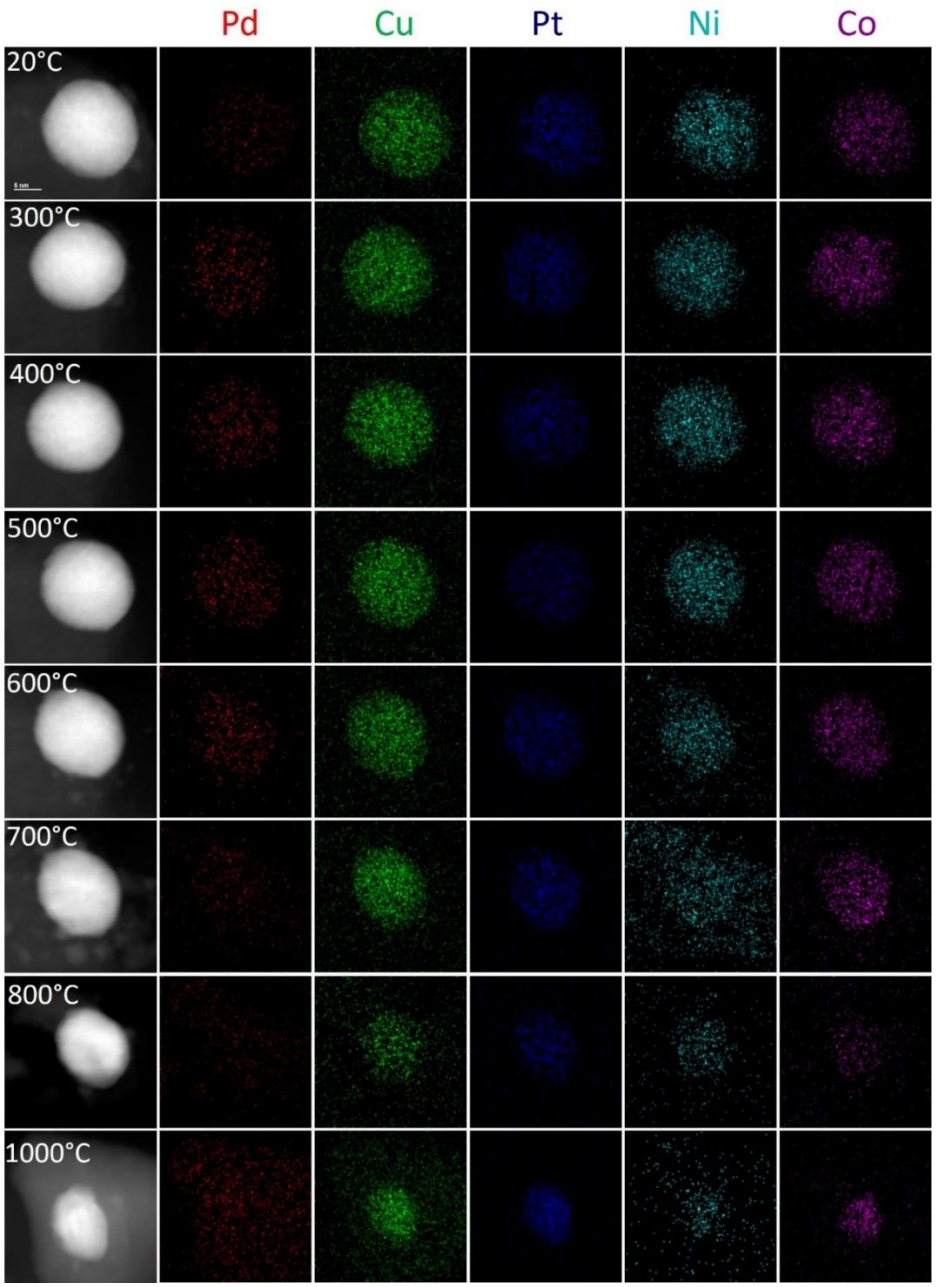


Figure 5.2 Compositional evolution of HEA PdCuPtNiCo NPs. HAADF-STEM images and the corresponding STEM-EDS maps captured at different elevated temperatures during in situ heating.

Table 5.2 Vapor pressure data.

Element	Melting Point [°C]	Temperature [°C] at vapor pressure [mbar]			
		10^{-7}	10^{-5}	10^{-3}	10^{-1}
Pd	1555	903	1072	1298	1615
Cu	1085	775	922	1117	1387
Pt	1768	1374	1596	1889	2289
Ni	1455	988	1155	1373	1669
Co	1495	983	1148	1364	1657

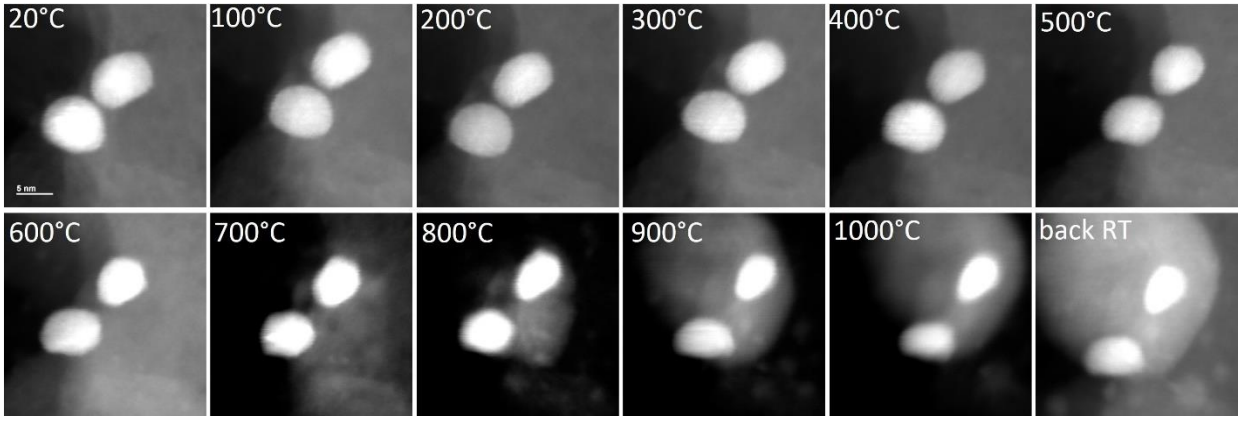


Figure 5.3 HAADF-STEM images showing the evolution of HEA PdCuPtNiCo NPs on carbon under in situ heating from 20 to 1000 °C.

5.3.3 Thermally Induced Chemical Evolutions of Single Core-shell NPs

Evolution without Mass Transfer

The evolution process is more complicated for core-shell NPs because of their unstabilized entropy and heterogeneous structure. In the first scenario, if one NP is isolated from all other NPs and there is nearly no mass transfer with it, the evolution route is similar to HEA NPs. Figure 5.4 shows the in situ STEM-EDS maps of an example isolated single NP. It showed nonuniform elemental distribution at RT. At 300 °C, gradual inward and outward diffusion of all elements started, leading to the homogeneous structure at 800 °C. However, the diffusion of these metals occurred not exactly simultaneously due to the inhomogeneity of as-synthesized NP. Cu has the highest diffusibility at 400 °C followed by Co and Ni, which is in agreement with experimental observations that the outward diffusion of Cu is more notable than Co and Ni [148]. Upon heating to 1000 °C, the homogeneous structure maintained well.

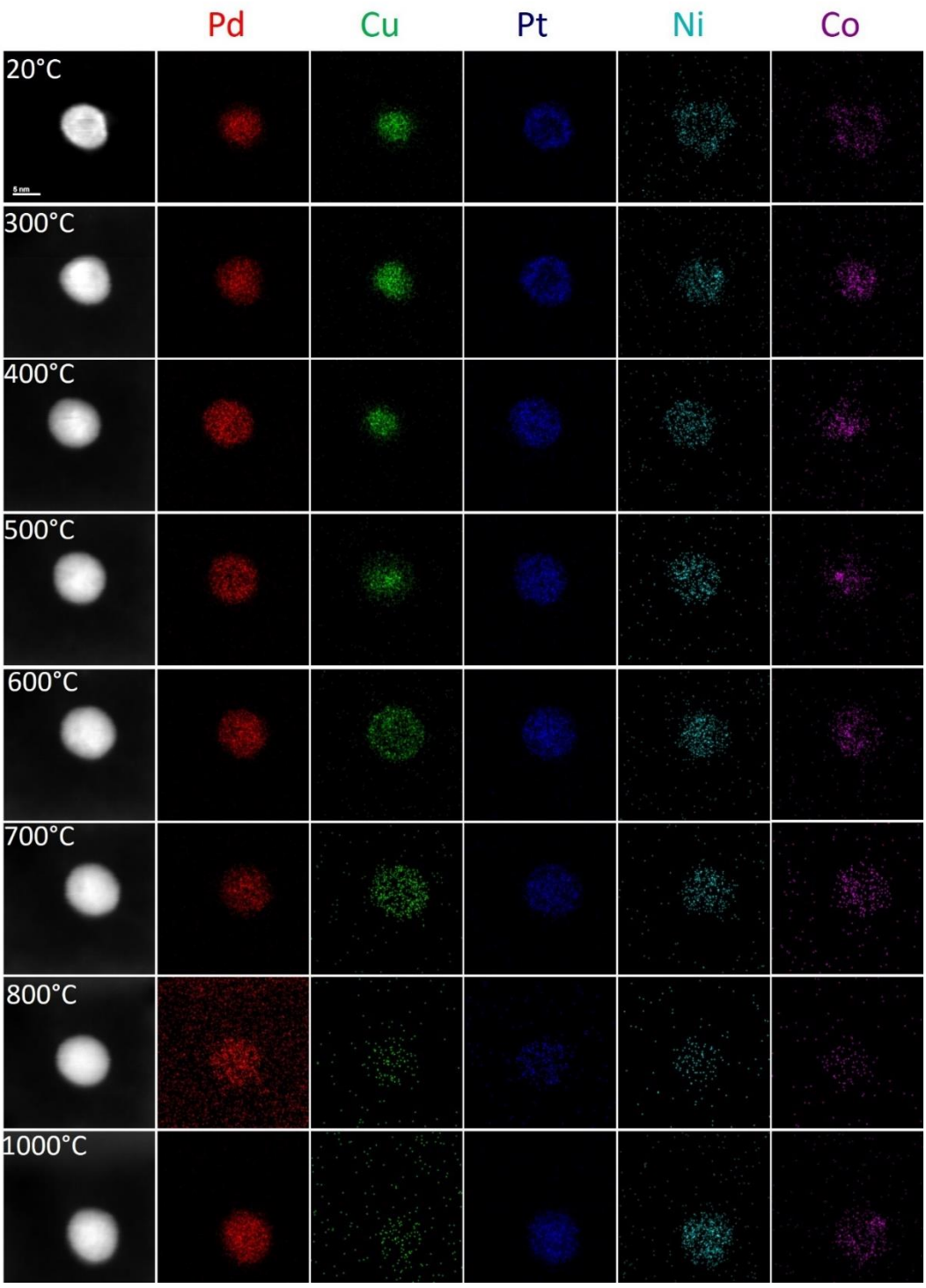


Figure 5.4 Compositional evolution of core-shell PdCu@PtNiCo NPs with nearly no mass transfer. HAADF-STEM images and the corresponding STEM-EDS maps captured at different elevated temperatures during in situ heating.

Evolution with Interparticle Mass Transfer

However, in another observation shown in Figure 5.5, we found that one core-shell NP displayed a different evolution route than above. From the EDS maps, Cu started to diffuse outward and Pt and Ni started to diffuse inward at 400 °C. At 500 °C, these 3 elements already distributed uniformly within the NP, however, Pd and Co still mainly located at their previous places. Due to the metal evaporation of Cu at 700 °C, its signal spread over the NP. Similar metal evaporation of Cu also took place. The HAADF-STEM image at 800 °C shows the contrast difference, revealing the heterostructure of the heated NP. After heating at 1000 °C, the phase segregation process completed, and the EDS maps showed the featured Janus configurations with PdPt parts and NiCo parts. We further studied the reason that caused the phase separation. From the HRTEM image taken at 800 °C (Figure 5.6a), some small atom clusters appeared near the observed NP on the background with relatively low contrast. From the EDS mapping in Figure 5.6b, these background atom clusters consist of mainly Pd and possibly Cu. We speculate that they came from incomplete synthesis of the metal precursors and became more visible due to the long time of beam irradiation and increased temperature. There would be possible interactions between these atom clusters with actual NPs through atomic diffusion on the membrane support [154]. More evidence of other post-heating Janus NPs is presented in Figure 5.7. These NPs are all in the single NP scale with no merging with neighbor NPs, and they all exhibited phase segregation after heating.

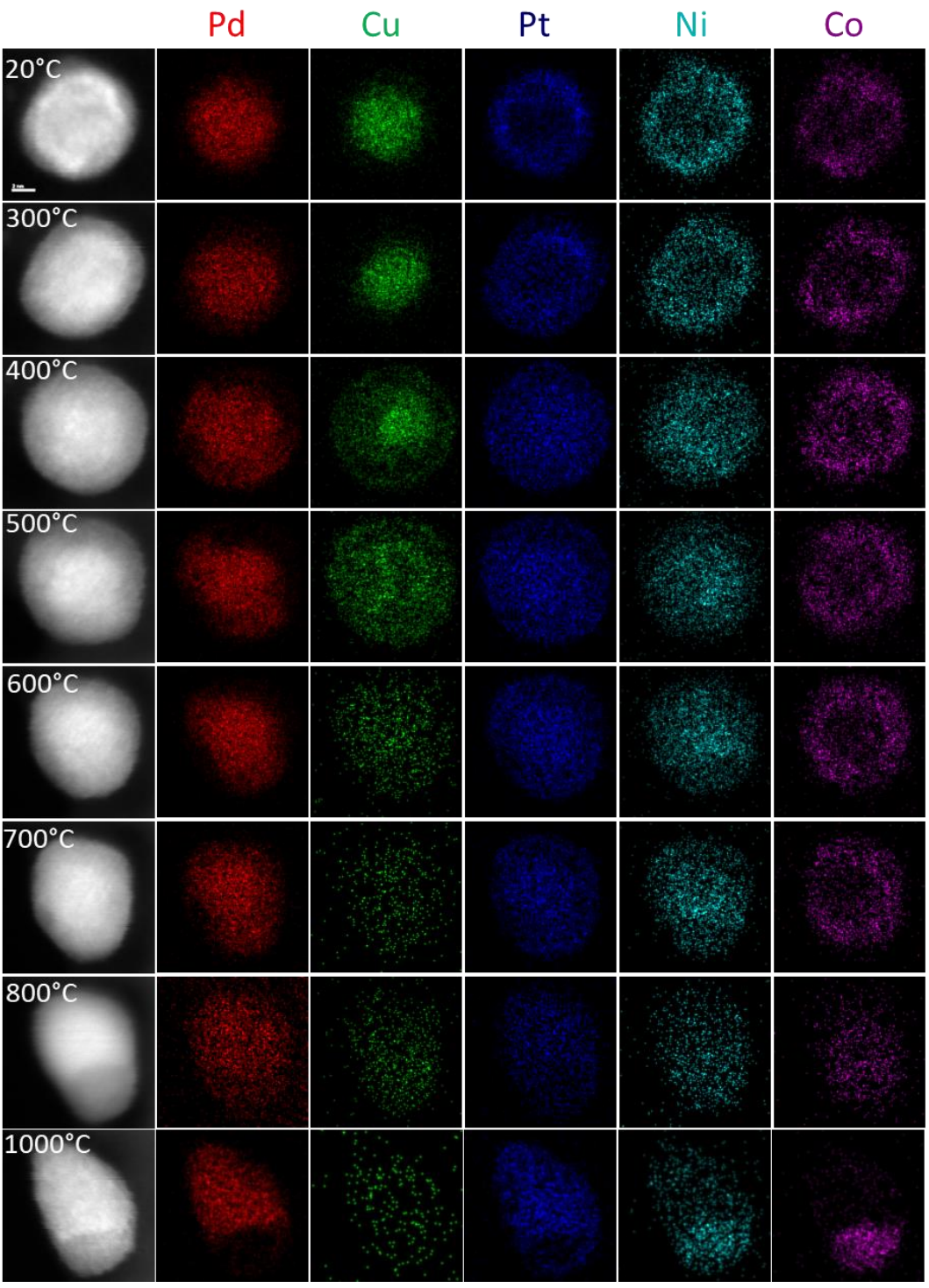


Figure 5.5 Compositional evolution of core-shell PdCu@PtNiCo NPs with mass transfer. HAADF-STEM images and the corresponding STEM-EDS maps captured at different elevated temperatures during in situ heating.

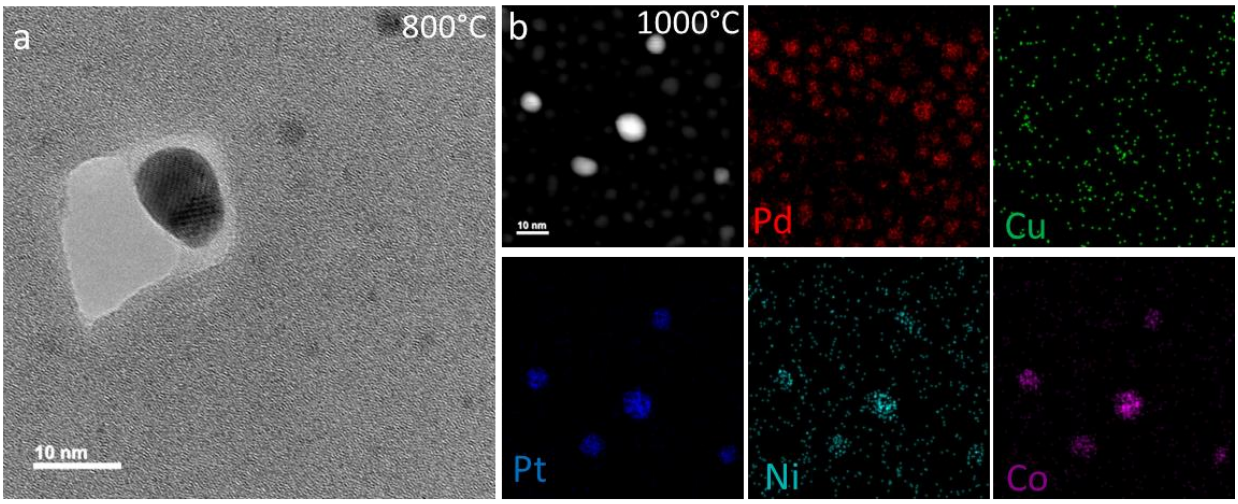


Figure 5.6 Characterization of background low-contrast small clusters. (a) HRTEM image of a core-shell PdCu@PtNiCo NP at 800 °C. (b) HAADF-STEM image and corresponding EDS maps at 1000 °C.

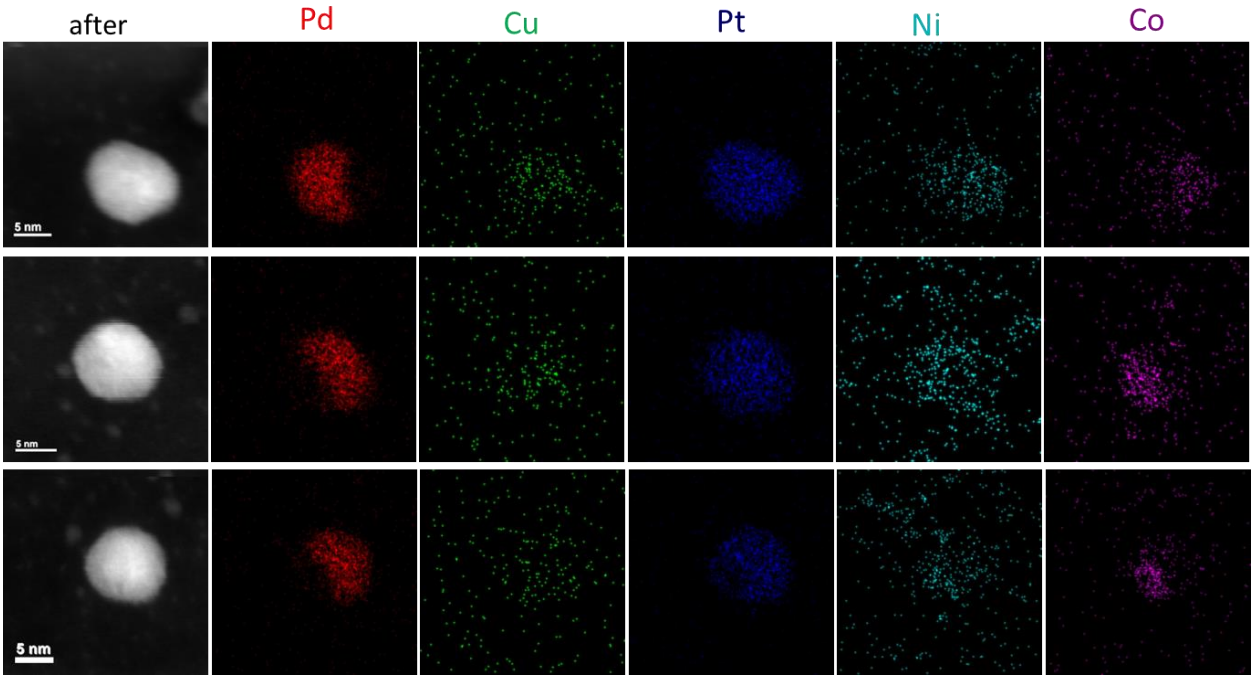


Figure 5.7 HAADF-STEM images and corresponding EDS maps of 3 core-shell PdCu@PtNiCo NPs after heating with phase segregation.

5.3.4 Thermally Induced Chemical Evolutions of Neighbor Core-shell NPs

When there are 2 neighbor NPs within near distances and no carbon support under them, they would merge via coalescence. Figure 5.8 shows the series of STEM-EDS maps at different temperatures with in situ monitoring. For each NP, the elemental evolution process is similar to the individual NP in Figure 5.7. The merging started with a neck connecting 2 NPs from 500 °C. From the EDS maps, the neck mainly consists of Co. The reason for this is that among the 3 shell elements, Co has the highest diffusibility. The outward Co diffusion of the neighbor NPs formed a bridge leading to the coalescence. When the temperature increased to 800 °C, the sphere parts of these 2 NPs were touching and both NPs showed a homogeneous alloy structure. However, once the temperature increased to 1000 °C, the 2 NPs quickly merged and formed the Janus structure with PdPt on one side and Co on the other side. We also captured other NPs post-heating to verify the universality of this phenomenon, as shown in Figure 5.9. If there are multiple NPs within the near distances, the phase segregation would also take place with more than 2 parts.

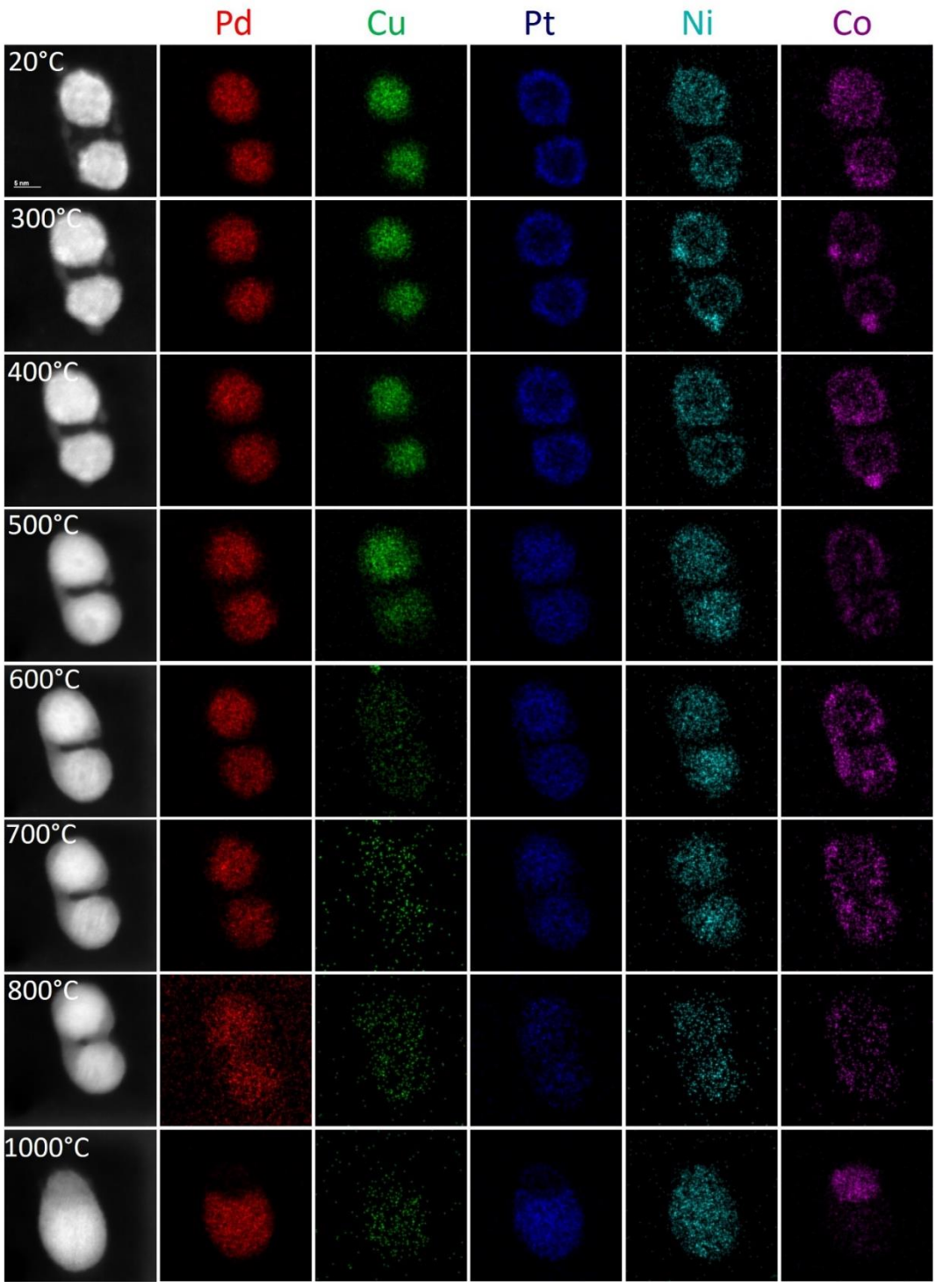


Figure 5.8 Compositional evolution of core-shell PdCu@PtNiCo NPs with coalesce. HAADF-STEM images and the corresponding STEM-EDS maps captured at different elevated temperatures during in situ heating.

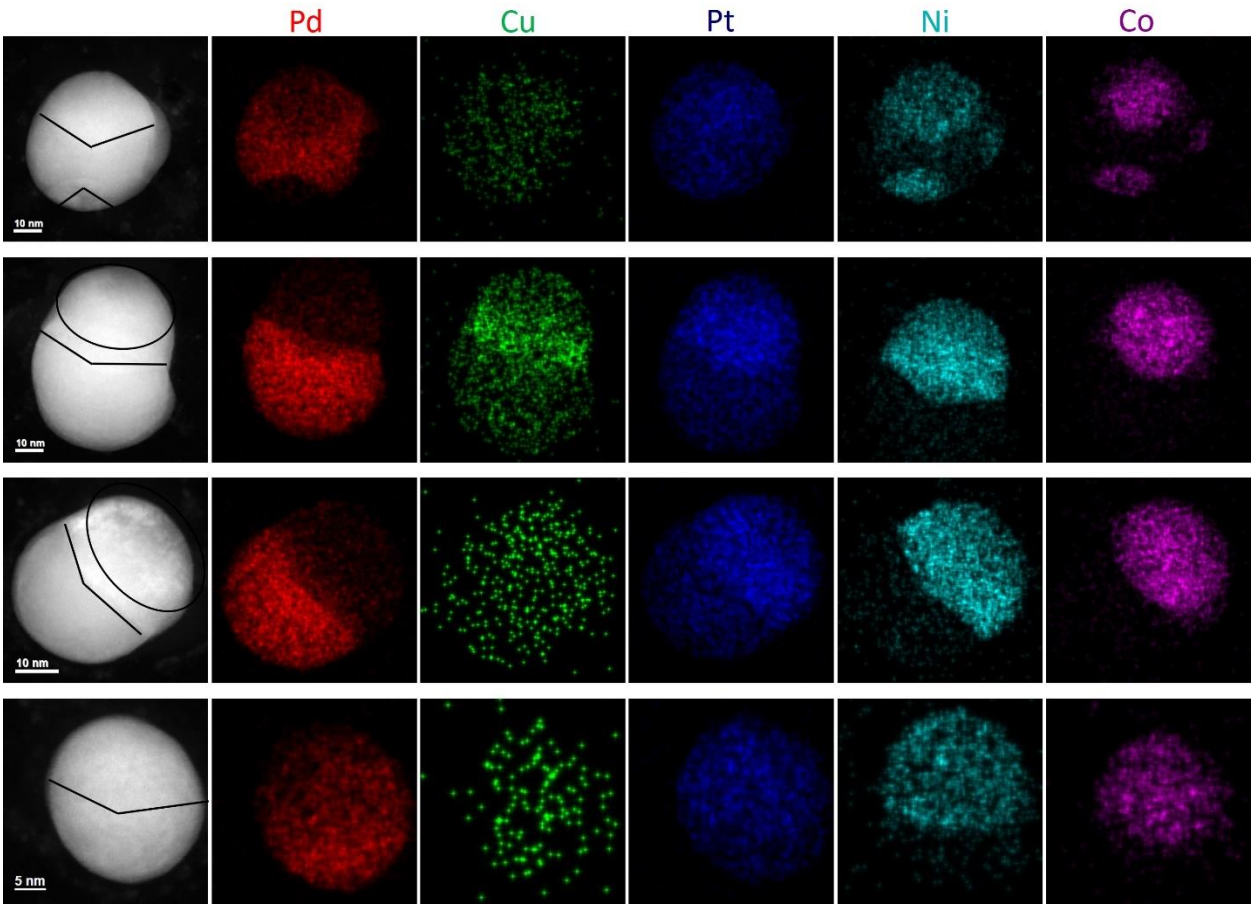


Figure 5.9 HAADF-STEM images and corresponding EDS maps of 4 coalesced core-shell PdCu@PtNiCo NPs after heating.

5.3.5 ML-assisted Images Analysis

The ML image segmentation method described in Chapter 3 was applied to the core-shell PdCu@PtNiCo NPs to quantify their behavior at elevated temperatures. Figure 5.10a displays the in situ heating STEM images, showing the morphological changes at different temperatures. Figure 5.10b shows the contoured images derived from the ML segmentation, where the segmentation model accurately identifies and outlines each NP.

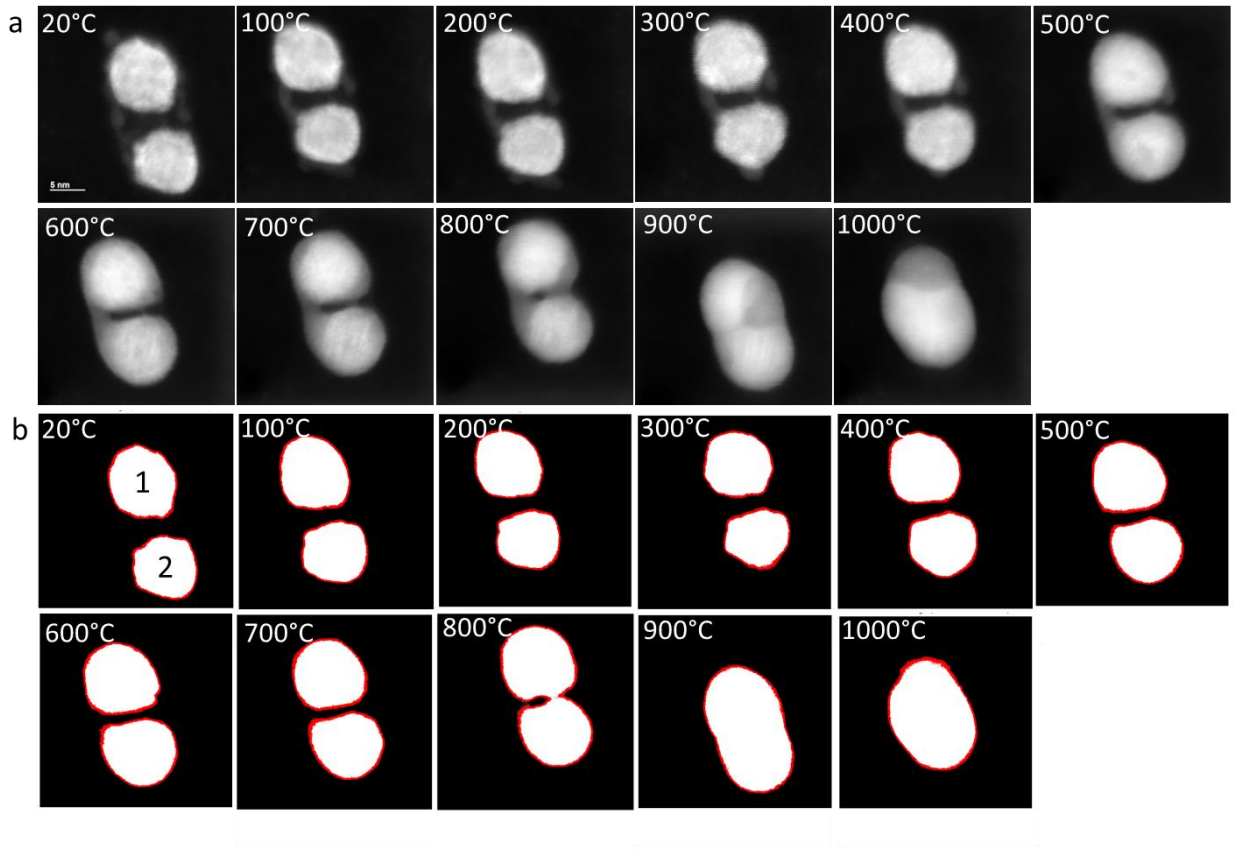


Figure 5.10 (a) In situ heating HAADF-STEM images of core-shell PdCu@PtNiCo NPs, and (b) contoured images using ML segmentation.

Table 5.3 summarizes the measurements of the number and projected area of NPs obtained from contoured images. The plot versus temperature is shown in Figure 5.11. The data reveals a consistent trend between the two NPs. From RT to 300 °C, there are no significant changes in the morphology of the NPs. The projected areas of the NPs remain relatively stable, indicating minimal structural evolution. Between 400 and 600 °C, interparticle mass transfer becomes evident. The projected areas of the NPs increased, indicating the interparticle mass transfer. This stage shows the start of atom migration between adjacent NPs, leading to changes in their sizes. At higher temperatures up to 1000

°C, significant coalescence occurs. The number of distinct NPs reduces to one, as seen at 800 °C, where the total projected area of the merged NP is 168 nm^2. The merging of NPs results in the formation of larger particles with increased projected areas. The ML segmentation and contoured HAADF-STEM images clearly show the merging of NPs and the resulting changes in their morphology.

Table 5.3 Measurement of number and projected area of NPs from in situ STEM images.

Temperature/°C	Number of NPs	Projected area of NP 1/nm^2	Projected area of NP 2/nm^2	Total projected area /nm^2
20	2	67	80	147
100	2	64	77	141
200	2	66	82	148
300	2	62	75	137
400	2	71	84	155
500	2	76	88	164
600	2	82	87	169
700	2	77	83	160
800	1	168		
900	1	170		
1000	1	152		

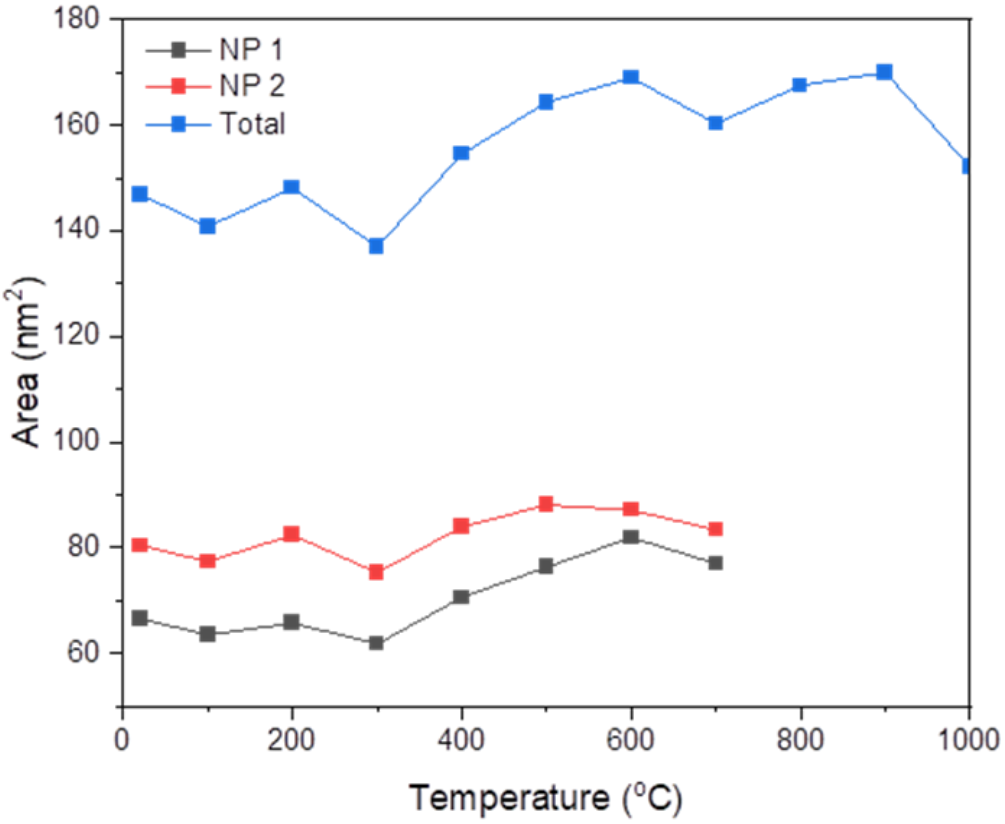


Figure 5.11 Measured projected area of each NP and summation of two NPs.

5.3.6 Proposed Mechanism

Overall, to understand how different metal elements affect two kinds of structures – core-shell and alloy, we did a series of in situ STEM-EDS experiments and found that mass transfer could be the key to inducing the final configuration of NPs. Figure 5.12 shows a schematic illustration of our proposed mechanisms. Because HEA NPs are loaded on carbon support, atoms are immobilized, leading to no mass transfer through this type of material. Therefore, the alloy structure would maintain well until 800 °C and 1000 °C. For core-shell NPs, the mechanism is more complicated due to the possible mass transfer via SiN_x

membrane on the MEMS heating chip. We divided this into three scenarios according to the amount of interacted materials. Firstly, if there is nearly no mass transfer with an individual NP, the core-shell structure would change to a homogeneous alloy structure upon heating to 800 °C and the alloy would be stable even heating to 1000 °C. Secondly, when small atom clusters containing Pd or Cu interacted with the NP at 800 °C, it would transform into Janus structure with noble metals Pd and Pt on one side and TMs Ni and Co on the other side. Lastly, when 2 NPs are adjacent to each other as neighbors, they would merge at 800 °C and the produced NP would also have Janus structure similar to above. In summary, based on our in situ experiments data, we suggest that atoms are not mobilized below 800 °C, causing no mass transfer between the NP and the outside environment within this temperature range. However, when the temperature is above 800 °C, NPs would have different transformations. Entropy-stabilized HEA NPs and isolated core-shell NPs would maintain the solid solution structure. Core-shell NPs with interaction with atom clusters or another NP would transform to Janus structure.

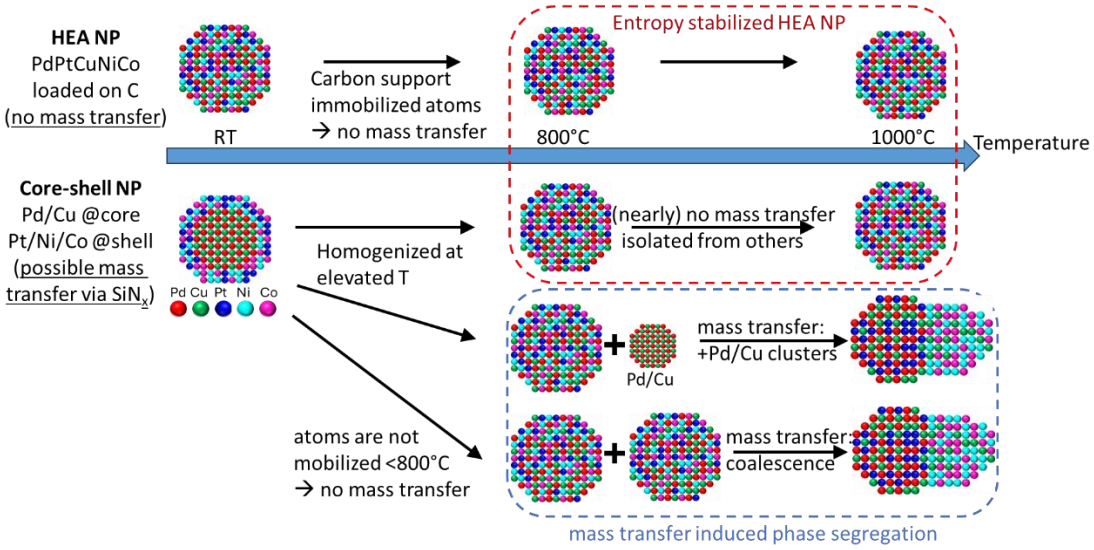


Figure 5.12 Proposed mechanism from in situ TEM heating experiments.

From the perspective of metal diffusion, the HEA NPs supported on carbon did not exhibit atomic mobility up to 800 °C, maintaining their alloy structure even at temperatures as high as 1000 °C. This stability is likely due to the high entropy of mixing, which fosters a uniform elemental distribution and resists phase separation. Conversely, core-shell PdCu@PtNiCo NPs displayed more intricate behavior, influenced by potential mass transfer via the SiN_x membrane on the MEMS heating chip. In scenarios without significant external atomic interaction, the core-shell structure transitioned into a homogeneous alloy at 800 °C, indicating that internal diffusion for elemental homogenization. However, interactions with atom clusters prompted the formation of Janus structures. This transformation is driven by the preferential diffusion of Pd and Cu, attributable to their higher diffusion coefficients.

Considering surface energy, it fundamentally influences NP stability and morphology. In core-shell NPs, the PtNiCo shell possesses higher surface energy compared to the PdCu core, leading to the diffusion of the shell elements to minimize overall surface energy. This tendency becomes more evident when atomic clusters or adjacent NPs interact, resulting in Janus structures where noble TMs Ni and Co. For HEA NPs, the homogeneous distribution of all five elements ensures a relatively uniform surface energy across the NP. This uniformity, coupled with high entropy, sustains a stable alloy structure even at elevated temperatures, suppressing surface energy-driven coalescence and growth.

From the standpoint of phase stability, this phenomenon could be partially understood based on the theory of thermodynamics, specifically the second law, which states that systems evolve towards minimizing their Gibbs free energy [155]. The Gibbs free energy of mixing ΔG_{mix} is given by:

$$\Delta G_{mix} = \Delta H_{mix} - T\Delta S_{mix}$$

In high-entropy systems, the entropy of mixing ΔS_{mix} is substantial due to the large number of different elements. This increased entropy significantly lowers the Gibbs free energy, especially at high temperatures, favoring the formation of solid solution phase rather than intermetallic compounds. The substantial ΔS_{mix} overcomes any medium negative ΔH_{mix}, favoring the homogeneous mixing of elements. Without mass transfer between NPs, HEA NPs remain stable due to the entropy stabilization effect. As T increases, $T\Delta S_{\text{mix}}$ increases, further lowering ΔG_{mix} and maintaining the disordered solid solution structure. In core-shell PdCu@PtNiCo NPs, phase stability is more dynamic due to the potential for phase segregation driven by diffusion and surface energy minimization. The formation of a homogeneous alloy at 800 °C suggests that the core-shell interface becomes thermodynamically unstable. When small atom clusters or neighboring NPs interact, the system's free energy is further minimized by forming Janus structures, where phase separation occurs due to differences in diffusion rates and surface energy between noble and transition metals.

To validate our proposed elemental redistribution mechanism, we have carried out collaborations with theorists to conduct a series of molecular dynamics simulations. We have developed a model with a single core-shell NP and two attached core-shell NPs to simulate the evolution. This ongoing work would provide more insights into the structural transitions of NPs and validate the proposed elemental redistribution mechanism under different conditions.

5.4 Conclusions

In summary, this study presents comprehensive in situ STEM observations and EDS mapping of phase segregation phenomena in core-shell and HEA PdCuPtNiCo NPs during heating. Our findings reveal that phase transformations at elevated temperatures are predominantly governed by mass transfer mechanisms. HEA NPs demonstrated good thermal stability, maintaining homogeneous alloy structure throughout the entire heating process. This stability is attributed to the immobilization of atoms on the carbon support, which inhibits mass transfer and prevents phase separation. The high configurational entropy of HEAs also contributes to the stabilization of a single-phase solid solution.

In contrast, core-shell NPs exhibit more complex thermal behavior due to their potential for mass transfer and interaction with surrounding materials. In the absence of mass transfer, core-shell NPs undergo a transformation to a homogeneous alloy structure at 800 °C, which is then maintained up to 1000 °C. However, when core-shell NPs interact with atomic clusters or neighboring NPs, significant phase transformations occur, leading to the formation of Janus structures. These Janus NPs exhibit a clear segregation of noble metals (Pd and Pt) and transition metals (Ni and Co), driven by differences in diffusion rates, surface energy, and atomic interactions.

The observed inward and outward diffusion of metals provides critical insights into the mechanisms of mass transfer and phase stability in multimetallic NPs. The formation of Janus structures at high temperatures highlights the role of external interactions in driving phase segregation. Our study provides valuable guidelines for the design of high-temperature-resistant materials and stable catalysts.

CHAPTER 6 Conclusions and Perspectives

6.1 Conclusions

We have systematically studied the evolutions of bimetallic, core-shell and HEA NPs under thermal conditions using in situ TEM methodologies and AI-enabled data analytics. After the rapid advancement in the past two decades, in situ TEM has become sophisticated regarding both methodology and instrumentation. We leveraged the in situ TEM heating setup and then used this to study the solid phase reactions in energy materials especially those used as catalysts.

Chapter 1 provides an introduction to multimetallic NPs, highlighting their controlled shapes, structures, and compositions. The chapter also discusses the various applications of these NPs and the motivation behind this research. Chapter 2 outlines the experimental methods used in this study, detailing the synthesis and characterization techniques. Conventional TEM, STEM, and in situ TEM methods are described, emphasizing their roles in elucidating the properties and behaviors of multimetallic NPs.

In situ TEM is a technique requiring effective tools for analyzing large datasets. The rapid advancement of AI technology has enabled diverse ML approaches to address the significant data analysis challenges in this field. Chapter 3 extensively reviews recent advancements in ML and DL methods applied to analyze TEM data. Methods for image segmentation and synthetic data generation are described. We applied the ML image segmentation on in situ images and extracted information about the dynamics of the NPs, such as a function of time and temperatures. The results indicated the thermally induced interactions between NPs during in situ heating at various elevated temperatures. Through

a series of control experiments, we have determined the optimized imaging parameters with high accuracy for data analysis, in terms of the optimized resolution for precision and field-of-view combinations for statistics, which can guide our in situ heating experiments.

The first NP system investigated using in situ TEM is Pt-Ni NPs. The experimental methods for synthesizing Pt-Ni NPs with 2 distinct structures and the characterization techniques are described. The observed morphological evolution includes the facet development from a truncated octahedron to a spherical-like isotropic shape, followed by the formation of pancake-like ellipsoid shape at high temperatures due to surface atom migration and interfacial wetting enabled by the particle-substrate interaction. Comparative investigations by in situ STEM with EDS mapping elucidate that the solid-solution compositional configuration can be retained over a large temperature range, while core-shell NPs undergo irreversible solid-solution transitions through chemical homogenization at elevated temperatures.

The in situ TEM studies extended to another NP system, quinary PdCuPtNiCo NPs with core-shell and HEA structures. The crystal structure and mixing patterns are examined by STEM and EDS mapping. Through a series of in situ experiments, We found that the chemical evolutions during heating are controlled by mass transfer with nearby NPs. If there is no mass transfer between NPs, they would maintain the solid solution structure. However, mass transfer with background atom clusters or neighbor NPs would happen and form Janus structure after heating. These findings elucidate the effect of thermal input on structural evolution and compositional redistribution of metallic NPs, offering valuable insights into the design of heterogeneous catalysts.

6.2 Perspectives

In advancing the understanding of thermally induced evolutions of multimetallic NPs, computational modeling emerges as a pivotal tool. By simulating the atomic and molecular dynamics of these complex systems, we can validate the proposed mechanisms of transformation observed through experiments. These simulations could offer a deep understanding of the diffusion processes, phase segregation, and surface energy effects that govern the NPs behavior under thermal conditions.

Leveraging the knowledge gained from this study, we can establish design principles that are broadly applicable to other multimetallic systems. Understanding the interactions and behaviors in the two model systems provides a robust framework for predicting and enhancing the properties of a wide array of metallic NPs. Expanding the research to encompass a broader range of material systems with diverse metal elements presents an opportunity. By investigating different combinations of metals in NPs, researchers can explore new interesting evolutions, which would affect catalytic, electronic, and magnetic properties. This expansion not only enhances our fundamental understanding of nanomaterials behavior under dynamic conditions but also facilitates the design and optimization of novel materials tailored for specific applications.

Overall, this study highlights the effectiveness of in situ TEM in monitoring dynamic structural and chemical changes in metallic NPs. Integrating ML-enhanced data analytics with in situ TEM methodologies offers promising avenues for innovative discoveries to address critical challenges in energy technologies.

References

[1] G. Sharma, A. Kumar, S. Sharma, M. Naushad, R. Prakash Dwivedi, Z.A. Alothman, G.T. Mola, Novel development of nanoparticles to bimetallic nanoparticles and their composites: A review, Journal of King Saud University - Science, 31 (2019) 257-269.

[2] R. Ferrando, J. Jellinek, R.L. Johnston, Nanoalloys: From Theory to Applications of Alloy Clusters and Nanoparticles, Chemical Reviews, 108 (2008) 845-910.

[3] J. Gu, F. Duan, S. Liu, W. Cha, J. Lu, Phase Engineering of Nanostructural Metallic Materials: Classification, Structures, and Applications, Chemical Reviews, 124 (2024) 1247-1287.

[4] P. Qiao, S. Zou, S. Xu, J. Liu, Y. Li, G. Ma, L. Xiao, H. Lou, J. Fan, A general synthesis strategy of multi-metallic nanoparticles within mesoporous titania via in situ photo-deposition, Journal of Materials Chemistry A, 2 (2014) 17321-17328.

[5] B. Roldan Cuenya, Metal Nanoparticle Catalysts Beginning to Shape-up, Accounts of Chemical Research, 46 (2013) 1682-1691.

[6] K. An, G.A. Somorjai, Size and Shape Control of Metal Nanoparticles for Reaction Selectivity in Catalysis, ChemCatChem, 4 (2012) 1512-1524.

[7] Y. Xia, Y. Xiong, B. Lim, S.E. Skrabalak, Shape-Controlled Synthesis of Metal Nanocrystals: Simple Chemistry Meets Complex Physics?, Angewandte Chemie International Edition, 48 (2009) 60-103.

[8] C. Wang, C. Lin, L. Zhang, Z. Quan, K. Sun, B. Zhao, F. Wang, N. Porter, Y. Wang, J. Fang, Pt_3Co Concave Nanocubes: Synthesis, Formation Understanding, and Enhanced Catalytic

Activity toward Hydrogenation of Styrene, Chemistry – A European Journal, 20 (2014) 1753-1759.

[9] J. Wu, H. Yang, Synthesis and electrocatalytic oxygen reduction properties of truncated octahedral Pt3Ni nanoparticles, Nano Research, 4 (2010) 72-82.

[10] H.-G. Liao, L. Cui, S. Whitelam, H. Zheng, Real-Time Imaging of Pt_3Fe Nanorod Growth in Solution, Science, 336 (2012) 1011.

[11] Y. Xiong, H. Cai, B.J. Wiley, J. Wang, M.J. Kim, Y. Xia, Synthesis and Mechanistic Study of Palladium Nanobars and Nanorods, Journal of the American Chemical Society, 129 (2007) 3665-3675.

[12] S. Choi, S.I. Han, D. Jung, H.J. Hwang, C. Lim, S. Bae, O.K. Park, C.M. Tschabrunn, M. Lee, S.Y. Bae, J.W. Yu, J.H. Ryu, S.-W. Lee, K. Park, P.M. Kang, W.B. Lee, R. Nezafat, T. Hyeon, D.-H. Kim, Highly conductive, stretchable and biocompatible Ag–Au core–sheath nanowire composite for wearable and implantable bioelectronics, Nature Nanotechnology, 13 (2018) 1048-1056.

[13] B. Lim, M. Jiang, P.H.C. Camargo, E.C. Cho, J. Tao, X. Lu, Y. Zhu, Y. Xia, Pd-Pt Bimetallic Nanodendrites with High Activity for Oxygen Reduction, Science, 324 (2009) 1302-1305.

[14] M.M. Maye, W. Zheng, F.L. Leibowitz, N.K. Ly, C.-J. Zhong, Heating-Induced Evolution of Thiolate-Encapsulated Gold Nanoparticles: A Strategy for Size and Shape Manipulations, Langmuir, 16 (2000) 490-497.

[15] M. Sankar, N. Dimitratos, P.J. Miedziak, P.P. Wells, C.J. Kiely, G.J. Hutchings, Designing bimetallic catalysts for a green and sustainable future, Chemical Society Reviews, 41 (2012) 8099-8139.

[16] K.E. MacArthur, M. Heggen, R.E. Dunin-Borkowski, Differentiating the structure of PtNi octahedral nanoparticles through combined ADF–EDX simulations, Advanced Structural and Chemical Imaging, 4 (2018) 2.

[17] Z. Qi, H. Geng, X. Wang, C. Zhao, H. Ji, C. Zhang, J. Xu, Z. Zhang, Novel nanocrystalline PdNi alloy catalyst for methanol and ethanol electro-oxidation in alkaline media, Journal of Power Sources, 196 (2011) 5823-5828.

[18] J. Wu, A. Gross, H. Yang, Shape and Composition-Controlled Platinum Alloy Nanocrystals Using Carbon Monoxide as Reducing Agent, Nano Letters, 11 (2011) 798-802.

[19] N. Kar, M. McCoy, J. Wolfe, S.L.A. Bueno, I.H. Shafei, S.E. Skrabalak, Retrosynthetic design of core–shell nanoparticles for thermal conversion to monodisperse high-entropy alloy nanoparticles, Nature Synthesis, 3 (2024) 175-184.

[20] Y. Chen, Z. Liang, F. Yang, Y. Liu, S. Chen, Ni–Pt Core–Shell Nanoparticles as Oxygen Reduction Electrocatalysts: Effect of Pt Shell Coverage, The Journal of Physical Chemistry C, 115 (2011) 24073-24079.

[21] J.-Y. Bigot, H. Kesserwan, V. Halté, O. Ersen, M.S. Moldovan, T.H. Kim, J.-t. Jang, J. Cheon, Magnetic Properties of Annealed Core–Shell CoPt Nanoparticles, Nano Letters, 12 (2012) 1189-1197.

[22] X. Huang, Z. Liu, M.-M. Millet, J. Dong, M. Plodine, F. Ding, R. Schlögl, M.-G. Willinger, In Situ Atomic-Scale Observation of Surface-Tension-Induced Structural Transformation of Ag-NiPx Core–Shell Nanocrystals, ACS Nano, 12 (2018) 7197-7205.

[23] X.-W. Zhou, R.-H. Zhang, Z.-Y. Zhou, S.-G. Sun, Preparation of PtNi hollow nanospheres for the electrocatalytic oxidation of methanol, Journal of Power Sources, 196 (2011) 5844-5848.

[24] X. Wang, Q. Dong, H. Qiao, Z. Huang, M.T. Saray, G. Zhong, Z. Lin, M. Cui, A. Brozena, M. Hong, Q. Xia, J. Gao, G. Chen, R. Shahbazian-Yassar, D. Wang, L. Hu, Continuous Synthesis of Hollow High-Entropy Nanoparticles for Energy and Catalysis Applications, Advanced Materials, 32 (2020) 2002853.

[25] S. De, J. Zhang, R. Luque, N. Yan, Ni-based bimetallic heterogeneous catalysts for energy and environmental applications, Energy & Environmental Science, 9 (2016) 3314-3347.

[26] S.I. Choi, S. Xie, M. Shao, J.H. Odell, N. Lu, H.C. Peng, L. Protsailo, S. Guerrero, J. Park, X. Xia, J. Wang, M.J. Kim, Y. Xia, Synthesis and characterization of 9 nm Pt-Ni octahedra with a record high activity of 3.3 A/mg(Pt) for the oxygen reduction reaction, Nano Lett, 13 (2013) 3420-3425.

[27] V.R. Stamenkovic, B. Fowler, B.S. Mun, G. Wang, P.N. Ross, C.A. Lucas, N.M. Marković, Improved Oxygen Reduction Activity on Pt_3Ni(111) via Increased Surface Site Availability, Science, 315 (2007) 493.

[28] J. Zhang, H. Yang, J. Fang, S. Zou, Synthesis and Oxygen Reduction Activity of Shape-Controlled Pt_3Ni Nanopolyhedra, Nano Letters, 10 (2010) 638-644.

[29] P.G. Jamkhande, N.W. Ghule, A.H. Bamer, M.G. Kalaskar, Metal nanoparticles synthesis: An overview on methods of preparation, advantages and disadvantages, and applications, Journal of Drug Delivery Science and Technology, 53 (2019) 101174.

[30] J.W. Yeh, S.K. Chen, S.J. Lin, J.Y. Gan, T.S. Chin, T.T. Shun, C.H. Tsau, S.Y. Chang, Nanostructured High-Entropy Alloys with Multiple Principal Elements: Novel Alloy Design Concepts and Outcomes, Advanced Engineering Materials, 6 (2004) 299-303.

[31] B.S. Murty, J.W. Yeh, S. Ranganathan, Chapter 2 - High-Entropy Alloys: Basic Concepts, in: B.S. Murty, J.W. Yeh, S. Ranganathan (Eds.) High Entropy Alloys, Butterworth-Heinemann, Boston, 2014, pp. 13-35.

[32] Y. Sun, S. Dai, High-entropy materials for catalysis: A new frontier, Science Advances, 7 eabg1600.

[33] Y. Yao, Z. Huang, P. Xie, S.D. Lacey, R.J. Jacob, H. Xie, F. Chen, A. Nie, T. Pu, M. Rehwoldt, D. Yu, M.R. Zachariah, C. Wang, R. Shahbazian-Yassar, J. Li, L. Hu, Carbothermal shock synthesis of high-entropy-alloy nanoparticles, Science, 359 (2018) 1489.

[34] P.-C. Chen, X. Liu, L. Hedrick James, Z. Xie, S. Wang, Q.-Y. Lin, C. Hersam Mark, P. Dravid Vinayak, A. Mirkin Chad, Polyelemental nanoparticle libraries, Science, 352 (2016) 1565-1569.

[35] S.L.A. Bueno, A. Leonardi, N. Kar, K. Chatterjee, X. Zhan, C. Chen, Z. Wang, M. Engel, V. Fung, S.E. Skrabalak, Quinary, Senary, and Septenary High Entropy Alloy Nanoparticle Catalysts from Core@Shell Nanoparticles and the Significance of Intraparticle Heterogeneity, ACS Nano, 16 (2022) 18873-18885.

[36] Q. Wu, Z. Wang, F. He, L. Wang, J. Luo, J. Li, J. Wang, High Entropy Alloys: From Bulk Metallic Materials to Nanoparticles, Metallurgical and Materials Transactions A, 49 (2018) 4986-4990.

[37] H. Qiao, M.T. Saray, X. Wang, S. Xu, G. Chen, Z. Huang, C. Chen, G. Zhong, Q. Dong, M. Hong, H. Xie, R. Shahbazian-Yassar, L. Hu, Scalable Synthesis of High Entropy Alloy Nanoparticles by Microwave Heating, ACS Nano, 15 (2021) 14928-14937.

[38] Q. Dong, M. Hong, J. Gao, T. Li, M. Cui, S. Li, H. Qiao, A.H. Brozena, Y. Yao, X. Wang, G. Chen, J. Luo, L. Hu, Rapid Synthesis of High-Entropy Oxide Microparticles, Small, 18 (2022) 2104761.

[39] A.H. Phakatkar, M.T. Saray, M.G. Rasul, L.V. Sorokina, T.G. Ritter, T. Shokuhfar, R. Shahbazian-Yassar, Ultrafast Synthesis of High Entropy Oxide Nanoparticles by Flame Spray Pyrolysis, Langmuir, 37 (2021) 9059-9068.

[40] S. Gao, S. Hao, Z. Huang, Y. Yuan, S. Han, L. Lei, X. Zhang, R. Shahbazian-Yassar, J. Lu, Synthesis of high-entropy alloy nanoparticles on supports by the fast moving bed pyrolysis, Nature Communications, 11 (2020) 2016.

[41] Y. Yang, B. Song, X. Ke, F. Xu, K.N. Bozhilov, L. Hu, R. Shahbazian-Yassar, M.R. Zachariah, Aerosol Synthesis of High Entropy Alloy Nanoparticles, Langmuir, 36 (2020) 1985-1992.

[42] J. Feng, D. Chen, P.V. Pikhitsa, Y.-h. Jung, J. Yang, M. Choi, Unconventional Alloys Confined in Nanoparticles: Building Blocks for New Matter, Matter, 3 (2020) 1646-1663.

[43] F. Okejiri, Z. Zhang, J. Liu, M. Liu, S. Yang, S. Dai, Room-Temperature Synthesis of High-Entropy Perovskite Oxide Nanoparticle Catalysts through Ultrasonication-Based Method, ChemSusChem, 13 (2020) 111-115.

[44] M. Liu, Z. Zhang, F. Okejiri, S. Yang, S. Zhou, S. Dai, Entropy-Maximized Synthesis of Multimetallic Nanoparticle Catalysts via a Ultrasonication-Assisted Wet Chemistry Method under Ambient Conditions, Advanced Materials Interfaces, 6 (2019) 1900015.

[45] F. Waag, Y. Li, A.R. Ziefuß, E. Bertin, M. Kamp, V. Duppel, G. Marzun, L. Kienle, S. Barcikowski, B. Gökce, Kinetically-controlled laser-synthesis of colloidal high-entropy alloy nanoparticles, RSC Advances, 9 (2019) 18547-18558.

[46] D. Wu, K. Kusada, T. Yamamoto, T. Toriyama, S. Matsumura, S. Kawaguchi, Y. Kubota, H. Kitagawa, Platinum-Group-Metal High-Entropy-Alloy Nanoparticles, Journal of the American Chemical Society, 142 (2020) 13833-13838.

[47] K. Mori, N. Hashimoto, N. Kamiuchi, H. Yoshida, H. Kobayashi, H. Yamashita, Hydrogen spillover-driven synthesis of high-entropy alloy nanoparticles as a robust catalyst for CO_2 hydrogenation, Nature Communications, 12 (2021) 3884.

[48] S. VijayaVenkataRaman, S. Iniyan, R. Goic, A review of climate change, mitigation and adaptation, Renewable and Sustainable Energy Reviews, 16 (2012) 878-897.

[49] S.G. Yalew, M.T.H. van Vliet, D.E.H.J. Gernaat, F. Ludwig, A. Miara, C. Park, E. Byers, E. De Cian, F. Piontek, G. Iyer, I. Mouratiadou, J. Glynn, M. Hejazi, O. Dessens, P. Rochedo, R. Pietzcker, R. Schaeffer, S. Fujimori, S. Dasgupta, S. Mima, S.R.S. da Silva, V. Chaturvedi, R.

Vautard, D.P. van Vuuren, Impacts of climate change on energy systems in global and regional scenarios, Nature Energy, 5 (2020) 794-802.

[50] I. Dincer, Renewable energy and sustainable development: a crucial review, Renewable and Sustainable Energy Reviews, 4 (2000) 157-175.

[51] C. Liu, F. Li, L.-P. Ma, H.-M. Cheng, Advanced Materials for Energy Storage, Advanced Materials, 22 (2010) E28-E62.

[52] X. Zhang, X. Cheng, Q. Zhang, Nanostructured energy materials for electrochemical energy conversion and storage: A review, Journal of Energy Chemistry, 25 (2016) 967-984.

[53] N. Sharma, H. Ojha, A. Bharadwaj, D.P. Pathak, R.K. Sharma, Preparation and catalytic applications of nanomaterials: a review, RSC Advances, 5 (2015) 53381-53403.

[54] J.C. Chadwick, R. Duchateau, Z. Freixa, P.W.N.M. van Leeuwen, Homogeneous Catalysts: Activity - Stability - Deactivation, Wiley2011.

[55] R. Schlögl, Heterogeneous Catalysis, Angewandte Chemie International Edition, 54 (2015) 3465-3520.

[56] T. Noor, L. Yaqoob, N. Iqbal, Recent Advances in Electrocatalysis of Oxygen Evolution Reaction using Noble-Metal, Transition-Metal, and Carbon-Based Materials, ChemElectroChem, 8 (2021) 447-483.

[57] X. Auvray, L. Olsson, Stability and activity of Pd-, Pt- and Pd–Pt catalysts supported on alumina for NO oxidation, Applied Catalysis B: Environmental, 168-169 (2015) 342-352.

[58] S. Roy, S. Hariharan, A.K. Tiwari, Pt–Ni Subsurface Alloy Catalysts: An Improved Performance toward CH_4 Dissociation, The Journal of Physical Chemistry C, 122 (2018) 10857-10870.

[59] M. Liu, Z. Zhao, X. Duan, Y. Huang, Nanoscale Structure Design for High-Performance Pt-Based ORR Catalysts, Advanced Materials, 31 (2019) 1802234.

[60] S. Duan, Z. Du, H. Fan, R. Wang, Nanostructure Optimization of Platinum-Based Nanomaterials for Catalytic Applications, Nanomaterials, 2018.

[61] L. Liu, A. Corma, Metal Catalysts for Heterogeneous Catalysis: From Single Atoms to Nanoclusters and Nanoparticles, Chemical Reviews, 118 (2018) 4981-5079.

[62] A. Fick, Ueber Diffusion, Annalen der Physik, 170 (1855) 59-86.

[63] C.Z. Hargather, S.-L. Shang, Z.-K. Liu, A comprehensive first-principles study of solute elements in dilute Ni alloys: Diffusion coefficients and their implications to tailor creep rate, Acta Materialia, 157 (2018) 126-141.

[64] P. Marcus, É. Protopopoff, V. Maurice, 5 - Surface Chemistry and Passivation of Metals and Alloys, in: C. Blanc, I. Aubert (Eds.) Mechanics - Microstructure - Corrosion Coupling, Elsevier2019, pp. 91-120.

[65] H. Zhang, M. Jin, Y. Xiong, B. Lim, Y. Xia, Shape-Controlled Synthesis of Pd Nanocrystals and Their Catalytic Applications, Accounts of Chemical Research, 46 (2013) 1783-1794.

[66] K. Yoshida, A. Bright, N. Tanaka, Direct observation of the initial process of Ostwald ripening using spherical aberration-corrected transmission electron microscopy, Journal of Electron Microscopy, 61 (2012) 99-103.

[67] X. Yao, Y. Wei, Z. Wang, L. Gan, Revealing the Role of Surface Composition on the Particle Mobility and Coalescence of Carbon-Supported Pt Alloy Fuel Cell Catalysts by In Situ Heating (S)TEM, ACS Catalysis, 10 (2020) 7381-7388.

[68] R. Tran, Z. Xu, B. Radhakrishnan, D. Winston, W. Sun, K.A. Persson, S.P. Ong, Surface energies of elemental crystals, Scientific Data, 3 (2016) 160080.

[69] Z. Wen, Y. Wang, W. Zhao, M. Jiang, H. Li, Y. Ren, G. Qin, Effects of Ni addition on the order–disorder transitions of Fe–Pt intermetallic compounds: An experimental study on Fe–Ni–Pt phase diagrams, Journal of Materials Science & Technology, 182 (2024) 54-66.

[70] B.T. Sneed, C.N. Brodsky, C.-H. Kuo, L.K. Lamontagne, Y. Jiang, Y. Wang, F. Tao, W. Huang, C.-K. Tsung, Nanoscale-Phase-Separated Pd–Rh Boxes Synthesized via Metal Migration: An Archetype for Studying Lattice Strain and Composition Effects in Electrocatalysis, Journal of the American Chemical Society, 135 (2013) 14691-14700.

[71] M. Gocyla, S. Kuehl, M. Shviro, H. Heyen, S. Selve, R.E. Dunin-Borkowski, M. Heggen, P. Strasser, Shape Stability of Octahedral PtNi Nanocatalysts for Electrochemical Oxygen Reduction Reaction Studied by in situ Transmission Electron Microscopy, ACS Nano, 12 (2018) 5306-5311.

[72] L. Gan, M. Heggen, C. Cui, P. Strasser, Thermal Facet Healing of Concave Octahedral Pt–Ni Nanoparticles Imaged in Situ at the Atomic Scale: Implications for the Rational Synthesis of Durable High-Performance ORR Electrocatalysts, ACS Catalysis, 6 (2015) 692-695.

[73] G. Li, W. Zhang, N. Luo, Z. Xue, Q. Hu, W. Zeng, J. Xu, Bimetallic Nanocrystals: Structure, Controllable Synthesis and Applications in Catalysis, Energy and Sensing, Nanomaterials (Basel), 11 (2021).

[74] K.D. Gilroy, A. Ruditskiy, H.-C. Peng, D. Qin, Y. Xia, Bimetallic Nanocrystals: Syntheses, Properties, and Applications, Chemical Reviews, 116 (2016) 10414-10472.

[75] S.U. Son, Y. Jang, J. Park, H.B. Na, H.M. Park, H.J. Yun, J. Lee, T. Hyeon, Designed Synthesis of Atom-Economical Pd/Ni Bimetallic Nanoparticle-Based Catalysts for Sonogashira Coupling Reactions, Journal of the American Chemical Society, 126 (2004) 5026-5027.

[76] J.C.H. Spence, The future of atomic resolution electron microscopy for materials science, Materials Science and Engineering: R: Reports, 26 (1999) 1-49.

[77] L.E. Franken, K. Grünewald, E.J. Boekema, M.C.A. Stuart, A Technical Introduction to Transmission Electron Microscopy for Soft-Matter: Imaging, Possibilities, Choices, and Technical Developments, Small, 16 (2020) 1906198.

[78] Y. Ding, F. Fan, Z. Tian, Z.L. Wang, Atomic Structure of Au–Pd Bimetallic Alloyed Nanoparticles, Journal of the American Chemical Society, 132 (2010) 12480-12486.

[79] D.B. Williams, C.B. Carter, Transmission Electron Microscopy: A Textbook for Materials Science, Springer US2013.

[80] Y. Jiang, Z. Chen, Y. Han, P. Deb, H. Gao, S. Xie, P. Purohit, M.W. Tate, J. Park, S.M. Gruner, V. Elser, D.A. Muller, Electron ptychography of 2D materials to deep sub-ångström resolution, Nature, 559 (2018) 343-349.

[81] S. Morishita, R. Ishikawa, Y. Kohno, H. Sawada, N. Shibata, Y. Ikuhara, Attainment of 40.5 pm spatial resolution using 300 kV scanning transmission electron microscope equipped with fifth-order aberration corrector, Microscopy, 67 (2018) 46-50.

[82] O.L. Krivanek, N. Dellby, J.A. Hachtel, J.C. Idrobo, M.T. Hotz, B. Plotkin-Swing, N.J. Bacon, A.L. Bleloch, G.J. Corbin, M.V. Hoffman, C.E. Meyer, T.C. Lovejoy, Progress in ultrahigh energy resolution EELS, Ultramicroscopy, 203 (2019) 60-67.

[83] G. Van Tendeloo, S. Bals, S. Van Aert, J. Verbeeck, D. Van Dyck, Advanced Electron Microscopy for Advanced Materials, Advanced Materials, 24 (2012) 5655-5675.

[84] H. Zheng, Y.S. Meng, Y. Zhu, Frontiers of in situ electron microscopy, MRS Bulletin, 40 (2015) 12-18.

[85] M.L. Taheri, E.A. Stach, I. Arslan, P.A. Crozier, B.C. Kabius, T. LaGrange, A.M. Minor, S. Takeda, M. Tanase, J.B. Wagner, R. Sharma, Current status and future directions for in situ transmission electron microscopy, Ultramicroscopy, 170 (2016) 86-95.

[86] Z. Fan, L. Zhang, D. Baumann, L. Mei, Y. Yao, X. Duan, Y. Shi, J. Huang, Y. Huang, X. Duan, In Situ Transmission Electron Microscopy for Energy Materials and Devices, Adv Mater, 31 (2019) e1900608.

[87] H. Zheng, X. Lu, K. He, In situ transmission electron microscopy and artificial intelligence enabled data analytics for energy materials, Journal of Energy Chemistry, 68 (2022) 454-493.

[88] A. Serve, T. Epicier, M. Aouine, F.J. Cadete Santos Aires, E. Obeid, M. Tsampas, K. Pajot, P. Vernoux, Investigations of soot combustion on yttria-stabilized zirconia by environmental transmission electron microscopy (ETEM), Applied Catalysis A: General, 504 (2015) 74-80.

[89] Z. Zhao, Z. Wang, D. Wang, J.-X. Wang, Y. Pu, J.-F. Chen, CFD modelling of gas flow characteristics for the gas-heating holder in environmental transmission electron microscope, The Canadian Journal of Chemical Engineering, 97 (2019) 777-784.

[90] M. Canavan, D. Daly, A. Rummel, E.K. McCarthy, C. McAuley, V. Nicolosi, Novel in-situ lamella fabrication technique for in-situ TEM, Ultramicroscopy, 190 (2018) 21-29.

[91] P.E. Batson, Motion of Gold Atoms on Carbon in the Aberration-Corrected STEM, Microscopy and Microanalysis, 14 (2008) 89-97.

[92] F. Gaulandris, S.B. Simonsen, J.B. Wagner, K. Mølhave, S. Muto, L.T. Kuhn, Methods for Calibration of Specimen Temperature During In Situ Transmission Electron Microscopy Experiments, Microscopy and Microanalysis, 26 (2020) 3-17.

[93] M.A. Asoro, P.J. Ferreira, D. Kovar, In situ transmission electron microscopy and scanning transmission electron microscopy studies of sintering of Ag and Pt nanoparticles, Acta Materialia, 81 (2014) 173-183.

[94] Y. Liu, Y. Sun, Electron beam induced evolution in Au, Ag, and interfaced heterogeneous Au/Ag nanoparticles, Nanoscale, 7 (2015) 13687-13693.

[95] M.A. Asoro, D. Kovar, P.J. Ferreira, Effect of surface carbon coating on sintering of silver nanoparticles: in situ TEM observations, Chemical Communications, 50 (2014) 4835-4838.

[96] Q. Chang, Y. Xu, Z. Duan, F. Xiao, F. Fu, Y. Hong, J. Kim, S.I. Choi, D. Su, M. Shao, Structural Evolution of Sub-10 nm Octahedral Platinum-Nickel Bimetallic Nanocrystals, Nano Lett, 17 (2017) 3926-3931.

[97] Y.-T. Pan, J. Wu, X. Yin, H. Yang, In situ ETEM study of composition redistribution in Pt-Ni octahedral catalysts for electrochemical reduction of oxygen, AIChE Journal, 62 (2016) 399-407.

[98] Y. Xiong, Y. Yang, H. Joress, E. Padgett, U. Gupta, V. Yarlagadda, D.N. Agyeman-Budu, X. Huang, T.E. Moylan, R. Zeng, A. Kongkanand, F.A. Escobedo, J.D. Brock, F.J. DiSalvo, D.A. Muller, H.D. Abruña, Revealing the atomic ordering of binary intermetallics using in situ heating techniques at multilength scales, Proceedings of the National Academy of Sciences, 116 (2019) 1974.

[99] M. Gatalo, F. Ruiz-Zepeda, N. Hodnik, G. Dražić, M. Bele, M. Gaberšček, Insights into thermal annealing of highly-active PtCu3/C Oxygen Reduction Reaction electrocatalyst: An in-situ heating transmission Electron microscopy study, Nano Energy, 63 (2019) 103892.

[100] L. Fei, S.M. Ng, W. Lu, M. Xu, L. Shu, W.-B. Zhang, Z. Yong, T. Sun, C.H. Lam, C.W. Leung, C.L. Mak, Y. Wang, Atomic-Scale Mechanism on Nucleation and Growth of Mo2C Nanoparticles Revealed by in Situ Transmission Electron Microscopy, Nano Letters, 16 (2016) 7875-7881.

[101] L. Fei, X. Gan, S.M. Ng, H. Wang, M. Xu, W. Lu, Y. Zhou, C.W. Leung, C.-L. Mak, Y. Wang, Observable Two-Step Nucleation Mechanism in Solid-State Formation of Tungsten Carbide, ACS Nano, 13 (2019) 681-688.

[102] M. Haenlein, A. Kaplan, A Brief History of Artificial Intelligence: On the Past, Present, and Future of Artificial Intelligence, California Management Review, 61 (2019) 5-14.

[103] Y. LeCun, Y. Bengio, G. Hinton, Deep learning, Nature, 521 (2015) 436-444.

[104] I. Arel, D.C. Rose, T.P. Karnowski, Deep Machine Learning - A New Frontier in Artificial Intelligence Research [Research Frontier], IEEE Computational Intelligence Magazine, 5 (2010) 13-18.

[105] Z. Ghahramani, Probabilistic machine learning and artificial intelligence, Nature, 521 (2015) 452-459.

[106] S.R. Spurgeon, C. Ophus, L. Jones, A. Petford-Long, S.V. Kalinin, M.J. Olszta, R.E. Dunin-Borkowski, N. Salmon, K. Hattar, W.-C.D. Yang, R. Sharma, Y. Du, A. Chiaramonti, H. Zheng, E.C. Buck, L. Kovarik, R.L. Penn, D. Li, X. Zhang, M. Murayama, M.L. Taheri, Towards data-driven next-generation transmission electron microscopy, Nature Materials, 20 (2021) 274-279.

[107] J.M. Ede, Deep learning in electron microscopy, Machine Learning: Science and Technology, 2 (2021) 011004.

[108] M. Ge, F. Su, Z. Zhao, D. Su, Deep learning analysis on microscopic imaging in materials science, Materials Today Nano, 11 (2020) 100087.

[109] S.V. Kalinin, A.R. Lupini, O. Dyck, S. Jesse, M. Ziatdinov, R.K. Vasudevan, Lab on a beam—Big data and artificial intelligence in scanning transmission electron microscopy, MRS Bulletin, 44 (2019) 565-575.

[110] J.P. Horwath, D.N. Zakharov, R. Mégret, E.A. Stach, Understanding important features of deep learning models for segmentation of high-resolution transmission electron microscopy images, npj Computational Materials, 6 (2020) 108.

[111] N.M. Schneider, J.H. Park, M.M. Norton, F.M. Ross, H.H. Bau, Automated analysis of evolving interfaces during in situ electron microscopy, Advanced Structural and Chemical Imaging, 2 (2016) 2.

[112] G. Roberts, S.Y. Haile, R. Sainju, D.J. Edwards, B. Hutchinson, Y. Zhu, Deep Learning for Semantic Segmentation of Defects in Advanced STEM Images of Steels, Scientific Reports, 9 (2019) 12744.

[113] L. Yao, Z. Ou, B. Luo, C. Xu, Q. Chen, Machine Learning to Reveal Nanoparticle Dynamics from Liquid-Phase TEM Videos, ACS Central Science, 6 (2020) 1421-1430.

[114] M. Shen, G. Li, D. Wu, Y. Yaguchi, J.C. Haley, K.G. Field, D. Morgan, A deep learning based automatic defect analysis framework for In-situ TEM ion irradiations, Computational Materials Science, 197 (2021) 110560.

[115] X. Li, O. Dyck, R.R. Unocic, A.V. Ievlev, S. Jesse, S.V. Kalinin, Statistical learning of governing equations of dynamics from in-situ electron microscopy imaging data, Materials & Design, 195 (2020) 108973.

[116] X. Wang, J. Li, H.D. Ha, J.C. Dahl, J.C. Ondry, I. Moreno-Hernandez, T. Head-Gordon, A.P. Alivisatos, AutoDetect-mNP: An Unsupervised Machine Learning Algorithm for Automated Analysis of Transmission Electron Microscope Images of Metal Nanoparticles, JACS Au, 1 (2021) 316-327.

[117] W. Li, K.G. Field, D. Morgan, Automated defect analysis in electron microscopic images, npj Computational Materials, 4 (2018) 36.

[118] V. Jain, J.F. Murray, F. Roth, S. Turaga, V. Zhigulin, K.L. Briggman, M.N. Helmstaedter, W. Denk, H.S. Seung, Supervised Learning of Image Restoration with Convolutional Networks, 2007 IEEE 11th International Conference on Computer Vision, 2007, pp. 1-8.

[119] R. Memisevic, G. Hinton, Unsupervised Learning of Image Transformations, 2007 IEEE Conference on Computer Vision and Pattern Recognition, 2007, pp. 1-8.

[120] W. Kim, A. Kanezaki, M. Tanaka, Unsupervised Learning of Image Segmentation Based on Differentiable Feature Clustering, IEEE Transactions on Image Processing, 29 (2020) 8055-8068.

[121] Z. Ni, W. Yang, S. Wang, L. Ma, S. Kwong, Towards Unsupervised Deep Image Enhancement With Generative Adversarial Network, IEEE Transactions on Image Processing, 29 (2020) 9140-9151.

[122] B. Pierre, Autoencoders, Unsupervised Learning, and Deep Architectures, PMLR, pp. 37-49.

[123] B. Rühle, J.F. Krumrey, V.-D. Hodoroaba, Workflow towards automated segmentation of agglomerated, non-spherical particles from electron microscopy images using artificial neural networks, Scientific Reports, 11 (2021) 4942.

[124] J.P. Horwath, P.W. Voorhees, E.A. Stach, Quantifying Competitive Degradation Processes in Supported Nanocatalyst Systems, Nano Letters, 21 (2021) 5324-5329.

[125] X.L. Lu, K. He, Machine Learning Enhanced Image Segmentation for High-Fidelity STEM Data Analysis, Microsc Microanal, 29 (2023) 1895-1896.

[126] Y. Yin, D. Talapin, The chemistry of functional nanomaterials, Chemical Society Reviews, 42 (2013) 2484-2487.

[127] X. Liu, D. Astruc, From Galvanic to Anti-Galvanic Synthesis of Bimetallic Nanoparticles and Applications in Catalysis, Sensing, and Materials Science, Advanced Materials, 29 (2017) 1605305.

[128] K. Loza, M. Heggen, M. Epple, Synthesis, Structure, Properties, and Applications of Bimetallic Nanoparticles of Noble Metals, Advanced Functional Materials, 30 (2020) 1909260.

[129] J. Wu, P. Li, Y.-T. Pan, S. Warren, X. Yin, H. Yang, Surface lattice-engineered bimetallic nanoparticles and their catalytic properties, Chemical Society Reviews, 41 (2012) 8066-8074.

[130] L. Li, G. Zhang, B. Wang, T. Yang, S. Yang, Electrochemical formation of PtRu bimetallic nanoparticles for highly efficient and pH-universal hydrogen evolution reaction, Journal of Materials Chemistry A, 8 (2020) 2090-2098.

[131] T. Sreethawong, S. Yoshikawa, Impact of photochemically deposited monometallic Pt and bimetallic Pt–Au nanoparticles on photocatalytic dye-sensitized H_2 production activity of mesoporous-assembled TiO_2–SiO_2 mixed oxide nanocrystal, Chemical Engineering Journal, 197 (2012) 272-282.

[132] B.P. Williams, A.P. Young, I. Andoni, Y. Han, W.-S. Lo, M. Golden, J. Yang, L.-M. Lyu, C.-H. Kuo, J.W. Evans, W. Huang, C.-K. Tsung, Strain-Enhanced Metallic Intermixing in Shape-Controlled Multilayered Core–Shell Nanostructures: Toward Shaped Intermetallics, Angewandte Chemie International Edition, 59 (2020) 10574-10580.

[133] M. Chi, C. Wang, Y. Lei, G. Wang, D. Li, K.L. More, A. Lupini, L.F. Allard, N.M. Markovic, V.R. Stamenkovic, Surface faceting and elemental diffusion behaviour at atomic scale for alloy nanoparticles during in situ annealing, Nature Communications, 6 (2015) 8925.

[134] X. Lu, S. Hwang, K. He, In Situ TEM for Structural and Chemical Evolutions of Bimetallic Pt–Ni Nanoparticles at Elevated Temperatures: Implications for Heterogeneous Catalysis, ACS Applied Nano Materials, 7 (2024) 15735-15742.

[135] H. Chen, G. Wang, T. Gao, Y. Chen, H. Liao, X. Guo, H. Li, R. Liu, M. Dou, S. Nan, Q. He, Effect of Atomic Ordering Transformation of PtNi Nanoparticles on Alkaline Hydrogen Evolution: Unexpected Superior Activity of the Disordered Phase, The Journal of Physical Chemistry C, 124 (2020) 5036-5045.

[136] W.-J. Zeng, C. Wang, Q.-Q. Yan, P. Yin, L. Tong, H.-W. Liang, Phase diagrams guide synthesis of highly ordered intermetallic electrocatalysts: separating alloying and ordering stages, Nature Communications, 13 (2022) 7654.

[137] N.E. Singh-Miller, N. Marzari, Surface energies, work functions, and surface relaxations of low-index metallic surfaces from first principles, Physical Review B, 80 (2009) 235407.

[138] Z.-Y. Zhou, N. Tian, J.-T. Li, I. Broadwell, S.-G. Sun, Nanomaterials of high surface energy with exceptional properties in catalysis and energy storage, Chemical Society Reviews, 40 (2011) 4167-4185.

[139] Y. Xia, D. Nelli, R. Ferrando, J. Yuan, Z.Y. Li, Shape control of size-selected naked platinum nanocrystals, Nature Communications, 12 (2021) 3019.

[140] J. Zimmerman, A. Bisht, Y. Mishin, E. Rabkin, Size and shape effects on the strength of platinum nanoparticles, Journal of Materials Science, 56 (2021) 18300-18312.

[141] D. Hill, H. Attia, A.R. Barron, S. Alexander, Size and morphology dependent surface wetting based on hydrocarbon functionalized nanoparticles, Journal of Colloid and Interface Science, 543 (2019) 328-334.

[142] R. Yu, H. Song, X.-F. Zhang, P. Yang, Thermal Wetting of Platinum Nanocrystals on Silica Surface, The Journal of Physical Chemistry B, 109 (2005) 6940-6943.

[143] P. Lu, M. Chandross, T.J. Boyle, B.G. Clark, P. Vianco, Equilibrium Cu-Ag nanoalloy structure formation revealed by in situ scanning transmission electron microscopy heating experiments, APL Materials, 2 (2014).

[144] M. Fu, X. Ma, K. Zhao, X. Li, D. Su, High-entropy materials for energy-related applications, iScience, 24 (2021) 102177.

[145] C.S. Bonifacio, S. Carenco, C.H. Wu, S.D. House, H. Bluhm, J.C. Yang, Thermal Stability of Core–Shell Nanoparticles: A Combined in Situ Study by XPS and TEM, Chemistry of Materials, 27 (2015) 6960-6968.

[146] Q. Ding, Y. Zhang, X. Chen, X. Fu, D. Chen, S. Chen, L. Gu, F. Wei, H. Bei, Y. Gao, M. Wen, J. Li, Z. Zhang, T. Zhu, R.O. Ritchie, Q. Yu, Tuning element distribution, structure and properties by composition in high-entropy alloys, Nature, 574 (2019) 223-227.

[147] J. Cui, H. Zheng, K. He, In Situ TEM Study on Conversion-Type Electrodes for Rechargeable Ion Batteries, Advanced Materials, 33 (2021) 2000699.

[148] B. Song, Y. Yang, M. Rabbani, T.T. Yang, K. He, X. Hu, Y. Yuan, P. Ghildiyal, V.P. Dravid, M.R. Zachariah, W.A. Saidi, Y. Liu, R. Shahbazian-Yassar, In Situ Oxidation Studies of High-Entropy Alloy Nanoparticles, ACS Nano, 14 (2020) 15131-15143.

[149] B. Song, Y. Yang, T.T. Yang, K. He, X. Hu, Y. Yuan, V.P. Dravid, M.R. Zachariah, W.A. Saidi, Y. Liu, R. Shahbazian-Yassar, Revealing High-Temperature Reduction Dynamics of High-Entropy Alloy Nanoparticles via In Situ Transmission Electron Microscopy, Nano Letters, 21 (2021) 1742-1748.

[150] Y. Yao, Z. Liu, P. Xie, Z. Huang, T. Li, D. Morris, Z. Finfrock, J. Zhou, M. Jiao, J. Gao, Y. Mao, J. Miao, P. Zhang, R. Shahbazian-Yassar, C. Wang, G. Wang, L. Hu, Computationally aided, entropy-driven synthesis of highly efficient and durable multi-elemental alloy catalysts, Science Advances, 6 (2020) eaaz0510.

[151] N. Hashimoto, K. Mori, H. Yoshida, N. Kamiuchi, R. Kitaura, R. Hirasawa, H. Yamashita, Thermal Stability of High-Entropy Alloy Nanoparticles Evaluated by In Situ TEM Observations, Nano Letters, (2024).

[152] C. Wang, X. Sang, J.T.L. Gamler, D.P. Chen, R.R. Unocic, S.E. Skrabalak, Facet-Dependent Deposition of Highly Strained Alloyed Shells on Intermetallic Nanoparticles for Enhanced Electrocatalysis, Nano Letters, 17 (2017) 5526-5532.

[153] Y. Yaakob, W.M. Lin, M.S. Rosmi, M.Z.M. Yusop, S. Sharma, K.F. Chan, T. Asaka, M. Tanemura, Study of structural and electrical behavior of silicon-carbon nanocomposites via in situ transmission electron microscopy, Materials Today Communications, 32 (2022) 104081.

[154] R.I. Babicheva, I. Evazzade, E.A. Korznikova, I.A. Shepelev, K. Zhou, S.V. Dmitriev, Low-energy channel for mass transfer in Pt crystal initiated by molecule impact, Computational Materials Science, 163 (2019) 248-255.

[155] W.-L. Hsu, C.-W. Tsai, A.-C. Yeh, J.-W. Yeh, Clarifying the four core effects of high-entropy materials, Nature Reviews Chemistry, 8 (2024) 471-485.